

A Search for Fully Hadronic Decay Modes of the B_c
Meson at CDF

by

Douglas Corey Reher

A.B. (University of California, Berkeley) 1993

A dissertation submitted in partial satisfaction of the
requirements for the degree of

Doctor of Philosophy

in

Physics

in the

GRADUATE DIVISION

of the

UNIVERSITY OF CALIFORNIA, BERKELEY

Committee in charge:

Professor Marjorie D. Shapiro, Chair

Professor Kam-Biu Luk

Professor Stephen Derenzo

Fall 2000

UMI Number: 3002628



UMI Microform 3002628
Copyright 2000 by Bell & Howell Information and Learning Company.
All rights reserved. This microform edition is protected against
unauthorized copying under Title 17, United States Code.

Bell & Howell Information and Learning Company
300 North Zeeb Road
P.O. Box 1346
Ann Arbor, MI 48106-1346

The dissertation of Douglas Corey Reher is approved:

Chair

Date

Date

Date

University of California, Berkeley

Fall 2000

A Search for Fully Hadronic Decay Modes of the B_c Meson at CDF

Copyright © 2000

by

Douglas Corey Reher

This work was supported by the Director, Office of Energy Research,
Office of High Energy and Nuclear Physics, Division of High Energy Physics,
of the U. S. Department of Energy under contract DE-AC03-76SF00098.

The United States Department of Energy has the right to use this
dissertation for any purpose whatsoever including the right to reproduce all
or any part thereof.

Abstract

A Search for Fully Hadronic Decay Modes of the B_c Meson at CDF

by

Douglas Corey Reher

Doctor of Philosophy in Physics

University of California, Berkeley

Professor Marjorie D. Shapiro, Chair

I present a search for the fully hadronic decays of the bottom-charm meson B_c in the mass range 5.6 to 6.8 GeV. The decays $B_c^+ \rightarrow J/\psi\pi^+$ and $B_c^+ \rightarrow J/\psi\pi^+\pi^-\pi^+$ are reconstructed using a data sample corresponding to an integrated luminosity of 109 pb⁻¹ of $p\bar{p}$ collisions at $\sqrt{s} = 1.8$ TeV collected with the Collider Detector at Fermilab. Upper limits on the cross section times branching ratio for each decay mode relative to $B^+ \rightarrow J/\psi K^+$ are presented as a function of the B_c mass.

Chair

Date

Contents

| | | |
|----------|--|-----------|
| 1 | Introduction | 1 |
| 1.1 | The Standard Model: Fundamental Forces and Particles . . . | 2 |
| 1.1.1 | Gauge Bosons | 2 |
| 1.1.2 | Quarks | 3 |
| 1.1.3 | Leptons | 5 |
| 1.2 | B_c in the Standard Model | 7 |
| 1.2.1 | Overview | 7 |
| 1.2.2 | Production of B_c at the Tevatron | 9 |
| 1.2.3 | Mass of the B_c Meson | 13 |
| 1.2.4 | Lifetime of the B_c Meson | 17 |
| 1.2.5 | Branching Ratios of the B_c | 19 |
| 1.3 | Previous CDF limit on $B_c^+ \rightarrow J/\psi \pi^+$ | 22 |
| 2 | Experimental Apparatus | 25 |
| 2.1 | Introduction | 25 |
| 2.2 | Tevatron | 25 |
| 2.2.1 | Introduction | 25 |
| 2.2.2 | Operation of the Tevatron | 28 |
| 2.3 | CDF Detector | 28 |
| 2.3.1 | CDF Coordinate System | 30 |
| 2.3.2 | Superconducting Solenoid | 31 |
| 2.3.3 | Silicon Vertex Detector (SVX') | 31 |
| 2.3.4 | Vertex Tracking Chamber (VTX) | 34 |
| 2.3.5 | Central Tracking Chamber (CTC) | 34 |
| 2.3.6 | Central Calorimeters | 35 |

| | | |
|----------|--|-----------|
| 2.3.7 | Central Muon Chambers | 37 |
| 2.3.8 | Beam-Beam Counter (BBC) | 38 |
| 3 | Data Handling and Monte Carlo Simulation | 41 |
| 3.1 | Introduction | 41 |
| 3.2 | Trigger Requirements | 41 |
| 3.2.1 | Level-1 Trigger | 42 |
| 3.2.2 | Level-2 Trigger | 42 |
| 3.2.3 | Level-3 Trigger | 45 |
| 3.2.4 | Offline Reconstruction | 45 |
| 3.2.5 | Inclusive J/ψ Data Set | 47 |
| 3.3 | Simulation of Events by Monte Carlo | 47 |
| 3.3.1 | Generation of b -quarks. | 47 |
| 3.3.2 | Fragmentation into B_c | 50 |
| 3.3.3 | Simulation of Decay | 54 |
| 3.3.4 | Detector Simulation | 54 |
| 4 | Analysis of the Data | 57 |
| 4.1 | Introduction | 57 |
| 4.2 | Reconstruction of Vertices | 57 |
| 4.3 | Track Quality Cut | 63 |
| 4.4 | J/ψ Selection | 65 |
| 4.5 | Selection of B^+ and B_c mesons | 67 |
| 4.5.1 | Optimization of Final Event Selection | 69 |
| 4.5.2 | Choice of Cut Variables | 70 |
| 4.5.3 | Choice of Statistical Measures | 77 |
| 4.5.4 | Optimized Selection of $B^+ \rightarrow J/\psi K^+$ Events | 78 |

| | | |
|----------|--|------------|
| 4.5.5 | Background Estimation For B_c Decay Modes | 89 |
| 4.5.6 | Estimation of $B_c^+ \rightarrow J/\psi \pi^+$ Signal | 90 |
| 4.6 | Optimized Selection of $B_c^+ \rightarrow J/\psi \pi^+$ Events | 91 |
| 4.7 | Selection of $B_c^+ \rightarrow J/\psi \pi^+ \pi^- \pi^+$ Events | 96 |
| 5 | Efficiency Corrections and Systematic Uncertainties | 106 |
| 5.1 | Introduction | 106 |
| 5.2 | Uncertainty of B_c Mass | 106 |
| 5.3 | Uncertainty of B_c Lifetime | 109 |
| 5.4 | Uncertainty of Fragmentation | 110 |
| 5.5 | Decay-in-Flight Correction | 111 |
| 5.6 | Tracking Efficiency Correction | 114 |
| 6 | Results and Conclusions | 116 |
| 6.1 | Introduction | 116 |
| 6.2 | $B_c^+ \rightarrow J/\psi \pi^+$ Upper Limits | 116 |
| 6.3 | $B_c^+ \rightarrow J/\psi \pi^+ \pi^- \pi^+$ Upper Limits | 120 |
| 6.4 | Conclusions | 122 |
| A | Incorporation of Errors Into Branching Ratio Limit | 124 |
| A.1 | Introduction | 124 |
| A.2 | Peak Area Probability Distribution | 126 |
| A.3 | Poisson Signals With Background Contribution | 128 |
| A.4 | Generalization of Upper Limit | 130 |
| A.5 | Inclusion of Systematic Errors in Final Limit Calculation . . . | 130 |
| A.6 | Numerical Methods and Evaluation of Accuracy | 132 |

List of Figures

| | | |
|----|---|----|
| 1 | Schematic Illustration of $p\bar{p}$ Collision | 10 |
| 2 | Feynman Diagrams Contributing to B_c Production at the Teva- tron | 12 |
| 3 | Calculation of B_c Production Cross Section | 14 |
| 4 | B_c Mass Spectrum | 16 |
| 5 | B_c Decay Diagrams | 17 |
| 6 | Previous CDF Limit on $B_c^+ \rightarrow J/\psi\pi^+$ | 24 |
| 7 | Accelerator Schematic | 26 |
| 8 | CDF Quadrant Cross Section | 29 |
| 9 | SVX' Barrel Schematic | 32 |
| 10 | CTC Endplate Diagram | 36 |
| 11 | Muon Chamber coverage in (η, ϕ) Plane | 39 |
| 12 | Cross-Sectional View of CMU Drift Chamber | 40 |
| 13 | Efficiency of Level-1 Muon Trigger | 43 |
| 14 | Efficiency of Level-2 Muon Trigger | 44 |
| 15 | Dimuon Events Passing Level-3 Trigger | 46 |
| 16 | Fragmentation Functions for B^+ and B_c | 53 |
| 17 | 3-Dimensional χ^2 Distributions for $B^+ \rightarrow J/\psi K^+$ Candidate Events in Data | 60 |
| 18 | 2-Dimensional χ^2 Distributions for $B^+ \rightarrow J/\psi K^+$ Candidate Events in Data | 61 |
| 19 | Sideband-Subtracted 2-Dimensional χ^2 Distributions for $B^+ \rightarrow$ $J/\psi K^+$ Events Compared to Monte Carlo | 62 |
| 20 | 3-Dimensional χ^2 Distributions for $B^+ \rightarrow J/\psi K^+$ Events From Monte Carlo | 64 |

| | | |
|----|--|----|
| 21 | L_{xy} Distributions of J/ψ for Three Levels of Track Quality Cuts | 66 |
| 22 | Invariant Mass Distribution of J/ψ Events | 68 |
| 23 | $c\tau$ Distribution for $B_c^+ \rightarrow J/\psi\pi^+$ Candidate Events Compared to Monte Carlo with Variation in Lifetime and Fragmentation Functions | 71 |
| 24 | P_T^π Distribution for $B_c^+ \rightarrow J/\psi\pi^+$ Candidate Events Compared to Monte Carlo with Variation in Lifetime and Fragmentation Functions | 73 |
| 25 | P_T^B Distribution for $B_c^+ \rightarrow J/\psi\pi^+$ Candidate Events Compared to Monte Carlo with Variation in Lifetime and Fragmentation Functions | 74 |
| 26 | Illustration of Impact Parameter of Tracks from B Decay and from Primary Vertex | 75 |
| 27 | Pion Impact Parameter Distribution for $B_c^+ \rightarrow J/\psi\pi^+$ Candidate Events Compared to Monte Carlo with Variation in Lifetime and Fragmentation Functions | 76 |
| 28 | $\sqrt{\frac{S^2}{S+B}}$ for $B^+ \rightarrow J/\psi K^+$ Events as a Function of P_T^B and $c\tau$ Cuts | 80 |
| 29 | $\sqrt{\frac{S^2}{S+B}}$ for $B^+ \rightarrow J/\psi K^+$ Events as a Function of P_T^K and $c\tau$ Cuts | 81 |
| 30 | $\sqrt{\frac{S^2}{S+B}}$ for $B^+ \rightarrow J/\psi K^+$ Events as a Function of P_T^B and P_T^K Cuts | 82 |
| 31 | Invariant Mass of $B^+ \rightarrow J/\psi K^+$ Events Selected With Optimized Cuts | 83 |
| 32 | Comparison of Monte Carlo With Sideband-Subtracted $c\tau$ Distribution for $B^+ \rightarrow J/\psi K^+$ Events Selected Using Optimized Cuts | 85 |

| | | |
|----|--|-----|
| 33 | Comparison of Monte Carlo With Sideband-Subtracted P_T^B Distribution for $B^+ \rightarrow J/\psi K^+$ Events Selected Using Optimized Cuts | 86 |
| 34 | Comparison of Monte Carlo With Sideband-Subtracted P_T^K Distribution for $B^+ \rightarrow J/\psi K^+$ Events Selected Using Optimized Cuts | 87 |
| 35 | Comparison of Monte Carlo With Sideband-Subtracted d_0 Significance Distribution for $B^+ \rightarrow J/\psi K^+$ Events Selected Using Optimized Cuts | 88 |
| 36 | Optimization of Statistical Significance x_S for $B_c^+ \rightarrow J/\psi \pi^+$. | 93 |
| 37 | Further Optimization of Statistical Significance x_S for $B_c^+ \rightarrow J/\psi \pi^+$ | 94 |
| 38 | Mass Distribution of $B_c^+ \rightarrow J/\psi \pi^+$ Candidate Events With Optimized Cuts | 95 |
| 39 | P_T^π and P_T^B Distributions for $B_c^+ \rightarrow J/\psi \pi^+$ Events Passing Optimized Cuts | 97 |
| 40 | $c\tau$ and πd_0 significance Distributions for $B_c^+ \rightarrow J/\psi \pi^+$ Events Passing Optimized Cuts | 98 |
| 41 | Invariant Mass Distribution of $B_c^+ \rightarrow J/\psi \pi^+ \pi^- \pi^+$ Events . . . | 100 |
| 42 | P_T^B and $c\tau$ Distributions for $B_c^+ \rightarrow J/\psi \pi^+ \pi^- \pi^+$ Events | 102 |
| 43 | P_T^π and πd_0 significance Distributions for $B_c^+ \rightarrow J/\psi \pi^+ \pi^- \pi^+$ Events | 103 |
| 44 | P_T Asymmetry in Signed Impact Parameter | 105 |
| 45 | Weighted P_T Histograms for π and K Decays-in-Flight | 113 |
| 46 | Invariant Mass Distribution of $J/\psi \pi^+$ Events with Optimized Selection Cuts | 117 |
| 47 | Upper Limit Calculation for Representative Bin | 118 |

| | | |
|----|---|-----|
| 48 | Invariant Mass Distribution of $J/\psi\pi^+\pi^-\pi^+$ Events | 120 |
| 49 | Convergence of Generalized Confidence Level Limit Including Errors | 136 |

List of Tables

| | | |
|----|---|-----|
| 1 | Fundamental Forces and Properties of Mediating Gauge Bosons | 3 |
| 2 | Three Generations of Quarks | 5 |
| 3 | Three Generations of Leptons | 7 |
| 4 | Exclusive Branching Ratios of B_c in a Potential Model | 21 |
| 5 | Results of Previous CDF B_c Hadronic Decay Search | 23 |
| 6 | Dimuon Triggers | 48 |
| 7 | Number of $B^+ \rightarrow J/\psi K^+$ Events and Monte Carlo Efficiency for Optimized Cuts | 84 |
| 8 | Number of $B_c^+ \rightarrow J/\psi\pi^+$ Events and Monte Carlo Efficiency for Optimized Cuts | 93 |
| 9 | Number of $B_c^+ \rightarrow J/\psi\pi^+\pi^-\pi^+$ Events and Monte Carlo Efficiency | 101 |
| 10 | $B_c^+ \rightarrow J/\psi\pi^+$ Monte Carlo Efficiency as a Function of Invariant Mass | 107 |
| 11 | $B_c^+ \rightarrow J/\psi\pi^+\pi^-\pi^+$ Monte Carlo Efficiency as a Function of Invariant Mass | 108 |
| 12 | Systematic Uncertainty on $B_c^+ \rightarrow J/\psi\pi^+$ Monte Carlo Effi- ciency Due to B_c Lifetime | 109 |
| 13 | Systematic Uncertainty on $B_c^+ \rightarrow J/\psi\pi^+$ Monte Carlo Effi- ciency Due to B_c Lifetime | 109 |
| 14 | Systematic Uncertainty on $B_c^+ \rightarrow J/\psi\pi^+$ Monte Carlo Effi- ciency Due to Fragmentation Parameterization | 110 |

| | | |
|----|--|-----|
| 15 | Systematic Uncertainty on $B_c^+ \rightarrow J/\psi \pi^+ \pi^- \pi^+$ Monte Carlo Efficiency Due to Fragmentation Parameterization | 111 |
| 16 | $B_c^+ \rightarrow J/\psi \pi^+$ Corrected Efficiency and Calculated 90% CL Upper Limit | 119 |
| 17 | $B_c^+ \rightarrow J/\psi \pi^+ \pi^- \pi^+$ Corrected Efficiency and Calculated 90% CL Upper Limit | 121 |

Chapter 1

Introduction

1 Introduction

The primary aim of high-energy physics is to better understand the way the world works by studying the fundamental units of matter and energy and the means by which they interact with one another. Our present understanding of these phenomena is represented by the so-called “Standard Model” of particle physics. The Standard Model has proven remarkably successful at accommodating experimental results over the last several decades, although it remains incomplete. The missing pieces will eventually come from two experimental fronts: very high energy accelerators to search for Higgs particles and possibly supersymmetric multiplets of the garden-variety particles already observed at existing colliders, as well as directly measuring the predicted tri-boson electroweak vertex; and also at lower energies by studying CP violation and measuring the fundamental parameters of the electroweak theory.

In order to realize such an ambitious physics program, it is first necessary to obtain a reliable understanding of quark interactions at lower energies, including effects caused by QCD dynamics. These effects are typically characterized by a parameter Λ_{QCD}/m_Q , where Λ_{QCD} is the quark confinement scale and m_Q is the quark mass. If this parameter is small (as it is for the heavy c -, b -, and t -quarks), then one can use a perturbative formulation of the quantum mechanical theory to calculate observable effects. By studying production and decay processes of particles containing heavy quarks, one can extract the parameters necessary for evaluating nonperturbative QCD effects in quark hadronization.

1.1 The Standard Model: Fundamental Forces and Particles

1.1.1 Gauge Bosons

Experimental evidence indicates that matter is composed of two types of fundamental¹ particles called quarks and leptons. Both types are fermionic, having spin 1/2, but differ in how they interact via the four known types of bosonic force carriers. The fundamental forces and the relevant properties of their mediating gauge bosons are summarized in Table 1. In the Standard Model, the photon is the carrier of the electromagnetic force, the weak force is mediated by the W and Z bosons, and the carrier of the strong force is the gluon.² The theoretical framework for describing the electromagnetic and weak interactions was laid down by Glashow, Weinberg, and Salam [1, 2, 3] in the 1960s, and the combined theory is known as the electroweak model. The theory of the strong interactions, known as quantum chromodynamics (or QCD), arose out of the contributions of Gell-Mann and others around 1973. [4, 5, 6] The gravitational force between fundamental particles is many orders of magnitude weaker than the other forces at energy scales below the Planck scale (10^{19} GeV), so is negligible for nearly all purposes. It is expected that all of the forces can be described by one single field theory (Grand Unified Theory, or GUT) as one approaches the Planck mass, though such speculation lies somewhat outside the scope of the present analysis.

¹*i.e.*, structureless and pointlike.

²There are actually 8 gluons, differentiated by the symmetry properties of their internal quantum numbers. Just as there are two types of electric charge (+ and −), there are three types of strong “color” (commonly denoted red, green, and blue). In group-theoretical language, the gluons belong to an octet representation of the SU(3) of color ($3 \otimes 3 = 8 \oplus 1$).

| <i>Force</i> | <i>Boson</i> | <i>Symbol</i> | <i>Charge</i> | <i>Spin</i> | <i>Mass</i> | <i>Coupling Strength</i> |
|--------------|--------------|---------------|---------------|-------------|--------------------------|--------------------------|
| E. M. | photon | γ | 0 | 1 | $< 2 \times 10^{-16}$ eV | 1/137 |
| Weak | W | W^{\pm} | ± 1 | 1 | 80.4 | 1.02×10^{-5} |
| | Z | Z^0 | 0 | 1 | 91.2 | |
| Strong | gluon | g | 0 | 1 | 0 | < 1 , small r |
| Gravity | graviton | G | 0 | 2 | 0 | 0.53×10^{-38} |

Table 1: Fundamental forces and properties of mediating gauge bosons. Electric charge is given in units of the proton charge $|e|$ and mass in units of GeV. [7, p. 21]

1.1.2 Quarks

Quarks are distinguished by the fact that they carry fractional electric charges. There are three known “generations” of quarks, with each generation containing one quark with charge $+2/3$ and one with charge $-1/3$; each successive generation corresponds to an increase in quark mass. Physically observable particles are constructed of either three quarks (known as a “baryon”) or a quark-antiquark pair (known as a “meson”). Note that these combinations ensure an integral charge for the observable states, although they are only two out of an arbitrarily large number of combinations that do so. One of the great successes of QCD is that it accounts for the fact that these two, and only these two, combinations occur naturally. Extensions to the theory have been proposed allowing for other physical states, such as six quarks, but there has so far been no compelling physical evidence to support these non-Standard Model theories. According to QCD, only “colorless” states are observable, *i.e.*, only those states corresponding to $SU(3)$ color singlets. Thus, a particle consisting of a quark of a given color and an anti-quark with the same (anti-)color

can be observed, corresponding to the meson. The baryons consist of three quarks, one of each color, which (if one takes the color metaphor literally) is then “white,” or colorless. Physically, the lack of visible lone quarks can be explained by the properties of the strong field. As the distance between two colored quarks increases, the field strength also increases (unlike the more familiar electromagnetic and gravitational forces, which decrease with separation), until there is enough energy accumulated in the gluon field to create new quarks from the vacuum. In this way, one may never observe a quark in isolation. Evidence for the existence of color comes from a number of indirect sources. Measuring the cross section for production of hadrons at an e^+e^- collider, relative to production of lepton pairs (which do not carry color), must give a result proportional to the number of types of hadrons produced, including the color degree of freedom. Experiments of this type give results consistent with $N_c = 3.0$.

The charged weak boson couples most strongly those quarks within a generation, but there does exist mixing between generations. In quantum mechanical terms, the quark flavor eigenstates, while eigenstates of the strong interaction, are not eigenstates of the weak interaction. This mixing can be conveniently expressed in terms of a 3×3 unitary matrix determined by three mixing angles and one nontrivial phase. The magnitudes of the elements of this matrix, called the CKM [8] matrix, are given (at 90% C. L.) by [9]:

$$|\mathcal{M}| = \begin{pmatrix} 0.9745 \text{ to } 0.9760 & 0.217 \text{ to } 0.224 & 0.0018 \text{ to } 0.0045 \\ 0.217 \text{ to } 0.224 & 0.9737 \text{ to } 0.9753 & 0.036 \text{ to } 0.042 \\ 0.004 \text{ to } 0.013 & 0.035 \text{ to } 0.042 & 0.9991 \text{ to } 0.9994 \end{pmatrix},$$

where the charged weak current is then expressed in matrix form via

$$J_{weak}^+ = (\bar{u} \ \bar{c} \ \bar{t}) \mathcal{M} \begin{pmatrix} d \\ s \\ b \end{pmatrix}.$$

It is often convenient to define a new rotated basis for the d -type quarks as:

$$\begin{pmatrix} d' \\ s' \\ b' \end{pmatrix} = \mathcal{M} \begin{pmatrix} d \\ s \\ b \end{pmatrix},$$

so that the weak interaction Lagrangian can be expressed in diagonal form.

Table 2 outlines the notation and physical properties of the quarks.

| <i>Quark</i> | <i>Symbol</i> | <i>Charge</i> | <i>Mass</i> |
|--------------|---------------|---------------|----------------|
| up | u | +2/3 | 1.5 to 5 MeV |
| down | d | −1/3 | 3 to 9 MeV |
| charm | c | +2/3 | 1.1 to 1.4 GeV |
| strange | s | −1/3 | 60 to 170 MeV |
| top | t | +2/3 | 174 GeV |
| bottom | b | −1/3 | 4.1 to 4.4 GeV |

Table 2: Three generations of quarks. Electric charge is given in units of the proton charge $|e|$ Light quark masses are estimates of “current-quark masses,” c - and b -quark masses estimated from meson masses, and t -quark mass measured from direct observation of its decay products. [7, p. 26]

1.1.3 Leptons

Leptons carry integral charges. Following the same structure as the quarks, there are three generations of leptons with each generation containing one

charged lepton and one light neutral lepton (called a “neutrino”). Each successive generation corresponds to an increase in charged lepton mass.³ Leptons are unique in that they do not interact via the strong force. Also, there is an inherent asymmetry exhibited by the neutrinos in their “handedness,” or the orientation of their spin relative to their momentum. Experimentally, only “left-handed” neutrinos⁴ (and “right-handed” antineutrinos) are observed. [10] This represents one of the more striking pieces of evidence that weak interactions are not invariant under spatial inversion. Parity under inversion, prior to 1956, was thought to be one of the solid conservation principles upon which physics rested, akin to the conservation of momentum and energy. Since the discovery of parity violation, [11] other conservation principles (notably CP, which is shorthand for the compound operations of spatial inversion and charge conjugation) have been proposed and found to be violated. [12] Currently, CPT (which adds time reversal to CP) is thought to be an invariant of all physical interactions. This invariance is implicit in the Lagrangian formulation of the Standard Model interactions. Table 3 outlines the notation and physical properties of the leptons.

³Experimental evidence exists for mass splittings between the neutrino generations, which implies a non-zero mass for at least one neutrino. I have made no attempt to assign mass values in Table 3, only recent limits.

⁴Massive left-handed Dirac type neutrinos can be observed as right-handed via a suitable change of inertial reference frames. Though expected to exist if at least one neutrino generation carries mass, these have not yet been observed.

| <i>Lepton</i> | <i>Symbol</i> | <i>Charge</i> | <i>Mass</i> |
|------------------|---------------|---------------|------------------------|
| electron | e | -1 | 0.511 MeV |
| e-neutrino | ν_e | 0 | < 3 eV |
| muon | μ | -1 | 106 MeV |
| μ -neutrino | ν_μ | 0 | < 0.19 MeV, CL = 90% |
| tau | τ | -1 | 1780 MeV |
| τ -neutrino | ν_τ | 0 | < 18.2 MeV, CL = 95% |

Table 3: Three generations of leptons. Electric charge is given in units of the proton charge $|e|$ Electron neutrino mass is inconclusive due to beta decay experiments giving significant imaginary mass results. [7, p. 23-25]

1.2 B_c in the Standard Model

1.2.1 Overview

Of the possible mesons containing at least one heavy quark, $(\bar{b}c)$ is the last remaining family to be studied in detail. The t -quark decays via a real W boson before it can hadronize. Thus, the B_c^+ , which is the bound state of a \bar{b} and a c -quark, is the only physically realizable combination remaining.⁵ It is the only meson consisting of two heavy quarks that carries net flavor, and therefore has unique production and decay mechanisms. The study of B_c decays will extend our quantitative understanding of QCD dynamics.

The spectroscopy of heavy quarkonia can be very reliably calculated using non-relativistic potential models in a way exactly analagous to the positronium or muonium systems, using a potential function motivated by QCD. It can also be calculated in the framework of QCD sum rules, the parameters of

⁵Charge-conjugate states of all particles are implied unless otherwise stated explicitly throughout this analysis.

which are fixed by fitting to the spectroscopic data of the well-studied charmonium ($c\bar{c}$) and bottomonium ($b\bar{b}$) systems. The B_c spectroscopic family is the only system capable of testing the self-consistency between these potential models and QCD sum rules. These tools are used extensively in other aspects of heavy quark physics (*e.g.*, in calculating matrix elements of mixings of heavy quark weak charged currents and estimating contributions that interfere with CP violating diagrams in heavy hadron decays). Since the B_c occupies an intermediate regime between $c\bar{c}$ and $b\bar{b}$, both in meson mass and inter-quark distances, experimental measurement of the B_c spectrum would allow for a determination of which theoretical tools are applicable at the scales of the heavy quarkonia, rather than relying on purely theoretical motivations for choosing a particular model.

Unlike $c\bar{c}$ and $b\bar{b}$, the B_c cannot annihilate to photons or gluons; it must decay weakly. Therefore, it is relatively long-lived and can be studied using conventional techniques of measuring displaced decay vertices at hadron colliders, as these have already been developed for the study of other B mesons. Although the production of B_c is suppressed relative to other B mesons due to the heavy c -quark mass, there is a significant (roughly a factor of 10) enhancement of detection through final-states containing a J/ψ meson, due to its initial charm content. Final-states containing a J/ψ have a very clean experimental decay signature when the J/ψ decays leptonically. Discovery of the B_c has already been accomplished at CDF⁶ via the leptonic decay channel $B_c \rightarrow \psi l \nu$. [13] Reconstruction of the $J/\psi l$ vertex allows for a determination of the B_c lifetime, but the missing neutrino momentum prohibits a precise mass measurement. Hadronic decays fully reconstructed in the detector allow for a

⁶CDF stands for “Collider Detector at Fermilab,” the experimental apparatus upon which this study is based.

more precise measurement of both the B_c mass and its lifetime. In addition, measurements of branching ratios into specific hadronic channels will provide valuable information about both the QCD dynamics and weak interactions in heavy quarkonia.

1.2.2 Production of B_c at the Tevatron

The simple picture presented in Section 1.1.2 of hadrons consisting solely of two or three quarks is not complete. In forming a bound state, these “valence” quarks interact with one another via the exchange of gluons. Moreover, these gluons can briefly produce virtual $q\bar{q}$ pairs of all light flavors from the vacuum. Experimentally, the quarks in a proton typically only carry about half [14] of the proton’s momentum, with the remainder carried by gluons. In considering the collision of a proton with an anti-proton, one must take into account the possibility of collisions between all constituent particles, including the “sea” quarks and gluons as well as the valence quarks. Figure 1 illustrates the internal structure of colliding protons and anti-protons. To produce heavy particles such as the B_c , it is necessary to collide quarks and gluons with a large center-of-mass energy. Only a fraction of the momentum of the (anti-)protons is carried by each constituent parton. Thus, the distribution of parton center-of-mass energies will be

$$\sqrt{\hat{s}} = \sqrt{x_i x_j s},$$

where s is the proton-antiproton CM energy (1.8 TeV) and x_i is the momentum fraction of parton i .

At high energies, hadronic production of B_c is dominated by gluon fusion subprocesses, with negligible contribution from $q\bar{q}$ processes. [15] The production cross section can be calculated fully to order α_s^4 in the framework of

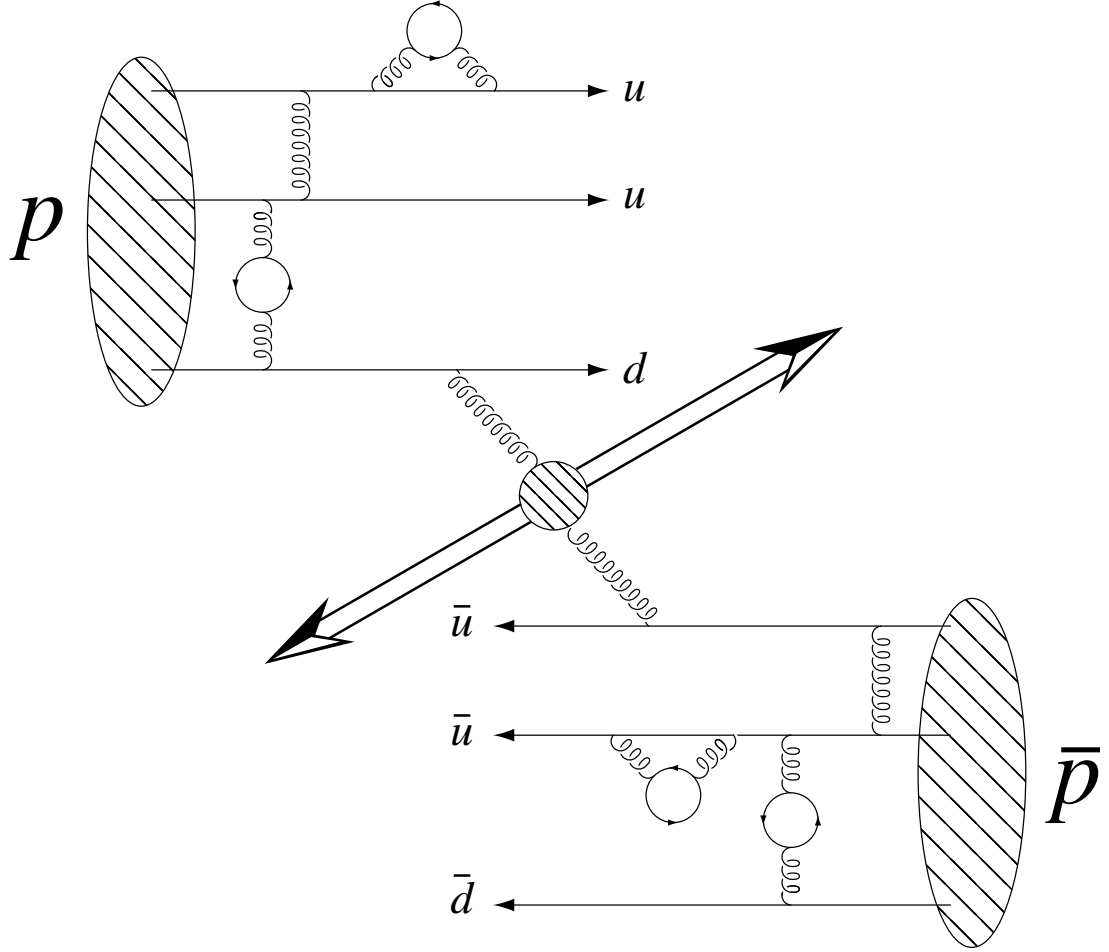


Figure 1: Schematic illustration of $p\bar{p}$ collision. In this diagram, a hard scattering occurs between constituent gluons. The sea quark loops can contain any of the light quark flavors (u , d , or s). The final-state particles from the inelastic scattering subprocess later hadronize into colorless objects. Quark loops and internal gluon lines represent a fraction of the possible contributions to the “sea” parton constituency. Additional higher-order processes also contribute.

perturbative QCD⁷ by summing over 36 gluon-gluon scattering diagrams obtained from the 13 shown in Figure 2 by permuting the initial gluon momenta and the final quark flavors.

The same perturbative calculations show that at high parton center-of-mass energies and large transverse momentum, hadronic B_c production is well-described by b -quark fragmentation. The production process can then be factorized into the short-range (valid under perturbative QCD) regime of $b\bar{b}$ production and long-range (nonperturbative) hadronization of one of the b -quarks into a B_c . The fragmentation description

$$d\hat{\sigma}(B_c) = d\hat{\sigma}(b\bar{b}) \otimes D_{\bar{b} \rightarrow B_c \bar{c}}(z) \quad (1.1)$$

can be used to estimate the production rate of B_c relative to other B mesons. This calculation has been performed using both the HERWIG parton shower Monte Carlo package [16] and using a perturbative calculation in the non-relativistic bound state approximation. [17, 18] Both estimates agree on the magnitude of the cross section ratio and give consistent values of

$$\frac{\sigma(B_c)}{\sigma(b\bar{b})} \simeq 10^{-3}.$$

The cross section for the hadronic process $p\bar{p} \rightarrow B_c + X$ is then obtained by convolving the partonic cross section from these diagrams with the gluon distribution functions describing the distributions of momenta of gluons inside the (anti-)proton:

$$\sigma(s) = \int_0^1 dx_1 \int_0^1 dx_2 g(x_1, Q^2) g(x_2, Q^2) \Theta(x_1 x_2 s - 4M_{B_c}^2) \hat{\sigma}(\hat{s} = x_1 x_2 s), \quad (1.2)$$

where $\hat{\sigma}$ is the partonic cross section evaluated at the parton center-of-mass energy, and $g(x, Q^2)dx$ is the fraction of gluons which carry between x and

⁷ α_s is the dimensionless coupling of gluons to the strong charges carried by quarks, analogous to the electromagnetic coupling constant α ($\sim 1/137$).

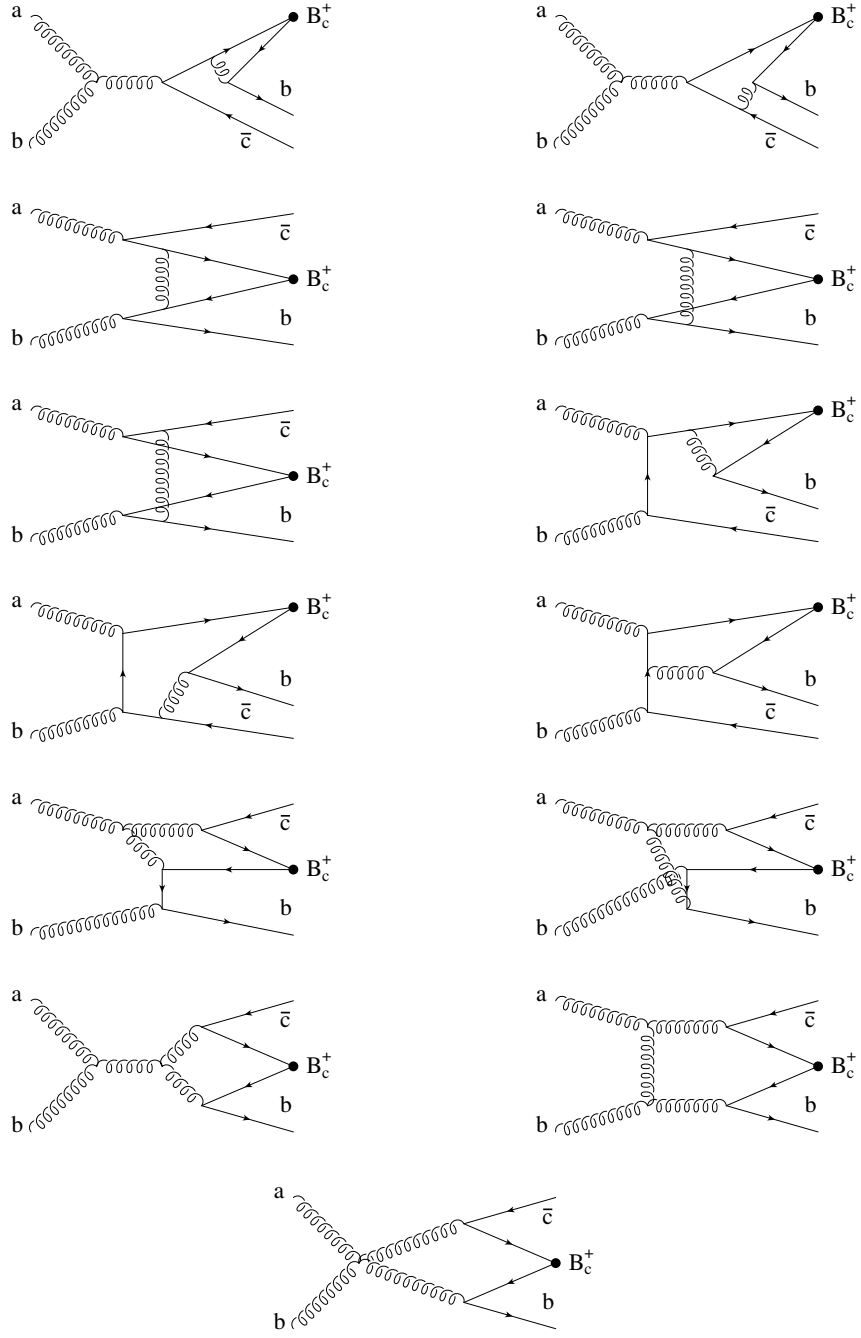


Figure 2: Feynman diagrams contributing to B_c production at the Tevatron. Only 13 gluon fusion diagrams are shown here. The remaining 23 diagrams are obtained by permuting the initial gluon momenta and the final quark flavors.

$x+dx$ of the total (anti-)proton momentum, evaluated at a momentum transfer scale, Q^2 . The Θ -function ensures that there is sufficient center-of-mass energy to produce a real B_c . The gluon distribution functions are primarily measured by deep inelastic scattering of leptons off nucleon targets. [19, 20, 21, 22, 23] The calculation of Equation 1.2 has been performed by several parties [24, 25, 26] to obtain

$$\sigma_{total}(p\bar{p} \rightarrow B_c X) \simeq 20 \text{ to } 50 \text{ nb}$$

at the Tevatron energy of 1.8 TeV.

At center-of-mass energies near threshold or for “small” transverse momentum of the B_c , P_T (small relative to the meson mass), both b fragmentation and $b\bar{c}$ recombination processes (which are not factorizable) can contribute, and the predictions become much less reliable. Figure 3 shows the differential cross section $d\sigma/dP_T$ for B_c production calculated at the Tevatron energy using the MRS(A) [15] gluon distribution for two different evolution scales.

1.2.3 Mass of the B_c Meson

The B_c mass can be estimated very simply by noting that, in solving the Schrödinger equation for a muonium-like system, the expression for the ground-state mass is linear in the reduced mass of the system. Thus, to first order, the mass of the B_c pseudoscalar ground-state is just the average of the $\psi(1S)$ and $\Upsilon(1S)$ masses:

$$M(B_c) \simeq \frac{M(\psi(1S)) + M(\Upsilon(1S))}{2} = \frac{3.097 + 9.460}{2} \text{ GeV} = 6.28 \text{ GeV}. \quad (1.3)$$

A more sophisticated approach would be to use the framework of phenomenological potential models for non-relativistic heavy quarks. By choosing a potential function with a sufficient number of parameters, it is of course always possible to simultaneously fit the data for both the charmonium and

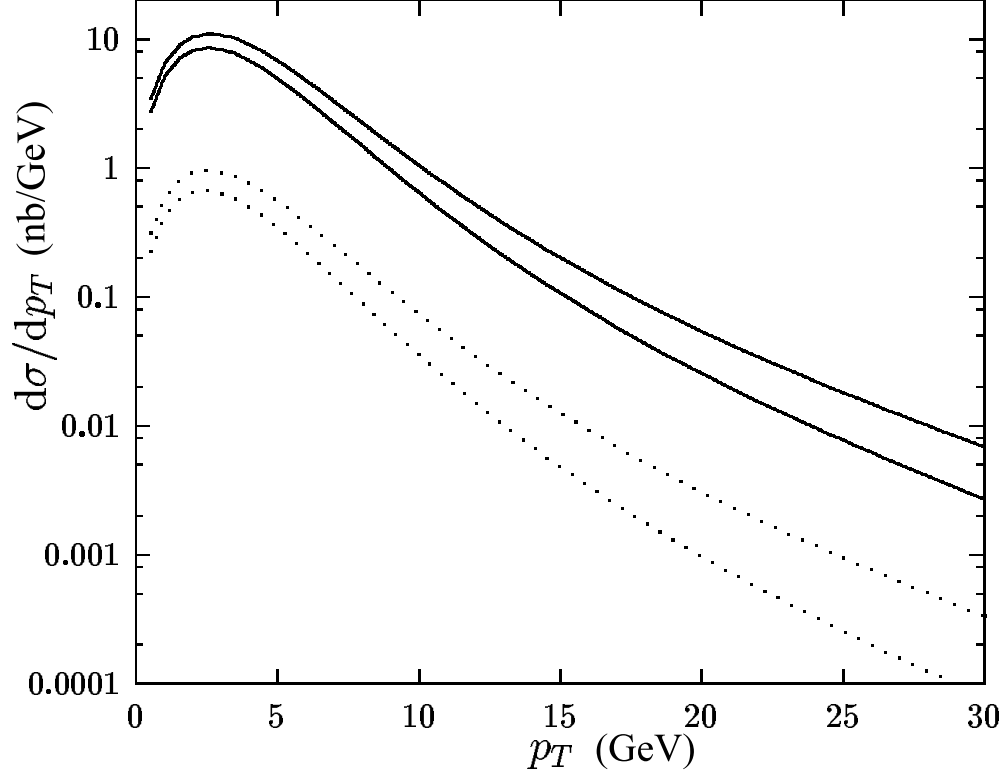


Figure 3: Differential production cross section of B_c , $d\sigma/dp_T$, using MRS(A) gluon distribution functions. Dotted lines indicate cross sections at Tevatron energy $\sqrt{s} = 1.8$ TeV, and solid lines are for LHC energy $\sqrt{s} = 14$ TeV. Upper lines of each type use an evolution scale equivalent to the meson mass $Q^2 = 4M_{B_c}^2$ and lower lines use the parton center-of-mass evolution scale $Q^2 = \hat{s}$. [15]

bottomonium systems. There are a few standard forms favored by QCD theorists, however, and four of these have been used by Eichten *et al.* [27, 28] to calculate the B_c mass. These are a simple power law exponential, a logarithmic potential, a Coulomb plus linear potential, and a QCD-motivated potential proposed by Buchmüller and Tye. [29]

The Schrödinger equation is solved for each potential function to determine the ground-state mass and the level splittings. The strong coupling constant is fixed by fitting to the hyperfine splitting in the charmonium spectrum: $M(J/\psi) - M(\eta_c) = 117$ MeV, where the splitting is determined by:

$$M(3S_1) - M(1S_0) = \frac{32\pi\alpha_s|\Psi(0)|^2}{9m_1m_2},$$

which neglects the variation of α_s with momentum, and scales the splittings of the $\bar{b}c$ and $b\bar{b}$ systems from the $c\bar{c}$ value. The values of the ground-state B_c masses obtained from these potential models are consistent and lie in the range:

$$6.194 \text{ GeV} < M(B_c) < 6.292 \text{ GeV};$$

the mass of the first excited state is similarly determined to be:

$$6.284 \text{ GeV} < M(B_c^*) < 6.357 \text{ GeV}.$$

The measured value [13] of $M(B_c) = 6.4 \pm 0.39 \pm 0.13$ is consistent with these theoretical predictions.⁸

The B_c mass spectrum calculated using a Buchmüller-Tye QCD potential is shown in Figure 4.

⁸I do not include the OPAL [30] measurement of $M(B_c) = 6.32 \pm 0.06$, which is based on 2 candidate $B_c^+ \rightarrow J/\psi\pi^+$ events with an expected background of 0.63 ± 0.20 .

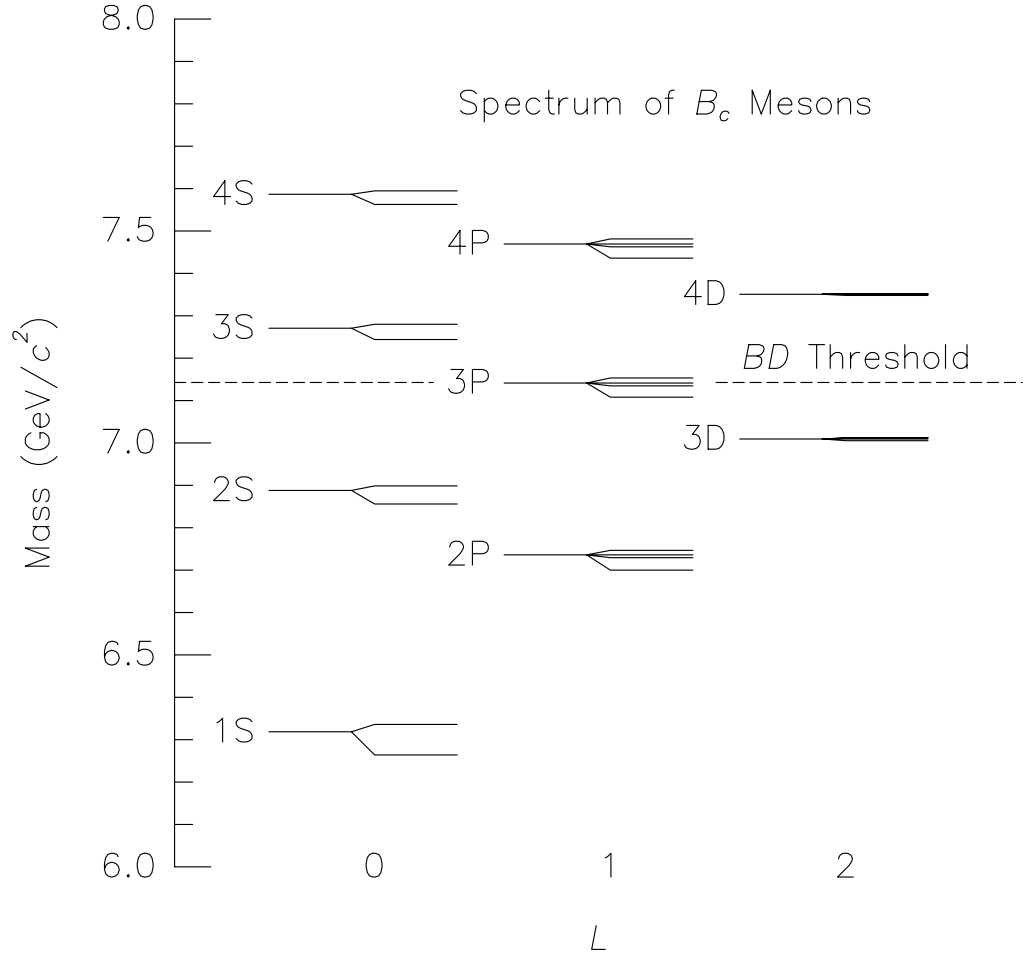


Figure 4: Theoretical B_c mass spectrum showing level splittings. Resonant $c\bar{b}$ states above the dotted line rapidly decay to real $B + D$ mesons. Below this threshold, excited states cannot decay directly to light mesons unlike other (unflavored) quarkonia. Instead, they cascade via gluon or photon emission to the pseudoscalar ground-state. [28]

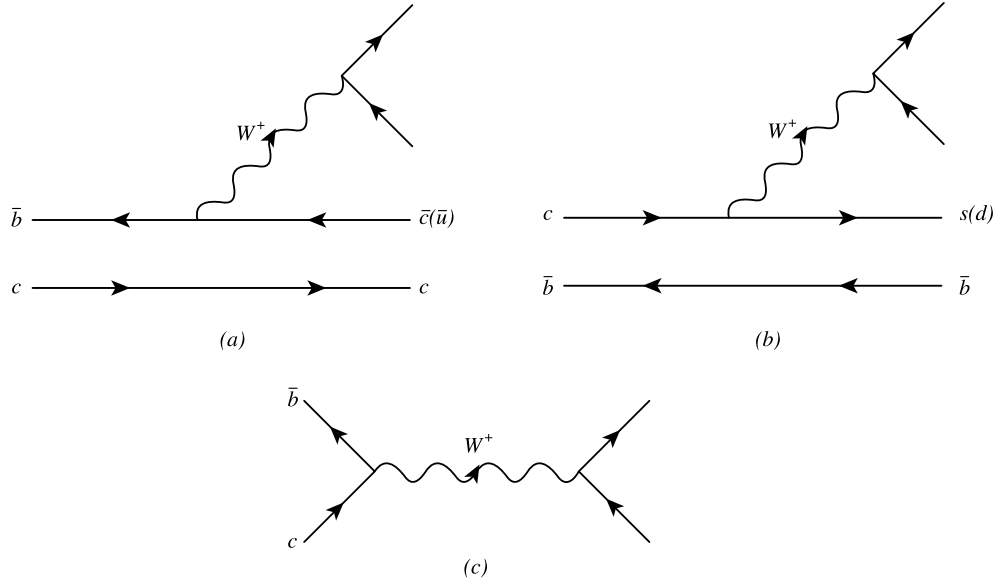


Figure 5: Schematic diagrams illustrating the three lowest-order decay subprocesses of the B_c . Figure (a) is c -quark spectator decay, (b) is \bar{b} -quark spectator decay, and (c) corresponds to annihilation.

1.2.4 Lifetime of the B_c Meson

The B_c can decay via three subprocesses: (a) the \bar{b} decays with the c -quark spectating, (b) the c -quark decays with the \bar{b} spectating, and (c) via an annihilation channel. These subprocesses are shown schematically in Figure 5.

The first is the same process that governs B^+ or B^0 decays, with the \bar{b} decaying either semileptonically

$$\bar{b} \rightarrow \bar{c}(\bar{u}) + l^+ \nu_l, \quad (l = e, \mu, \tau)$$

or hadronically

$$\bar{b} \rightarrow \bar{c}(\bar{u}) + u\bar{d}'(c\bar{s}').$$

The partial width of the B_c from the c spectator diagram should be similar to that of the corresponding diagram in B^0 decays. However, there is a

contribution from the mode $\bar{b} \rightarrow \bar{c} + c\bar{s}'$ which interferes destructively. The indistinguishability of the final-state c -quarks gives the B_c a slightly smaller partial width than that of the B^0 due to Pauli interference.⁹

The partial width of the B_c from the \bar{b} spectator diagram is similar to that responsible for D^0 (or D_s) meson decays; it is either semileptonic

$$c \rightarrow s' + l^+ \nu_l$$

or hadronic

$$c \rightarrow s' + \bar{d}'.$$

Since the mass of the spectator quark in this case is larger than that of the decaying c -quark, the B_c phase space available to the final-state B_c is diminished relative to the corresponding D meson decay, resulting in a smaller partial width (by a factor of $\simeq 0.6$, according to one calculation). [31]

The third subprocess of weak annihilation, while negligible for light mesons due to helicity suppression of the even lighter final-state particles, is not *a priori* negligible for B_c . Rather, the B_c can decay to a heavy τ lepton or c -quark in the final-state, which would not suffer from helicity suppression. In one potential model calculation, the contribution from $B_c \rightarrow c + \bar{s}'$ is estimated to be about 5% of the total width. [31, 33]

Combining all of these contributions gives an initial estimate for the B_c lifetime:

$$\frac{1}{\tau_{B_c}} \simeq \frac{1}{\tau_B} + \frac{0.6}{\tau_{D^0}} + \Gamma_{ann}, \quad (1.4)$$

⁹There is a similar interference in the B^+ decay mode $\bar{b} \rightarrow \bar{c} + u\bar{d}'$. Experimentally, however, $\tau_{B^+} \approx \tau_{B^0}$, and the effect is not significant. One expects the effect to be smaller for B decays because there are two Cabibbo-allowed decay channels instead of one, thus diluting the interference term (which is responsible for a lifetime difference of 3 standard deviations in the D^0 - D_s system).

or

$$\tau_{B_c} \simeq 4.0 \times 10^{-13} \text{ s } (120 \text{ } \mu\text{m}). \quad (1.5)$$

A lifetime measurement that differed significantly from this estimate would indicate a breakdown of the simple spectator model and provide additional insight into initial- and final-state interactions in heavy-heavy mesons.

As Quigg [32] has pointed out, this may be too naïve a model to provide reliable predictions, however, since the \bar{b} and c -quarks are tightly bound. In this case, the spectator model should be modified by expressing the decay widths in terms of the effective quark masses, which are reduced by the binding energy. This method results in somewhat longer lifetimes, depending on the particular value assumed for the binding energy, up to a maximum of about 1.4 ps. The measured value of $0.46^{+0.18}_{-0.16} \pm 0.03$ ps [13] indicates that despite the strong binding, the naïve spectator model still gives a reasonable estimate of the B_c lifetime.

1.2.5 Branching Ratios of the B_c

To precisely measure the B_c mass, the decay must be fully reconstructed via hadronic decay modes. As mentioned earlier, modes containing a final-state J/ψ provide a unique decay signature and should have a significant branching fraction owing to the initial charm content and the large branching ratio of $\bar{b} \rightarrow \bar{c}$. The dominant such decay mode is

$$B_c \rightarrow J/\psi \pi^+.$$

This is also the easiest mode, experimentally, to identify since it contains only one charged track in addition to the J/ψ decay products.

Predictions of the decay width for a given channel are highly dependent on the assumed theoretical model. Estimates of the $B_c^+ \rightarrow J/\psi \pi^+$ decay width

calculated in the framework of non-relativistic quark potential models have been performed [33] and give consistent values of the branching ratio:

$$\mathcal{B}^{NRQPM}(B_c^+ \rightarrow J/\psi\pi^+) \simeq 0.2\%.$$

These potential models are expected to be most applicable for low P_T (in the B_c rest frame) of the J/ψ . One can also model the hard recoil of the J/ψ from the exchange of a hard gluon between the decaying quark and the spectator, which is calculable in perturbative QCD, and factorize this hard gluon exchange from the soft nonperturbative binding process. This calculation [34] gives a branching ratio:

$$\mathcal{B}^{HS}(B_c^+ \rightarrow J/\psi\pi^+) = (2.0 \pm 0.5)\%.$$

Such large variations in theoretical predictions are clearly indicative that measurements of the hadronic branching fractions will provide important insight into the energy scales at which the various theoretical tools for QCD calculation involving heavy quarks are applicable.

Table 4 provides a tabulation of branching ratios into various decay modes as calculated by Chang and Chen [35] in a typical potential model. In addition to the $B_c^+ \rightarrow J/\psi\pi^+$ decay mode, this analysis also searches for the mode $B_c^+ \rightarrow J/\psi\pi^+\pi^-\pi^+$, which is expected to have the next-largest branching fraction. The diagrams leading to this decay mode are identical to the $J/\psi\pi^+$ mode, except that instead of a $J/\psi(1S)$ produced in the final-state, a $J/\psi(2S)$ is produced instead with the subsequent decay

$$J/\psi(2S) \rightarrow J/\psi(1S)\pi^+\pi^-,$$

or with an $a_1(1260)^+$ produced instead of a final-state π^+ , with the a_1 decaying via

$$a_1(1260)^+ \rightarrow \pi^+\rho^0; \rho^0 \rightarrow \pi^+\pi^-,$$

| <i>Semileptonic Decay</i> | <i>Decay Rate</i> |
|--|------------------------|
| $B_c^+ \rightarrow J/\psi + e^+ \nu_e$ | 34.4 |
| $B_c^+ \rightarrow J/\psi(2S) + e^+ \nu_e$ | 1.45 |
| <i>Hadronic Decay</i> | <i>Decay Rate</i> |
| $B_c^+ \rightarrow J/\psi + \pi^+$ | 3.29 |
| $B_c^+ \rightarrow J/\psi + \rho^+$ | 9.45 |
| $B_c^+ \rightarrow J/\psi + K^+$ | 0.242 |
| $B_c^+ \rightarrow J/\psi + D^+$ | 0.382×10^{-6} |
| $B_c^+ \rightarrow J/\psi(2S) + \pi^+$ | 0.398 |

Table 4: B_c exclusive branching ratios in a typical potential model. These are theoretical values derived from one specific model and, as such, should be used as guidelines only. Additional care should be taken in comparing semileptonic to hadronic decays, as these are calculated independently and may use different constants. Decay rates are in 10^{-6} eV.

or alternatively, via non-resonant decay into $J/\psi(1S)\pi^+\pi^-\pi^+$.

As a comparison with known branching fractions of the B^0 , the PDG [7, p. 40] values of $B^0 \rightarrow D^-\pi^+$ and $B^0 \rightarrow D^-\pi^+\pi^-\pi^+$ are, respectively, $(3.0 \pm 0.4) \times 10^{-3}$ and $(8.0 \pm 2.5) \times 10^{-3}$.

1.3 Previous CDF limit on $B_c^+ \rightarrow J/\psi\pi^+$

A search for $B_c^+ \rightarrow J/\psi\pi^+$ in the Run I data at CDF has already been performed which predates the CDF B_c discovery. [36] This analysis measured an upper limit as a function of assumed B_c lifetime in order to cover the entire theoretical range of lifetime values. The $\sigma \cdot \mathcal{B}^{10}$ for $B_c^+ \rightarrow J/\psi\pi^+$ is normalized to that of $B^+ \rightarrow J/\psi K^+$ in order to cancel theoretical uncertainties on the production cross section of the b -quark, as well as systematic effects of the J/ψ trigger and the track finding efficiency in the detector. The remaining differences are due primarily to decay kinematics, which can be modeled by Monte Carlo methods. To a lesser degree, they are also due to the b -quark hadronization mechanism, which can be parameterized in terms of a small (usually one) number of parameters and can therefore also be modeled. The current 95% confidence level limit on $\frac{\sigma(B_c^+) \cdot \mathcal{B}(B_c^+ \rightarrow J/\psi\pi^+)}{\sigma(B_u^+) \cdot \mathcal{B}(B^+ \rightarrow J/\psi K^+)}$, as measured at CDF [36] varies from 0.15 for an assumed B_c lifetime of 0.17 ps to 0.040 for a lifetime of 1.6 ps. This represents the world's best limit on $\frac{\Gamma(B_c^+ \rightarrow J/\psi\pi^+)}{\Gamma_{total}} \times \mathcal{B}(\bar{b} \rightarrow B_c)$, which varies from 5.7×10^{-5} to 1.5×10^{-5} for $0.17 \text{ ps} < \tau_{B_c} < 1.6 \text{ ps}$. (Using the values of $\mathcal{B}(b \rightarrow B^+) = 0.397_{-0.022}^{+0.018}$ and $\mathcal{B}(B^+ \rightarrow J/\psi(1S)K^+) = (9.9 \pm 1.0) \times 10^{-4}$.) [7, p. 40] The lifetime measurement provided by the discovery paper greatly

¹⁰ σ denotes the cross section for production of a specific particle, and \mathcal{B} is the branching ratio of that particle to a specified decay mode. The quantity $\sigma \cdot \mathcal{B}$ then represents an absolute measure of how often a decay process occurs for a given beam luminosity and center-of-mass energy.

reduces reliance on conservative upper limits necessary to cover the entire theoretical range of B_c lifetimes, so it may now be possible to obtain an improved upper limit. The current best limit on $\Gamma(J/\psi(1S)\pi^+\pi^-\pi^+)/\Gamma_{total} \times \mathcal{B}(\bar{b} \rightarrow B_c)$ is $< 5.7 \times 10^{-4}$ at 90% C.L. from the DELPHI experiment. [37] It should be possible to improve on this limit using CDF's advanced vertexing capabilities. Table 5 and Figure 6 summarize the results of the previous CDF B_c hadronic decay search.

| <i>Lifetime</i> | <i>cτ Cut</i> | $\epsilon_{rel} = \frac{\epsilon(B_u^+)}{\epsilon(B_c^+)}$ | N_{tot} | N_{bkg} | 95% C. L. |
|-----------------|-------------------------------|--|-----------|----------------|-----------|
| 0.17 ps | 60 μm | 2.50 ± 0.15 | 40 | 29.2 ± 2.6 | 0.15 |
| 0.33 ps | 85 μm | 2.10 ± 0.12 | 25 | 16.5 ± 2.1 | 0.10 |
| 0.50 ps | 100 μm | 1.84 ± 0.11 | 18 | 12.7 ± 1.7 | 0.070 |
| 0.80 ps | 150 μm | 1.80 ± 0.10 | 10 | 5.9 ± 1.2 | 0.053 |
| 1.0 ps | 150 μm | 1.61 ± 0.09 | 10 | 5.9 ± 1.2 | 0.046 |
| 1.3 ps | 150 μm | 1.43 ± 0.08 | 10 | 5.9 ± 1.2 | 0.042 |
| 1.6 ps | 150 μm | 1.35 ± 0.07 | 10 | 5.9 ± 1.2 | 0.040 |

Table 5: Results of previous CDF B_c hadronic decay search. Rows in this table correspond to various choices of the assumed B_c lifetimes, the $c\tau$ selection criterion used for each choice, the relative efficiency of the selection cuts, the total number of data events in the largest four consecutive mass bins from 6.1 to 6.4 GeV, the number of background events in those four bins (including statistical error), and the 95% C.L. limit for the $\sigma \cdot \mathcal{B}$ ratio.

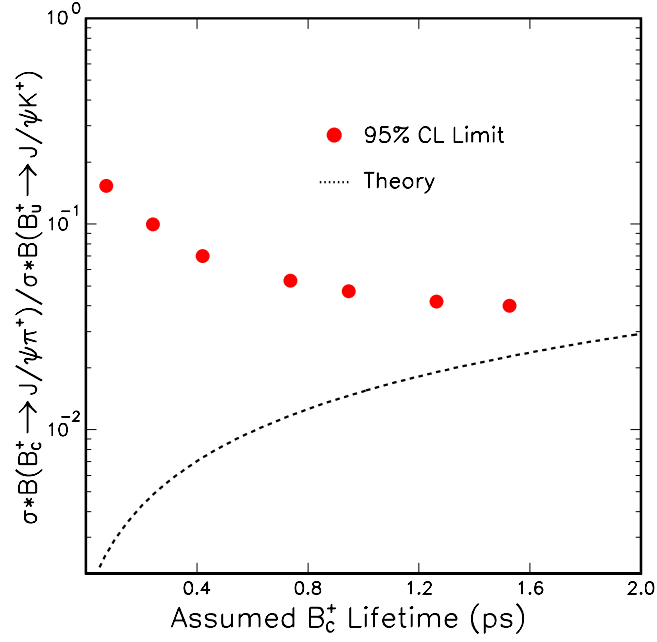


Figure 6: Previous CDF limit on $B_c^+ \rightarrow J/\psi \pi^+$. [36] Circular points show 95% C.L. limits on ratio of $\sigma \cdot \mathcal{B}$ for $B_c^+ \rightarrow J/\psi \pi^+$ relative to $B^+ \rightarrow J/\psi K^+$ as a function of B_c lifetime. The dotted curve represents a theoretical calculation of the same ratio based on the assumptions that B_c is produced 1.5×10^{-3} times as often as all other B mesons and that $\Gamma(B_c^+ \rightarrow J/\psi \pi^+) = 4.2 \times 10^9 \text{ s}^{-1}$.

Chapter 2

Experimental Apparatus

2.1 Introduction

The data used in this analysis were gathered by a general purpose experiment for the studying $p\bar{p}$ collisions. The general features of the collider facility and a description of the detector components are presented here.

2.2 Tevatron

2.2.1 Introduction

The Tevatron is a proton synchrotron located at the Fermi National Accelerator Laboratory in Batavia, Illinois. Figure 7 shows a schematic layout of the Tevatron and its main components. Protons and antiprotons are guided by magnetic fields to circulate in opposite directions around a ring 1 km in radius. Currently the highest energy accelerator in the world, the Tevatron can be operated in “fixed target” or “collider” modes. In the collider mode, the protons and antiprotons are stored in six bunches each and collide at various points around the ring every $3.5 \mu\text{s}$ with a center-of-mass energy of 1.8 TeV. Two of the collision points are instrumented with detectors, known as D0¹¹ and CDF. The analysis presented here is based on data collected by the CDF experiment. The bunch sizes are typically Gaussian in shape with a longitudinal spread of $\sigma_z \simeq 30 \text{ cm}$ and transverse radius $\sigma_{xy} \simeq 40 \mu\text{m}$ at the collision points. The number of inelastic collisions is proportional to a quantity called “luminosity,”

¹¹The collision points are designated A0, B0, C0, D0, E0, and F0. The D0 detector is, appropriately, located at the D0 collision point.

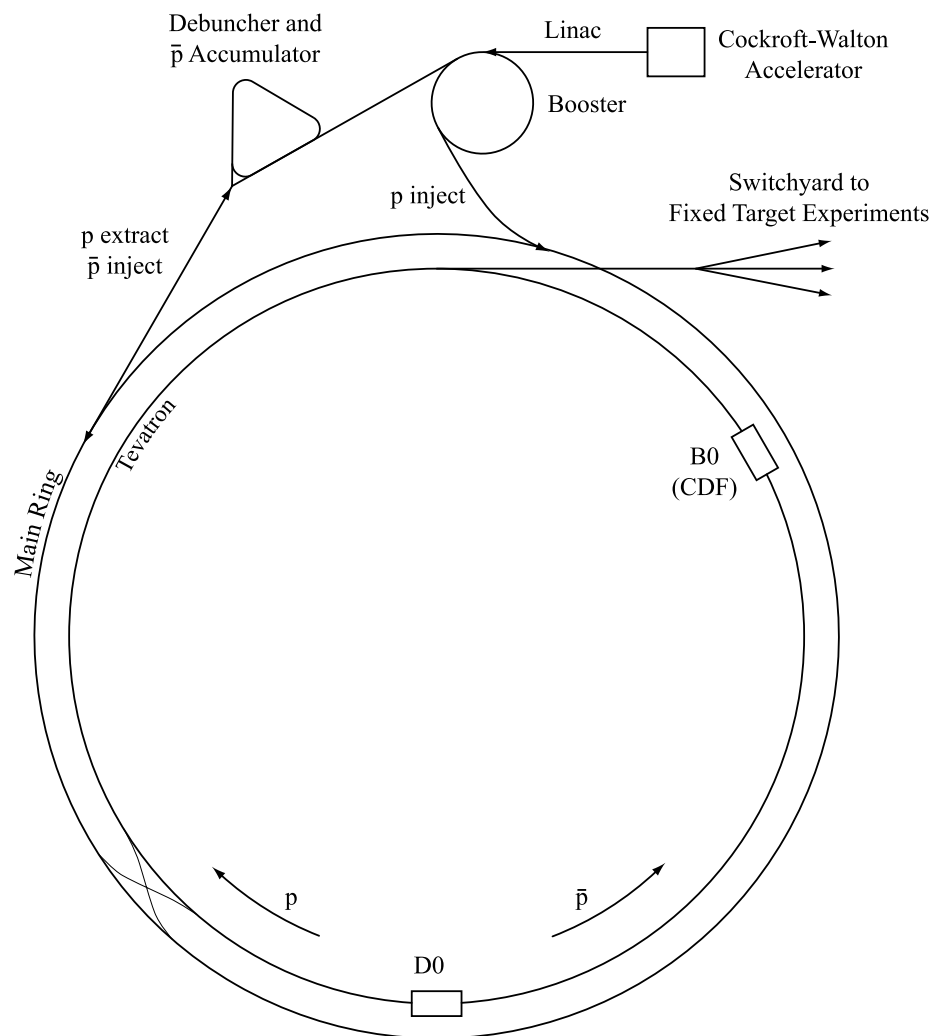


Figure 7: Schematic layout of Fermilab accelerator. Principal components are labeled. Arrows indicate directions of particle flow.

which is a measure of how often a collision opportunity presents itself. The proportionality factor is the “cross section” for the process. Luminosity is calculated as follows:

$$\mathcal{L} = \frac{N_{bunch} N_p N_{\bar{p}} f}{4\pi\sigma^2}, \quad (2.1)$$

where $\sigma \simeq 40 \mu\text{m}$ is the characteristic transverse beam size, N_{bunch} is the number (6) of bunches, N_p is the number of protons per bunch (typically about 2×10^{11}), $N_{\bar{p}}$ is the number of antiprotons per bunch (anywhere from 2 to 9×10^{10} , depending on how long antiprotons are accumulated before each store), and f is the frequency of circulation for each bunch (50 kHz). A small beam size obtained by focusing the beam with quadrupole magnets is desirable for maximum luminosity, but is limited by Coulomb repulsion of (anti-)protons in the bunch. Accumulation of antiprotons is inherently more difficult than production of protons, so $N_{\bar{p}}$ is generally the limiting factor in the luminosity equation. The average luminosity for Run Ib (1994-95)¹², during which the bulk of the data was taken, was $8 \times 10^{30} \text{ cm}^{-2} \text{ s}^{-1}$. The cross section for a “minimum-bias”¹³ event is about 50 mb, so there were approximately 1.4 inelastic collisions at each bunch crossing. The total number of events recorded by CDF during all of run I corresponded to an integrated luminosity of roughly $\int \mathcal{L} dt \approx 110 \text{ pb}^{-1}$.

¹²The Tevatron operated in colliding-beam mode during two principal data-taking periods, designated Run Ia (1992-93) and Run Ib (1994-95). The CDF detector was upgraded during the downtime between these runs. Two additional runs, Run -1 in 1987, and Run 0 in 1989, did not implement the full set of analysis triggers and were used primarily for calibration and parameterization of the detector performance.

¹³A minimum-bias event corresponds to a scattering event which produced hits in the beam-beam counters, which lie just off the collision axis.

2.2.2 Operation of the Tevatron

Protons are injected into the collider by accelerating negatively charged hydrogen gas in a Cockcroft-Walton accelerator to an initial energy of 750 keV, then stripping the electrons and accelerating the protons to 200 MeV in a linear accelerator. The bunches emerging from the linac are injected into a small circular accelerator called the Booster Ring, which accelerates them to 8 GeV before injection into the Main Ring, which lies above the Tevatron. The Main Ring accelerates the bunches to 150 GeV and transfers them to the Tevatron, where they are ramped up to 900 GeV.

The antiprotons are produced by accelerating protons in the Main Ring to 120 GeV and colliding them with a fixed nickel target. A fraction of these collisions will produce antiprotons with a broad range of energies and angles, which are passed into a “debuncher” ring. Here, the beam is stochastically cooled by monitoring the orbit of each antiproton and giving it a corrective “kick” at a later point in its orbit. Eventually, the result is a substantial number of antiprotons traversing a known trajectory with a narrow beam size. These are sent into the accumulator for storage until a sufficient quantity is obtained to begin collisions with the protons.

2.3 CDF Detector

The CDF detector is a multipurpose solenoidal magnetic spectrometer surrounded by complete azimuthal coverage of calorimetry and additional chambers designed to detect muons. The design of CDF reflects the desire to be as sensitive as possible to a wide range of physics events. Figure 8 illustrates a cross section of the CDF detector. Detector components relevant to this analysis are described in further detail in the following sections.

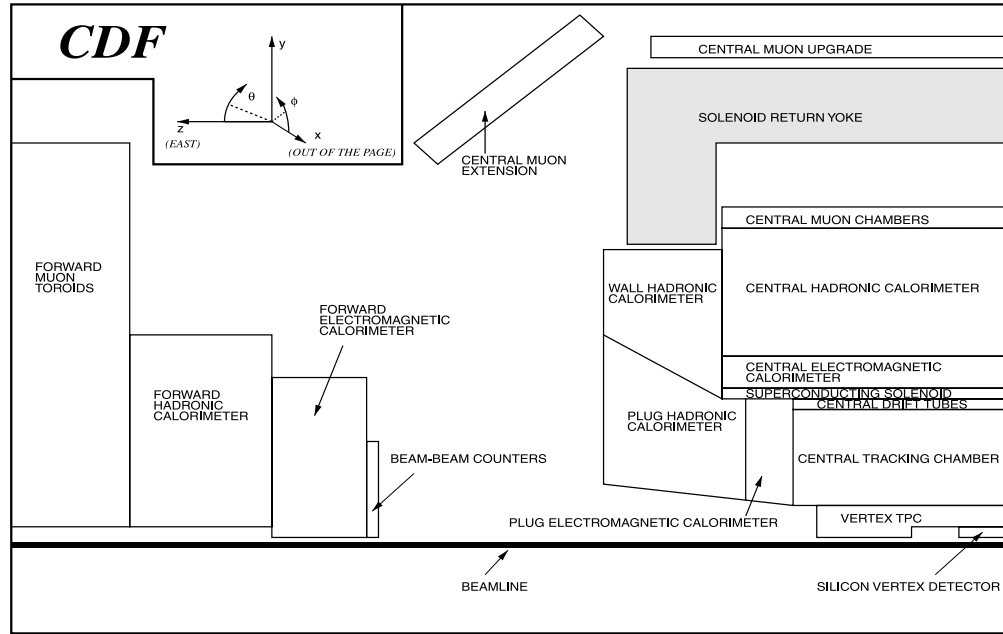


Figure 8: One quadrant of the CDF detector in cross section view (r - z plane), showing relative dimensions and layout of detector elements. Detector is symmetric in z and has rotational symmetry in the x - y plane.

2.3.1 CDF Coordinate System

The elements of the CDF detector have discrete azimuthal symmetry, and exhibit forward-backward symmetry around the interaction region. The orthonormal coordinate system¹⁴ is defined such that \hat{z} points along the direction of the proton beam (east), \hat{y} points up, and \hat{x} points north (making it a right-handed system). The origin of this coordinate system corresponds to the center of the detector and the nominal $p\bar{p}$ interaction point.

In cylindrical coordinates, r is the distance from the z -axis and ϕ is the azimuthal angle, with $\phi = 0$ at $x = r$, $y = 0$. The polar angle θ is defined as $r = z \tan \theta$. Since minimum-bias events are distributed roughly uniformly in rapidity, it is sometimes useful to define a quantity in the CDF coordinate system that corresponds to the kinematic rapidity $y = (2 \log(\frac{E+p_z}{E-p_z}))^{-1}$ in the limit of massless particles. This quantity is usually referred to as “pseudorapidity” and is defined by $\eta = \tanh^{-1}(\cos \frac{\theta}{2})$. Because particles are produced approximately uniformly in pseudorapidity, the calorimetry is segmented in units of η and the extent of various detector components is usually quoted in units of η .

The path of a stable¹⁵ charged particle traversing a uniform magnetic field is a helix. Thus, each track can be assigned five helix parameters, denoted c, ϕ_0, z_0, d_0 , and λ , that completely describe its trajectory. The curvature, c , is signed according to the helical orientation, such that a positively-charged particle has a positive curvature. The angle ϕ_0 is the starting angle (in the x - y

¹⁴For clarity, I will rarely make specific reference to this coordinate system. Where possibly I will refer to quantities using cylindrical coordinates, unless there is no harm in mixing up the sign of a particular coordinate, *e.g.*, $P_T = \sqrt{p_x^2 + p_y^2}$.

¹⁵By “stable,” I mean on the timescale it takes to traverse the detector. Muons are not stable, but have a very long lifetime and can travel hundreds of meters before decaying.

plane) of the trajectory at its closest approach to the z -axis; the z -coordinate at this point is z_0 , and d_0 is the distance of closest approach in the transverse plane. The distance d_0 is signed such that the (x,y) coordinates of the point of closest approach are $(-d_0 \sin \phi_0, d_0 \cos \phi_0)$. The slope parameter, λ , is defined as $\lambda = \frac{p_z}{p_T} = \cot \theta$. The d_0 of a track is commonly referred to as the “impact parameter.”

2.3.2 Superconducting Solenoid

In order to measure a charged particle’s momentum, one may equivalently measure its curvature in a magnetic field. For a magnetic field in the \hat{z} direction, the component of momentum transverse to the magnetic field (P_T) is determined by $P_T = 0.3B\rho$; when B is measured in Tesla, ρ is the track turning radius in m, and P_T is measured in GeV. At CDF, the magnetic field is produced by a superconducting solenoid located outside of the tracking region, but inside the calorimeters ($r = 1.5$ m, $|z| < 2.4$ m). The nominal field strength is 1.4116 T, and is uniform to better than 0.1% within the tracking volume. Nonuniformities in the magnetic field strength were measured during construction and are part of a database used to properly fit tracks during offline event reconstruction. During data taking periods, nuclear magnetic resonance probes monitor the field strength and adjust the database accordingly. A final check of the magnetic field is performed by reconstructing J/ψ events and ensuring that the measured mass value agrees with the PDG value.

2.3.3 Silicon Vertex Detector (SVX’)

The component of the detector closest to the beamline, through which tracks first travel, is a four-layer silicon microstrip detector. The original detector,

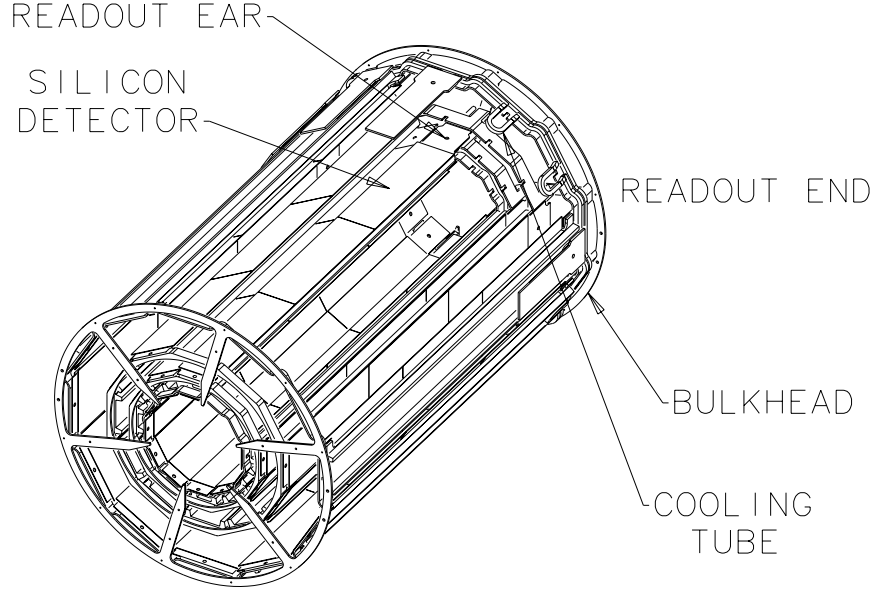


Figure 9: Schematic rendering of SVX' barrel, showing primary components and arrangement of silicon ladders.

installed in 1990, was called “SVX” and was used during the Run Ia data-taking period. For Run Ib, the SVX was upgraded with radiation-hard readout chips to withstand the additional luminosity. The geometry of this newer “SVX'” is almost identical to that of the original SVX.

The SVX' is composed of two cylindrical barrels with a total active length of 51 cm, which provides acceptance for about 60% of the collision vertices. Figure 9 shows a schematic drawing of one of the SVX' barrels. Each barrel has four concentric layers of $300\text{ }\mu\text{m}$ thick silicon sensors divided into $60\text{ }\mu\text{m}$ strips ($55\text{ }\mu\text{m}$ on the outer layer), segmented azimuthally. This fine segmentation allows for precise reconstruction of event vertices. It also allows identification of collision vertices and location of secondary vertices displaced from the production vertex, which are indicative of long-lived particles such as

B mesons. Such events can then be separated from so-called “prompt” events, which have zero lifetime. The layers are located at $r = 2.9$ cm, $r = 4.3$ cm, $r = 5.7$ cm, and at $r = 7.9$ cm; and they are subdivided into twelve 30° wedges in azimuthal angle.

SVX’ “hits” are formed by performing a pedestal subtraction of the charge collected on each strip. Then the strips are clustered according to an algorithm designed to reject spurious noise hits. This clustering algorithm requires groups of contiguous strips with 4 times the noise level for 1-strip clusters, 2.5 times the noise level for 2-strip clusters, and 2 times the noise level for 3(or more)-strip clusters. The impact parameter resolution for tracks with both CTC and SVX information combined can be described by¹⁶

$$\sigma_d = 10 \text{ } \mu m + \frac{40}{P_T} \text{ } \mu m \text{ GeV}. \quad (2.2)$$

The position resolution for 1-strip clusters is determined to be $13 \text{ } \mu m$ from fits using only SVX’ tracking information, and $11 \text{ } \mu m$ for 2-strip clusters.

Identification of long-lived B mesons relies on the ability to measure a secondary decay vertex displaced from the primary interaction vertex. The SVX’ is unique among the CDF detector components in its ability to provide precise impact parameter and decay length information, and therefore is essential to the search for B_c mesons at CDF. The vertexing capabilities of the SVX’ also provide a means of measuring the run-averaged beam position, which can vary due to the Tevatron operating conditions.

¹⁶Normally, errors would be combined in quadrature. Empirically, adding the terms linearly gives a good fit to the d_0 resolution.

2.3.4 Vertex Tracking Chamber (VTX)

The VTX consists of 28 time projection chambers (TPC's), 9.4 cm in length and segmented octagonally in azimuth. It is designed to measure the z -position of interaction vertices, because the SVX provides virtually no z information. The VTX is segmented to provide 24 z measurements between $6.5 \text{ cm} < r < 21 \text{ cm}$ for $85 \text{ cm} < |z| < 132 \text{ cm}$ and 16 z measurements between $11.5 \text{ cm} < r < 21 \text{ cm}$ for $|z| < 85 \text{ cm}$.¹⁷ The overall z vertex resolution is roughly 2 mm. The z positions of primary vertices are used to guide the track reconstruction in the CTC in the $r - z$ plane, to match tracks with the appropriate vertex when multiple production vertices are present, and to correct the $x - y$ beam position for the overall slope of the beamline.

2.3.5 Central Tracking Chamber (CTC)

The CTC is a cylindrical drift chamber which lies outside the VTX and extends to 1.38 m in radius and covers 3.2 m in z . It is filled with an argon-ethane (50% – 50%) gas mixture, which is ionized by charged particles traversing the detector. The electrons produced in the ionization drift to sense wires arranged in alternating “superlayers” of five axial (with 12 wires each) and four small-angle stereo (with 6 wires each, tilted at 2.5 degrees with respect to z) layers. Each plane of sense wires is tilted 45° in azimuth, corresponding to the Lorentz angle of electrons drifting at $51 \mu\text{m/s}$ in the 1.4 T magnetic field. Figure 10 is a diagram of the CTC endplate. The diagram shows the locations of both the sense wire planes and the field wire planes. The wires are spaced such that the maximum drift time is less than 800 ns (40 mm). The

¹⁷The change in thickness corresponds to the physical location of the SVX', which would otherwise overlap the VTX in r .

tilt angle of the drift cells allows for high- P_T tracks to sample the full range of drift times. This is of dual benefit: it makes calibration of the drift time-to-drift distance relationship simpler, and it guarantees that high- P_T tracks will contain some hits arriving early in the time window. This latter feature offers the opportunity to trigger on high- P_T tracks before all of the hit information is collected. [38] The time development of signals on each sense wire is read out with TDC's¹⁸ capable of storing multiple hits. Both the leading and trailing edges of the incoming pulses are recorded in bins of 2 ns. The distribution of pulse widths is such that multiple tracks may be resolved if their separation is > 0.2 cm. The CTC track parameter resolutions are measured¹⁹ to be

$$\frac{\sigma_{P_T}}{P_T^2} = 0.10\% \text{ GeV}^{-1}, \sigma_d = 0.07 \text{ cm}, \sigma_z = 1.0 \text{ cm}.$$

The primary function of the CTC is to measure track momenta, and therefore plays a central role in this analysis. Identifying muons originating from a J/ψ requires precise reconstruction of their invariant mass, calculated from the track momenta. Likewise, additional tracks added to the J/ψ vertex must be well-measured in order to distinguish an excess of events in the B meson mass spectrum.

2.3.6 Central Calorimeters

Outside of the tracking region and the solenoid lies the calorimetry. In the central region, the electromagnetic and hadronic calorimeters form projec-

¹⁸Time to Digital Converters.

¹⁹Resolutions on the CTC track parameters are determined by performing an *in situ* calibration of the detector using actual tracks in the data. These particular values correspond to calibrations performed on Run Ib data. Momentum resolution assumes that the track momentum is large enough that the multiple scattering contribution can be neglected.

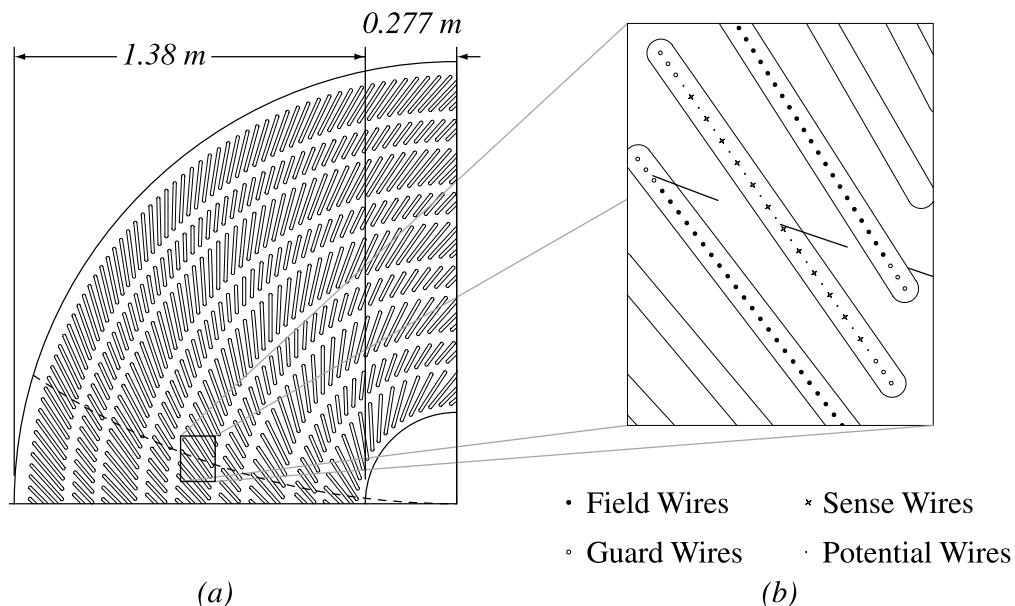


Figure 10: (a) One quadrant of the CTC endplate, showing location of sense and field wire planes as seen from the western end of the detector. For illustrative purposes, the dotted line represents a 1 GeV positively-charged track. (b) Expanded view of one axial superlayer. Locations of wire types are indicated. The presence of the potential wires, which are not instrumented, provides for independent control of the gain on the sense wires (governed by the field strength near the wire where the final “avalanche” of charge occurs) and the field strength in the drift region.

tive towers that are subdivided to cover 0.1 units of η and 15° in ϕ . The EM calorimeters use lead absorbers and doped polystyrene scintillator which produces predominantly low-energy photons (blue light) when ionized. The central EM calorimeter (CEM) provides electron and photon energy measurements with a resolution of

$$\frac{\sigma_E}{E} = \frac{13.5\%}{\sqrt{E_T(\text{GeV})}} \oplus 1.5\%.$$

Beyond the CEM towers are the central hadronic calorimeter (CHA) towers, which contain layers of iron absorber and plastic scintillator to measure the energy of hadronic jets.

The calorimeter system is not used in this analysis except as an absorber preventing hadronic particles from reaching the muon detectors.²⁰

2.3.7 Central Muon Chambers

The Central Muon (CMU) chambers contain four layers of drift chambers measuring 6 cm by 2.7 cm by 2.2 mm in thickness, each with a single 50 μm stainless steel sense wire through the center along the z direction. It covers about 84% of the solid angle for $|\eta| < 0.6$. After the hadrons have deposited their energy in the calorimeters (except for a small “punch-through” fraction), the only charged particles that can reach the CMU are muons with $P_T > 1.4 \text{ GeV}$.

In 1992, an additional 60 cm of steel and four more layers of drift chambers for extra hadron absorption and greater muon detection were added. This is called the Central Muon Upgrade (CMP). It covers about 63% of the solid angle for $|\eta| < 0.6$.

²⁰The pion and kaon punch-through fraction is $\sim 0.2\%$ for the central muon chambers.

An additional set of free-standing conical arches, called the Central Muon Extension (CMX), provides greater coverage of the central region. These contain drift chambers layered between scintillator counters for coincidence triggering. It covers about 71% of the solid angle for $0.6 < |\eta| < 1.0$.

Figure 11 maps the η - ϕ coverage of each muon system. Figure 12 shows a schematic of the CMU drift chambers in cross section.

The decay of J/ψ into two muons provides a distinctive experimental signature for selecting data rich in B mesons, owing to their relatively large branching fractions into final-states containing a J/ψ . The central muon system provides the sole means to trigger efficiently on such events.

2.3.8 Beam-Beam Counter (BBC)

The BBC is a set of scintillating detectors located 5.8 m from $z = 0$ and covering 0.32° to 4.47° in ϕ . They are used for triggering of inelastic scattering events and to provide an estimate of the instantaneous luminosity. Events are only recorded if there is a coincidence between the BBC's within 15 ns. This acts as a “Level 0” trigger. Luminosity is determined by the number of collisions recorded during this 15 ns window.

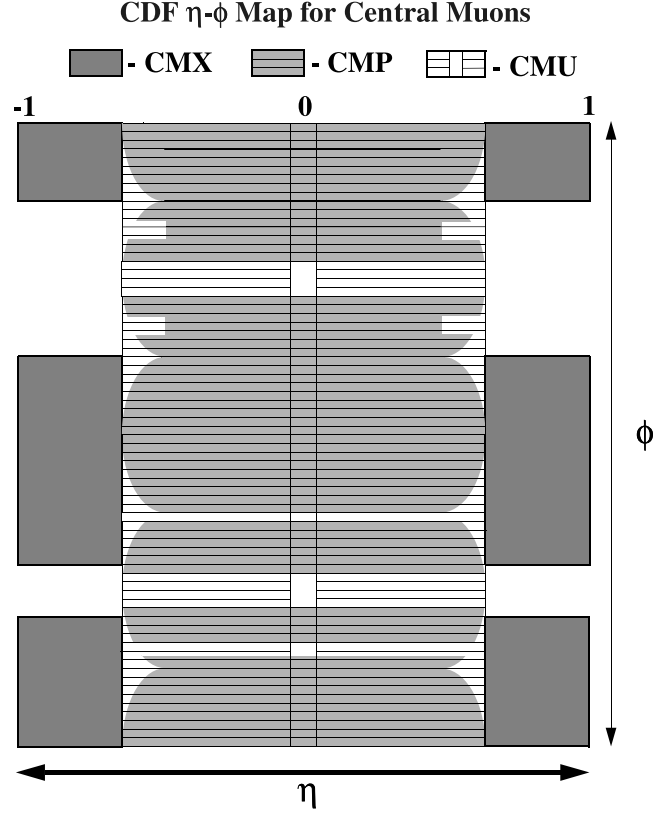


Figure 11: Schematic map showing coverage of the central muon chambers in (η, ϕ) . The forward muon system not shown as it is not used in this analysis. Where overlap occurs, drift chamber hits are used from all overlapping systems. Muon selection criteria are described more fully in Section 3.2.5.

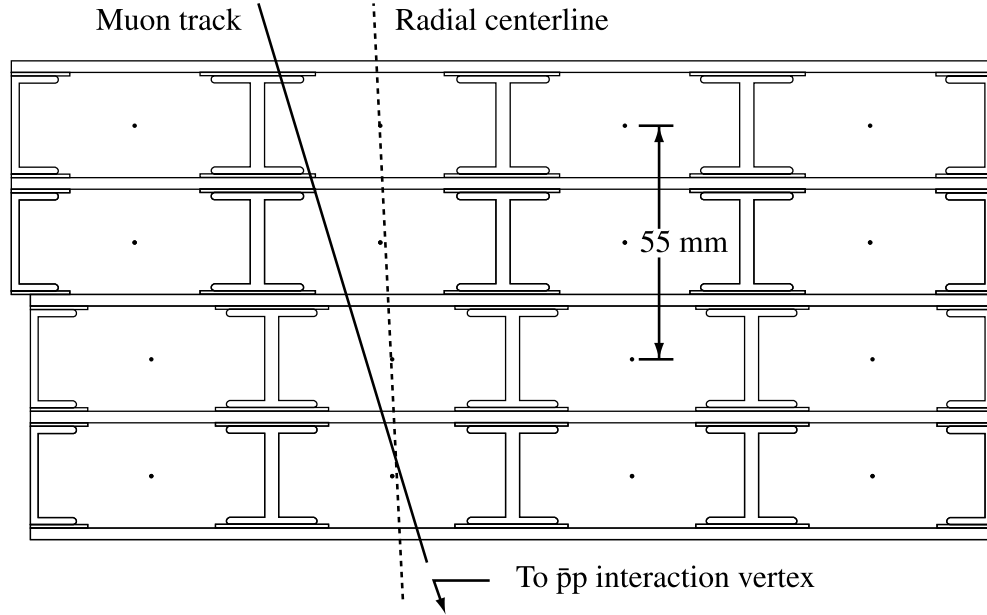


Figure 12: Cross Section of CMU drift chambers. Muon track positions are measured by sampling drift times in four layers. Evaluating track slope in the CMU prior to full event reconstruction in the tracking volume provides for a fast estimate of muon momentum for triggering purposes.

Chapter 3

Data Handling and Monte Carlo Simulation

3.1 Introduction

The collection of data at CDF involves a multi-stage triggering process and a large software base for the reconstruction and simulation of physics events. The aspects of this system relevant to the present analysis are described here.

3.2 Trigger Requirements

In the interaction region, the bunch-crossing rate is 286 kHz. With an average luminosity (during Run Ib) of $8 \times 10^{30} \text{ cm}^{-2} \text{ s}^{-1}$ and a 50 mb cross section for minimum-bias events, one observes an average of 1.4 interactions at every bunch-crossing, or an average minimum-bias event rate of $1.4 \times 286 \text{ kHz} = 400 \text{ kHz}$. At this high rate, it would be impossible (and wasteful) to read out all of the data (roughly 10^5 channels) for every inelastic collision. Interesting events are selected through a three-level trigger system, with increasing accuracy, specificity, and readout time at each successive trigger level. Events passing the level-3 trigger are written to tape for future analysis. The trigger requirements leading to the selection of events containing a final-state $J/\psi \rightarrow \mu^+ \mu^-$ are described here. Other triggers are searched concurrently during data-taking, such as events with large missing transverse energy, and central electron and photon candidates for other physics analyses which are not described here.

3.2.1 Level-1 Trigger

The first trigger level is a hardware trigger that scans events at every bunch-crossing. If there is a coincidence between the BBC's within a 15 ns window around the collision time, the muon chambers are scanned for hits. A combination of more than two hits in a given chamber is tentatively identified as a muon “stub.” The slope of this muon stub provides an initial estimate of the muon momentum. Figure 13 shows the efficiency of the level-1 trigger as a function of track P_T . The rate of the level-1 trigger is about 1 kHz, for a rejection factor of about 400. [39]

3.2.2 Level-2 Trigger

The level-2 dimuon trigger uses the algorithm alluded to in Section 2.3.5 to rapidly process CTC information by using the prompt hits to sort tracks according to their estimated P_T . Tracks are also extrapolated into the muon chambers to check for matching muon stubs. At this level, the P_T assigned to the muons via the CFT processor has a resolution of $\frac{\sigma P_T}{P_T^2} = 3.5\%$ GeV^{-1} . The level-2 dimuon trigger requires at least two level-1 CMU stubs, or one CMU and one CMX, or two CMX muon stubs. At least one of these must have a matching track from the CFT with $P_T > 2.5$ GeV. Table 6 outlines the various combinations of muon chambers and matching CFT tracks considered. These varying P_T thresholds of these triggers are applied after level-3. The rate of the level-2 dimuon trigger is about 15 Hz (a rejection factor of $\simeq 70$, relative to level-1), and its efficiency as a function of track P_T is shown in Figure 14. The longer decision time of level-2 ($\simeq 40$ μs), combined with the level-1 trigger rate of 1 kHz results in a 4% dead time during which events were not recorded.

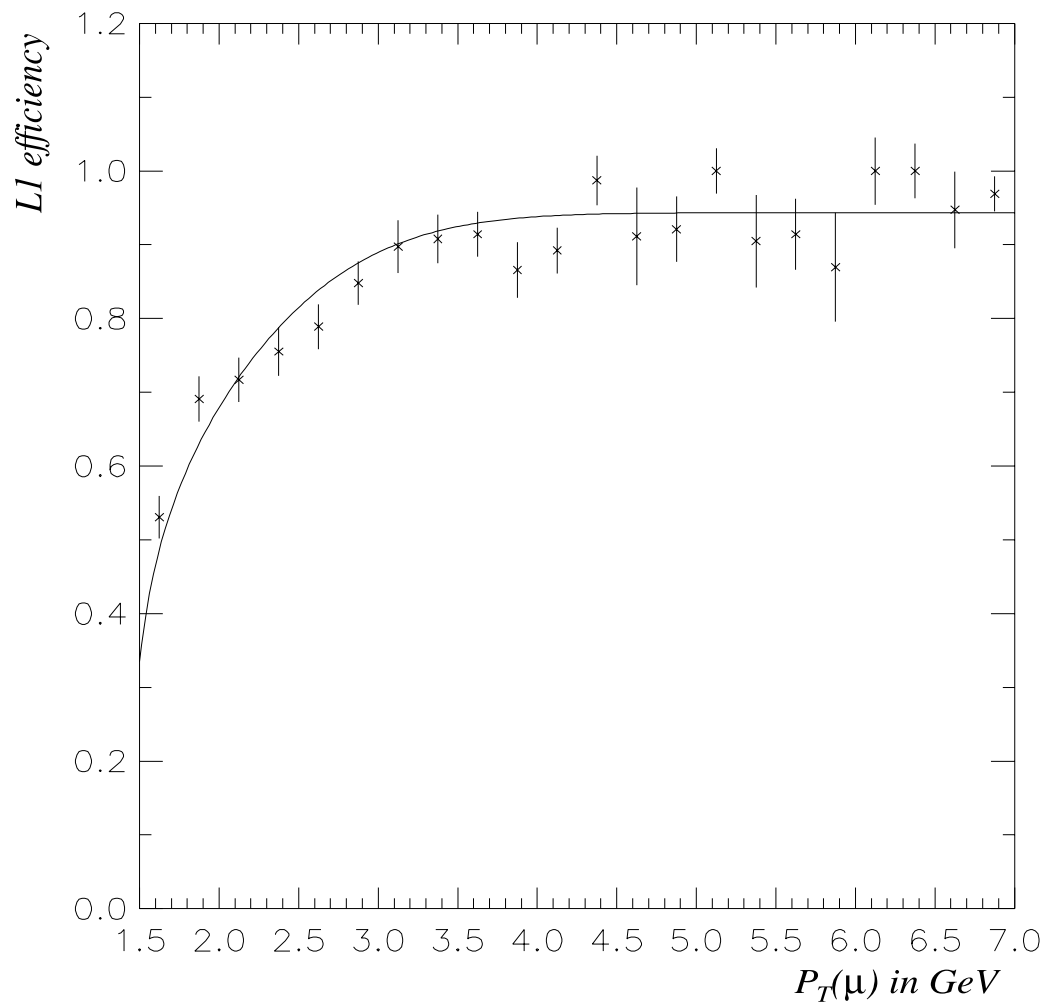


Figure 13: Efficiency of Level-1 muon trigger as a function of P_T of the muon.

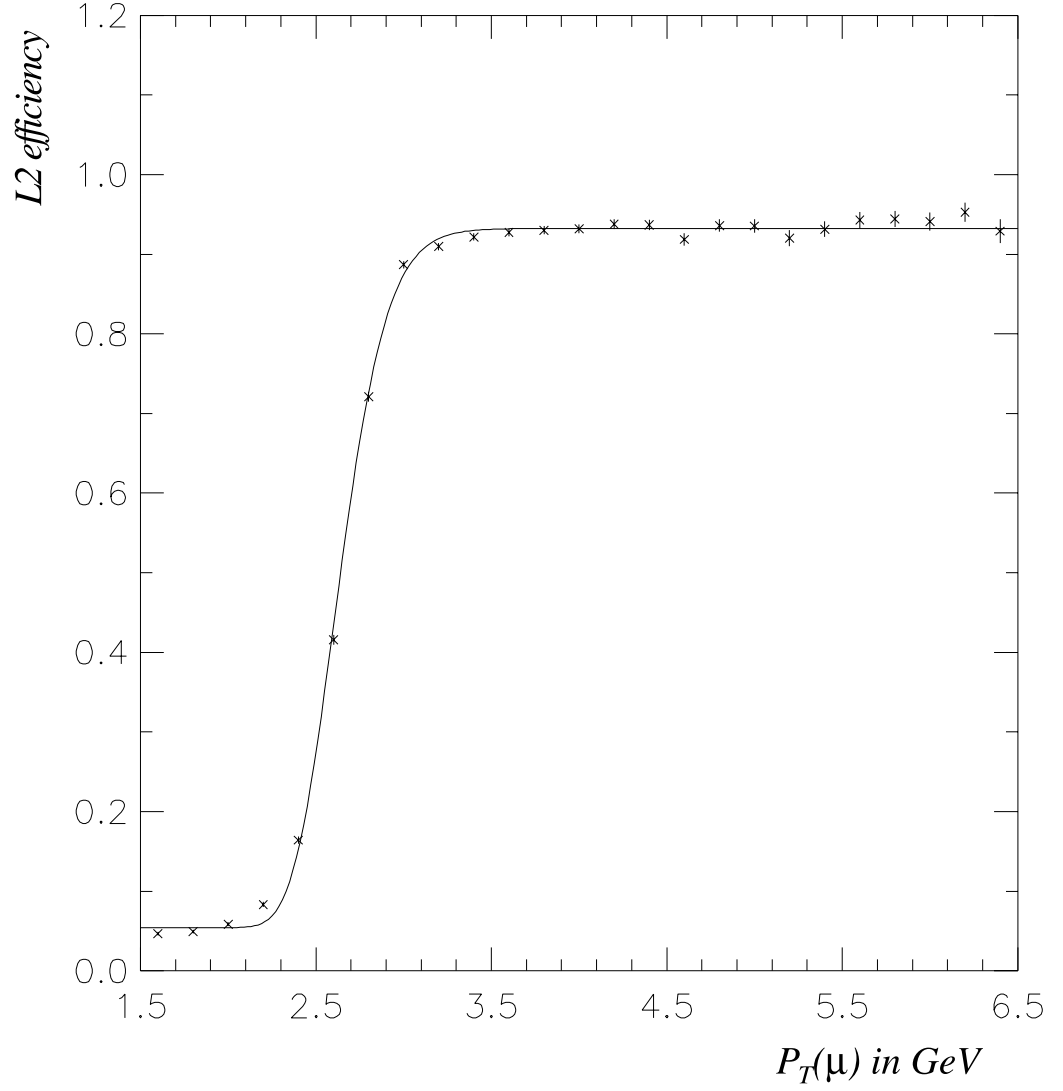


Figure 14: Efficiency of Level-2 muon trigger as a function of P_T of the muon.

3.2.3 Level-3 Trigger

The level-3 dimuon trigger uses fully reconstructed tracks in the CTC to measure momentum. Matching requirements between the CTC and central muon stubs are more stringent (tracks must match to within 4 standard deviations), and the invariant mass of the dimuon pair must lie between 2.8 and 3.2 GeV (the world-average J/ψ mass is 3.09688 ± 0.00044 GeV. [7, p. 46]) Additionally, the muon candidates must be separated by a calorimeter tower to remove background from punch-through hadronic jets. Figure 15 shows the invariant mass distribution for dimuons passing level-3. The trigger rate of dimuons for level-3 prior to the mass cut is about 6 Hz, providing an additional rejection factor of 2.5. The readout time for all the detector channels necessary for complete event reconstruction is about 3 ms. With a level-2 rate of 15 Hz, this corresponds to an additional 4.5% dead time. All events passing the level-3 triggers are written to tape.

3.2.4 Offline Reconstruction

A certain fraction of events passing the level-3 triggers are cached on disk for rapid processing by a cluster of UNIX machines. The dimuon triggers described above are among this “Stream A” set of events. The offline reconstruction is substantially more thorough than the level-3 reconstruction. It also computes higher-level quantities of interest to physicists (*e.g.*, track parameters, vertex positions, jet clusters, etc.) from the raw data using calibration constants derived in parallel from the data. It also includes proper alignment corrections for the tracking components of the detector.

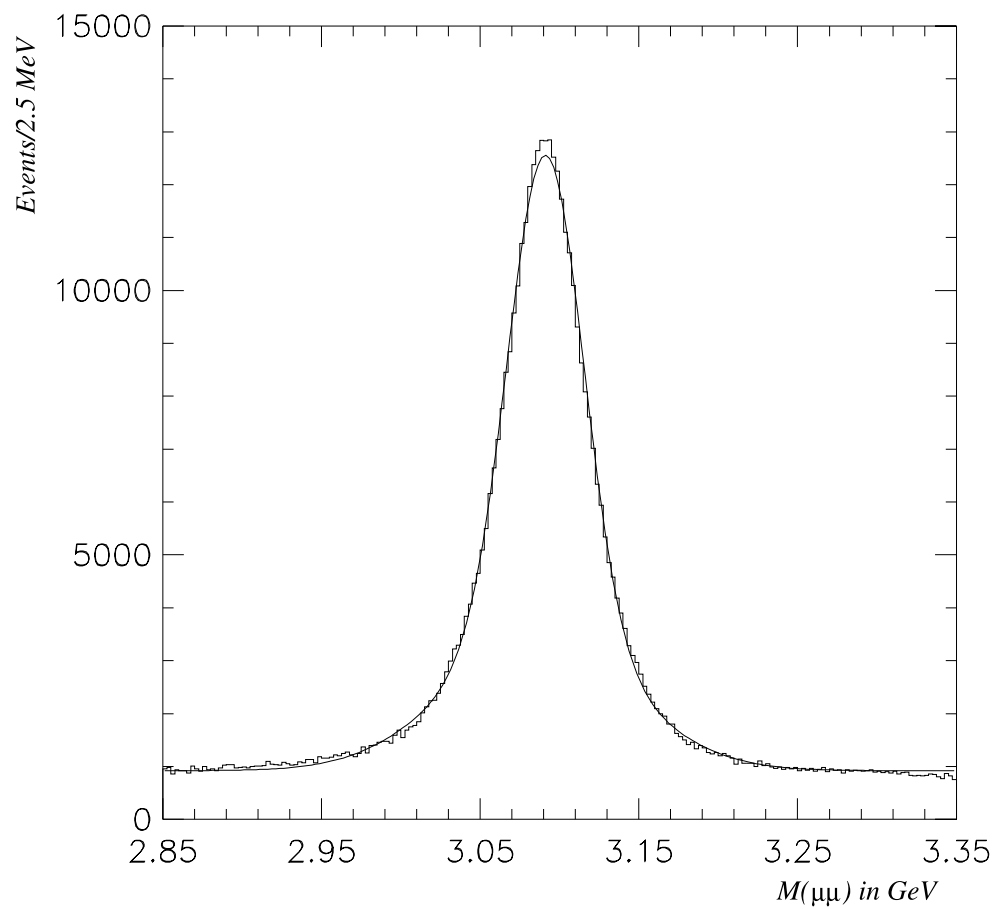


Figure 15: Dimuon Invariant mass of J/ψ candidates passing Level-3 muon trigger. A Gaussian fit to the peak plus a linear fit to the background gives 345800 ± 600 J/ψ events.

3.2.5 Inclusive J/ψ Data Set

Data that pass the dimuon triggers are collectively known as the inclusive J/ψ data set. This data set resides on disk and is used extensively as a source of events rich in B meson decays. Table 6 lists the specific triggers used in Runs Ia and Ib and the muon P_T cuts assigned to each. These cuts are designed to be above the 50% efficiency point of the trigger thresholds. In practice, higher P_T cuts will be imposed at a later stage of the analysis. As noted earlier, the production of B_c mesons at low P_T has large uncertainties associated with non-perturbative soft gluon exchange. To reduce theoretical and experimental uncertainties, the B_c branching ratio will be compared to a standard, well-studied branching ratio of the more conventional charged B ($B^+ \rightarrow J/\psi K^+$). Therefore, the same data set is chosen for consistency.

3.3 Simulation of Events by Monte Carlo

Simulated events are used to calculate the detection efficiencies of the various B meson decay channels examined in this analysis. The problem of sampling random processes, such as the production and decay of mesons containing heavy quarks, in a complex detector environment is made tractable by using computational sampling and integration methods known as “Monte Carlo” techniques. Following are descriptions of the various Monte Carlo packages employed in this analysis, and the necessary input parameters and assumptions.

3.3.1 Generation of b -quarks.

As described in Section 1.2.2, by convolving the gluon distribution functions with the parton-level cross section for producing $b\bar{b}$, one may calculate the dif-

| <i>Dimuon Trigger Name</i> | <i>Muon P_T Cuts</i> |
|----------------------------|-----------------------------------|
| CMU_CMU_ONE_CFT_1A | 2.8, 1.65 |
| CMU_CMX_ONE_CFT_1A | 2.8, 1.65 |
| CMU_CMU_TWO_CFT_1B | 1.9, 1.9 |
| CMU_CMX_TWO_CFT_1B | 1.9, 1.9 |
| CMX_CMX_TWO_CFT_1B | 1.9, 1.9 |
| CMUP_CMX_TWO_CFT_1B | 2.4, 1.9 |
| CMU_CMU_ONE_CFT_1B | 3.0, 1.65 |
| CMU_CMX_ONE_CFT_1B | 3.0, 1.65 |
| CMUP_CMU_ONE_CFT_1B | 3.0, 1.65 |
| CMUP_CMX_ONE_CFT_1B | 3.0, 1.65 |
| CMU_CMU_SIX_TOW_1B | 1.9, 1.9 |
| CMU_CMUX_ONE_CFT_1B | N.A. |
| CMUP_CMUX_ONE_CFT_1B | N.A. |

Table 6: List of triggers used in selecting J/ψ candidate events in Runs Ia and Ib, with associated muon P_T cuts. Trigger names reflect which muon chamber combinations are allowed (compound names such as CMUP are muons that leave hits in both the CMU and the CMP), how many level-2 CFT track matches were required, and the run for which each trigger was used. CMUX muons are not used, because there is no physical overlap between the CMU and the CMX.

ferential cross section for b -quark production $d\sigma(p\bar{p} \rightarrow b\bar{b})/dP_T dy$. Often, as is true here, one is only interested in the single-particle differential cross section. The final-state fragmentation fraction for a single b -quark to become a B_c is on the order of 10^{-3} times that for the other B mesons. Correspondingly, the probability for both the b and \bar{b} (anti-) quarks to fragment to $B_c^+ B_c^-$ is suppressed by roughly six orders of magnitude relative to $B^+ B^-$ production. Thus, we need only consider fragmentation, decay, and detector simulation of one of the two b -quarks produced in a given event. For this purpose, physicists at CDF have implemented the next-to-leading-order ($\mathcal{O}(\alpha_s^3)$) calculation of Nason, Dawson, and Ellis [40] for the single-particle inclusive differential cross section in a FORTRAN routine called **BGENERATOR**²¹. The result of this calculation depends on the choice of the parton distribution functions (PDF's) used, as well as the quark masses and the fragmentation scale parameter.

The input to this generator package is a two-dimensional histogram containing the cross section for producing a single b -quark as a function of transverse momentum P_T and rapidity y , including the correlation. Events are generated according to this histogram and subjected to user-defined cuts on both P_T and y . To avoid generating too many events at low P_T and y which would subsequently be removed by cuts later in the analysis, only events with $P_T(b) > 4.5$ GeV and $|y(b)| < 2.0$ were accepted. The default PDF and parameter values were chosen to be consistent with previous CDF B_c searches and with the discovery paper. The MRSD0 [45] structure functions were used, with $m_b = 4.75$ GeV, $m_c = 1.5$ GeV, and the default renormalization scale $\mu = \mu_0 \equiv \sqrt{m_b^2 + P_T^2(b)}$.

²¹There is an analogous calculation performed by Mangano, Nason, and Ridolfi [41] to calculate the full differential cross section for $b\bar{b}$ production.

3.3.2 Fragmentation into B_c

To the extent that both the B^+ and the B_c^+ are produced via the same mechanism and that kinematic cuts are chosen so that the data events lie in a region where non-perturbative effects can be neglected in producing the heavy quarks, the ratio of $\sigma \cdot \mathcal{B}$ of one B meson species to another is insensitive to the choice of PDF and fragmentation scale. However, the **BGENERATOR** treatment of B_c necessarily differs from the B^+ in fragmenting the b -quark to the final-state mesons. In order to establish a reasonable approach to quantifying the systematic uncertainty due to this essential difference, some understanding of the fragmentation mechanism and the definition of quark masses is required here.

After producing the $b\bar{b}$ pair, the quarks begin to separate (typically back-to-back) until the strong color field stores enough energy to create a new $q\bar{q}$ pair. For high- P_T quarks, this process can occur multiple times until one of the produced lighter quarks binds with the b -quarks into a hadron. This fragmentation process is not describable in perturbation theory and therefore can only be calculated in phenomenological models. This is, of course, one of the reasons for studying heavy quark systems such as the B_c — it provides insight into these non-perturbative models. A wide variety of functional forms have been proposed, but the Peterson [46] parameterization has become widely used due to its relative simplicity. This parameterization, as it was initially formulated, was defined for a system of a heavy quark Q and a light quark \bar{q} as a function of one kinematic variable z and one free parameter ϵ_P . The

variable z^{22} is defined as:

$$z = \frac{(E_m + p_m^{\parallel})}{E_Q + p_Q},$$

where the subscripts refer to the energy and momentum of the final-state meson or the heavy quark, and p_m^{\parallel} is the component of the meson momentum parallel to the heavy quark momentum. In physical terms, z roughly corresponds to the fraction of energy that the meson takes from the heavy quark. The functional form of the Peterson parameterization is:

$$\frac{dN}{dz} = \frac{1}{z[1 - (1/z) - \epsilon_P/(1 - z)]^2}.$$

This form has been used with some degree of success in modeling the cross sections for charm and bottom meson production at LEP. [47, 48] A compilation [49] of these results indicates that $\epsilon_c \simeq 0.06$ and $\epsilon_b \simeq 0.006$. The latter value is used in many B analyses at CDF. One may reasonably question whether this parameterization is applicable to the B_c , which contains two heavy quarks. According to Peterson, the parameter should roughly follow a simple scaling law: $\epsilon_Q \propto \frac{m_q^2}{m_Q^2}$. This analysis follows the precedent set by previous CDF B_c searches and the discovery paper in using an alternate fragmentation parameterization based on a perturbative calculation of gluon Bremsstrahlung off the b -quark, with the gluon splitting to $c\bar{c}$ and one of the c -quarks binding with the b . [50, 51] This is formulated as a function of z :

$$\begin{aligned} \frac{dN}{dz} = 6 & \quad -18(1 - 2R)z \\ & \quad + (21 - 74R + 68R^2)z^2 \\ & \quad - 2(1 - R)(6 - 19R + 18R^2)z^3 \\ & \quad + 3(1 - R)^2(1 - 2R + 2R^2)z^6, \end{aligned} \tag{3.1}$$

²²In a later section, a new quantity z will be defined. For clarity, the current z will be referred to as the ‘‘Peterson z .’’

where the single parameter $R = \frac{m_c}{m_c + m_b}$.

The fragmentation parameterization described in 3.1 is implemented in **BGENERATOR** and is used as the default for this analysis for historical compatibility. Figure 16 shows the parameterizations used in **BGENERATOR** and the variations in shape resulting from changes in the parameter values. Aside from the obvious question about whether one should place faith in a theoretical perturbative calculation of what is generally perceived to be a non-perturbative hadronization process, this formulation carries an explicit dependence on the quark masses. This introduces a systematic uncertainty into the B_c production cross section through the uncertainties on m_c and m_b . The framework of heavy quark effective theory (HQET) [52, 53, 54] allows one to define a heavy quark mass that is consistent even when non-perturbative effects are included (unlike the pole mass definition). The HQET mass definition introduces an additional parameter, $\bar{\Lambda}$, which must be estimated using other means (*e.g.*, QCD sum rules). According to the PDG, [7, p. 378] the HQET mass values derived in this way are $m_b = 4.74 \pm 0.14$ GeV and $m_c = 1.4 \pm 0.2$ GeV, for $\bar{\Lambda} = 0.57 \pm 0.07$ GeV. [55] Assuming uncorrelated errors, the most significant parametric dependence of R will be on m_c due to its larger fractional uncertainty and the appearance of m_c in the numerator.²³ To estimate the systematic error due to the parameter in the fragmentation function, m_c was varied by one standard deviation in the default **BGENERATOR** B_c fragmentation function. The Peterson parameterization was also used, with a value of $\epsilon_{B_c} = (m_c/m_b)^2 = 0.09$ to test the systematic dependence on the form of the fragmentation function.

²³The error term in m_b is suppressed by an additional factor of the b -quark mass.

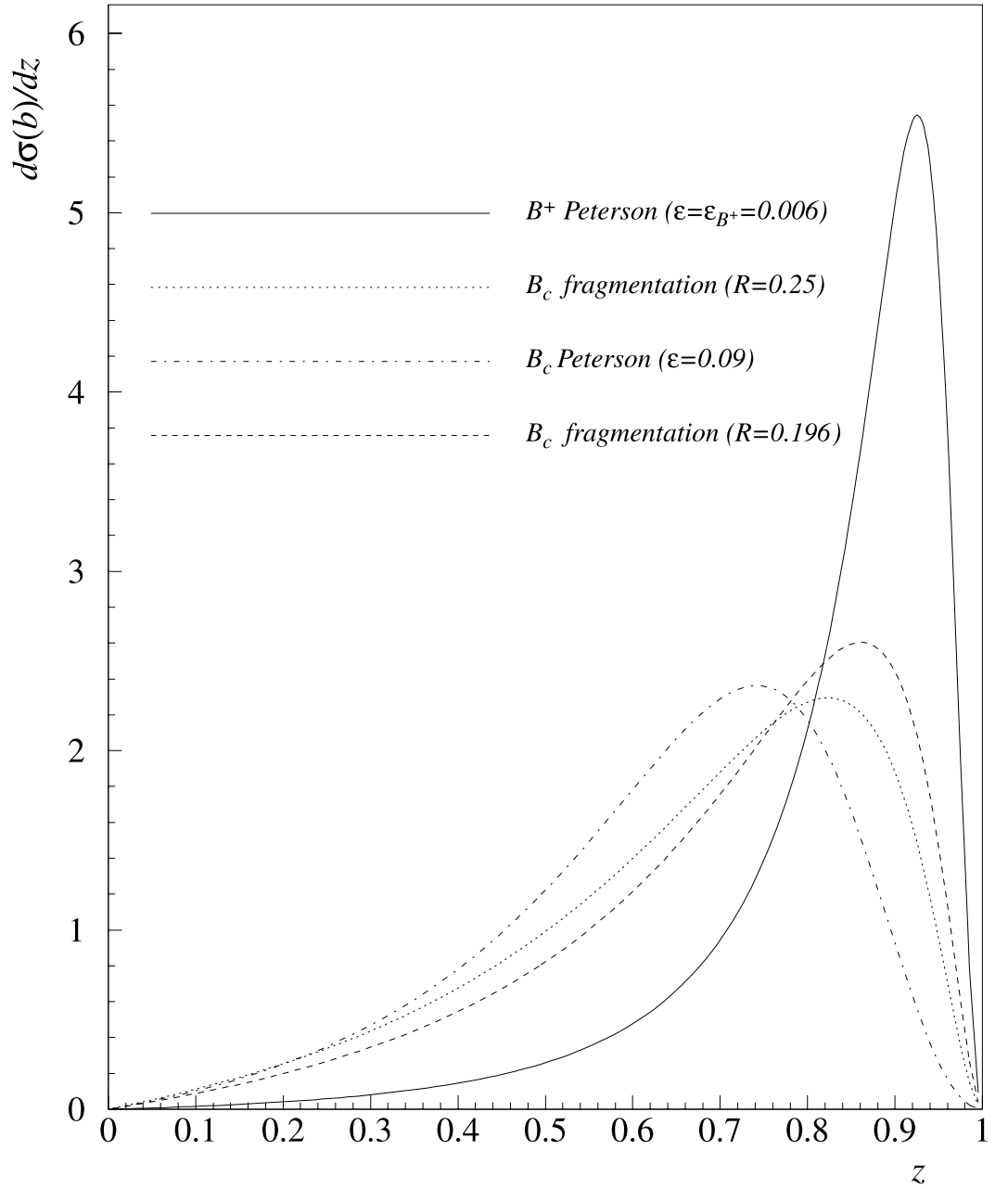


Figure 16: Parameterization of fragmentation functions as function of the kinematic variable z . Shown are the Peterson form for B^+ , the default B_c function with $R = \frac{1.5 \text{ GeV}}{1.5+4.5 \text{ GeV}} = 0.25$, the Peterson form for B_c with $\epsilon = (\frac{m_c}{m_b})^2 = 0.09$, and the default B_c fragmentation function with $m_c = 1.1 \text{ GeV}$ ($R = 0.196$). The average values of these distributions are $\langle z \rangle = 0.83, 0.67, 0.64$, and 0.70 , respectively.

3.3.3 Simulation of Decay

After generating a B meson with a given mass and 4-momentum distributed according to the PDF, the **CLEOMC** Monte Carlo package [56] is used to decay the meson to its final-state. The input to the **CLEOMC** module is a table of particle properties, including mass, lifetime, spin, and branching fractions into allowed final-states. For the purposes of this analysis, the default lifetime of 0.46 ps was used for the B_c , and 1.65 ps for B^+ decay. All decay modes except the relevant ones being studied ($B^+ \rightarrow J/\psi K^+$; $B_c^+ \rightarrow J/\psi \pi^+$; $B_c^+ \rightarrow J/\psi \pi^+ \pi^- \pi^+$) were turned off. Additionally, the J/ψ was required to decay via $J/\psi \rightarrow \mu^+ \mu^-$ 100% of the time. The Monte Carlo creates a displaced secondary vertex according to the input lifetime and handles the kinematics of the decay, including spin effects and phase space considerations, in determining the 4-momentum distributions of the final-state particles. Since the B , π , and K are all pseudoscalars and the J/ψ is a vector meson, the final-state J/ψ and π/K will be in a state with angular momentum $l = 1$, with the J/ψ spin transverse to its momentum vector in the B rest frame. This will affect the relative angular distributions of the final-state muons from $J/\psi \rightarrow \mu^+ \mu^-$. The 4-body final-state from $B_c^+ \rightarrow J/\psi \pi^+ \pi^- \pi^+$ is even more complex and would be difficult to analyze without the features of the **CLEOMC** module.

To determine systematic uncertainties due to the B_c lifetime, samples were also generated with $c\tau = 0.46_{-0.16}^{+0.18} \pm 0.03$ ps.

3.3.4 Detector Simulation

The final-state particles from **CLEOMC** are used as input to a simulation of the CDF detector known as **QFL**. [57] This simulation module uses parametric forms of the detector response to provide a fast calculation of acceptance

rather than performing a full physics simulation of all detector channels. To use a full physics simulation of the detector response would be prohibitively slow for studies of large-statistics samples. Inputs to **QFL** relevant to this analysis include alignment constants and resolution parameters appropriate to the specified run (Run IA/IB), beam size (transverse and longitudinal) for simulation of primary vertices, a database of detector channel efficiencies and dead elements, and SVX clustering parameters and thresholds. In addition, there is a covariance scaling parameter, which is taken to be 2.0 for Run Ib in accord with other CDF analyses. In calculating track parameters in the CTC, all elements of the covariance matrix are scaled by this amount to account for the fact that the hit resolutions alone do not account for the track parameter resolutions observed in test data. The source of this discrepancy remains unknown. The output of **QFL** is a set of banks containing high-level analysis quantities rather than simulated raw detector data banks. This obviates the need to perform a full-scale event reconstruction on simulated events. Although **QFL** provides the option to decay secondary particles (such as K and π), for the purposes of this analysis, these secondaries are treated as stable. Corrections for decay-in-flight of the secondaries are applied to the detection efficiencies in Section 5.5.

The dimuon trigger is modeled by a separate module called **DIMUTG**. [58, 59] This module uses a parameterization of the trigger turn-on to simulate acceptance. In addition to the efficiency plateau level, trigger turn-on momentum values, and background level parameters for each of the dimuon triggers, **DIMUTG** also includes effects due to dead towers and tower clustering.²⁴

Monte Carlo events are generated using the parameters of both Runs

²⁴Some triggers require a minimum separation between muon tower clusters at level-1.

Ia and Ib. All Monte Carlo samples used in this analysis are scaled according to the integrated luminosities of the Run Ia and Ib dimuon triggers so that each sample is composed of $\frac{20 \text{ pb}^{-1}}{(20+89) \text{ pb}^{-1}} = 18.3\%$ Run Ia simulated events and $\frac{89 \text{ pb}^{-1}}{(20+89) \text{ pb}^{-1}} = 81.7\%$ Run Ib simulated events.

Chapter 4

Analysis of the Data

4.1 Introduction

In order to identify those J/ψ mesons that result from the decay of either B_c or B^+ , additional tracks in the event are combined with the muons. One then removes track combinations which do not satisfy certain selection criteria designed to differentiate the signature of real B mesons from sources of background. This section describes the process necessary to extract a limit on hadronic B_c decays from the CDF Run I data.

4.2 Reconstruction of Vertices

One of the primary characteristics that distinguishes a J/ψ from B decay from other sources is that the B is long-lived and travels a measurable distance from its production vertex to its decay vertex. The primary vertex where the meson is produced is determined primarily by the SVX.²⁵ In any inelastic process that produces a heavy meson with enough transverse momentum to be found in the detector, there will also be a number of tracks from light, stable (or very long-lived) particles produced in association with the B that point back to the production vertex. The secondary (decay) vertex is also found by the SVX in the same manner: by reconstructing tracks that intersect near a common point, displaced from the primary vertex. Upon identification of a common

²⁵The beam positions used in this analysis are determined by averaging over individual runs, not on an event-by-event basis. During a collider run, the beam position exhibits long-term stability and the run-averaged position is less sensitive to measurement errors for each event.

decay vertex, measurement errors on quantities derived from the decay tracks can be reduced by a process known as “kinematic fitting.” The specialized software routine for performing such a kinematic fit on CDF data is called **CTVMFT**. [60] This routine applies user-specified constraints on the invariant mass of track combinations, pointing constraints that require combined track momenta to point back to a specified vertex, and a vertex constraint that forces the tracks to coincide at a secondary vertex. For example, in the decay $B^+ \rightarrow J/\psi K^+$, the two muons and the kaon can be simultaneously constrained to come from a decay vertex, the muons constrained to have the J/ψ invariant mass, and the combined momentum of the 3-track object (the B^+) constrained to point back to the primary vertex. The output would then be a new set of track parameters for each of the three tracks, with their new error matrices, the fitted primary and secondary vertices, and the χ^2 value of the fit. The details of how the track parameters and vertices are modified to satisfy the constraints is somewhat beyond the scope of this analysis, but I will point out a few relevant details.

The track parameters and vertices that result from the fit are chosen by satisfying the constraints with a minimum deviation (as determined by the χ^2 from the original measured parameters). The χ^2 for the fit is defined as:

$$\chi^2 = \sum_{i=1}^{N_{tracks}} \xi_i^T G_i^{-1} \xi_i, \quad (4.1)$$

where ξ_i is the vector of track parameter residuals (difference between constrained and unconstrained parameters) for track i , and G is the 5×5 covariance matrix of the original measured parameters. Assuming the covariance matrix faithfully reflects the uncertainties on the measured track parameters,²⁶ the χ^2 thus determined should behave according to an ordinary χ^2 distribution

²⁶This is approximately true when scaled appropriately. Scale factor used by various

for tracks satisfying the initial assumptions (*i.e.*, J/ψ and K from a real B). Background can then be reduced by removing events that have a low probability for originating from a χ^2 distribution.²⁷ A potential flaw in this scheme is that the CDF tracking system does not measure z_0 of tracks with very well known precision, and the z_0 resolution depends on the luminosity, due to multiple interactions. In order to reduce dependence on the z_0 measurements, one may only consider the χ^2 contribution from the three track parameters that are independent of z (curvature c , azimuthal angle ϕ_0 , and impact parameter d_0). Figure 17 shows the χ_{3d}^2 distribution and the probability that repeating the measurement with a different event would produce a larger χ_{3d}^2 for a sample of $B^+ \rightarrow J/\psi K^+$ events found in CDF data, which contains real B^+ mesons as well as background. In selecting these events, a cut on the fit $\chi^2 < 40$ is implemented in order to obtain a manageable sample. Without such a preselection, virtually every event in the dimuon trigger sample can be combined with at least one extra track to form a vertex. Such a large sample consisting almost entirely of background would make further analysis (specifically the cut optimization procedure, which is computation-intensive) infeasible. Of the channels considered in this analysis, the kinematic fit of $B_c^+ \rightarrow J/\psi \pi^+ \pi^- \pi^+$ has the highest number of degrees of freedom (10). The preselection on $\chi^2 < 40$ corresponds to a probability cut of $P(40|10) > 1.7 \times 10^{-5}$ on the $B_c^+ \rightarrow J/\psi \pi^+ \pi^- \pi^+$ events. Figure 18 is the same set of distributions for χ_{2d}^2 . If these values originate from a genuine χ^2 distribution, the probability profile will be flat. Cutting

authors is typically 1.5 - 2.5 for Run Ib; 2.0 is the value chosen for this analysis. The scale factor for Run Ia is taken to be 1.4.

²⁷The confidence level is determined by integrating the χ^2 distribution (with a given number of degrees of freedom) from 0 to the measured χ^2 and subtracting from 1. The interpretation of this “ χ^2 probability” is that it represents the probability that a random repeat of the experiment would observe a greater value of χ^2 , assuming the model is correct.

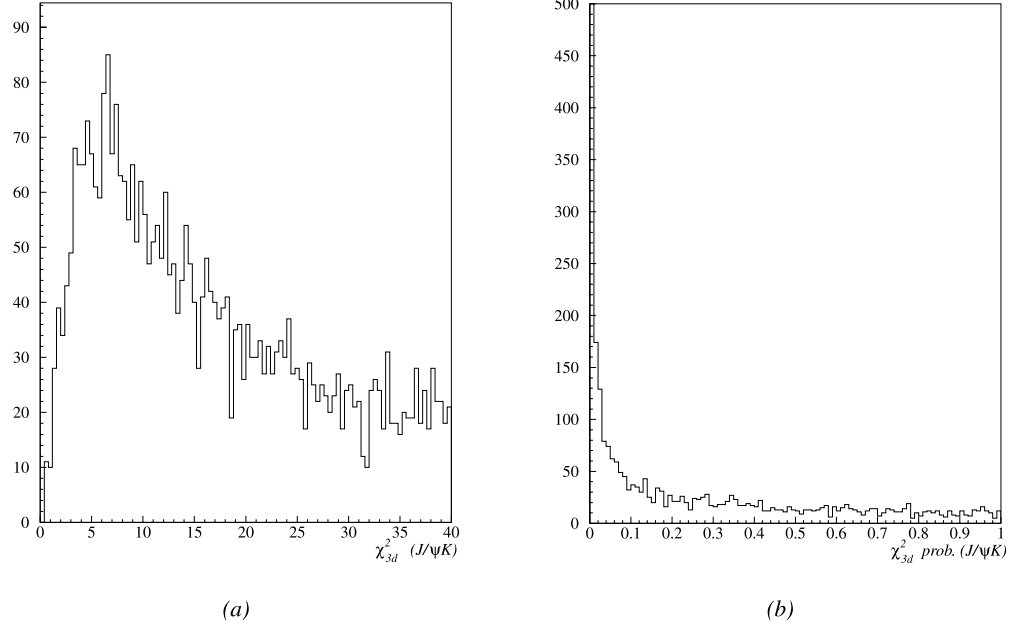


Figure 17: (a) χ^2_{3d} distribution for $B^+ \rightarrow J/\psi K^+$ candidate events found in the data, including background. The number of degrees of freedom for a kinematic fit to these events is 6. (b) χ^2 probability distribution for the same set of events. The first bin is cropped and extends to 2812 events.

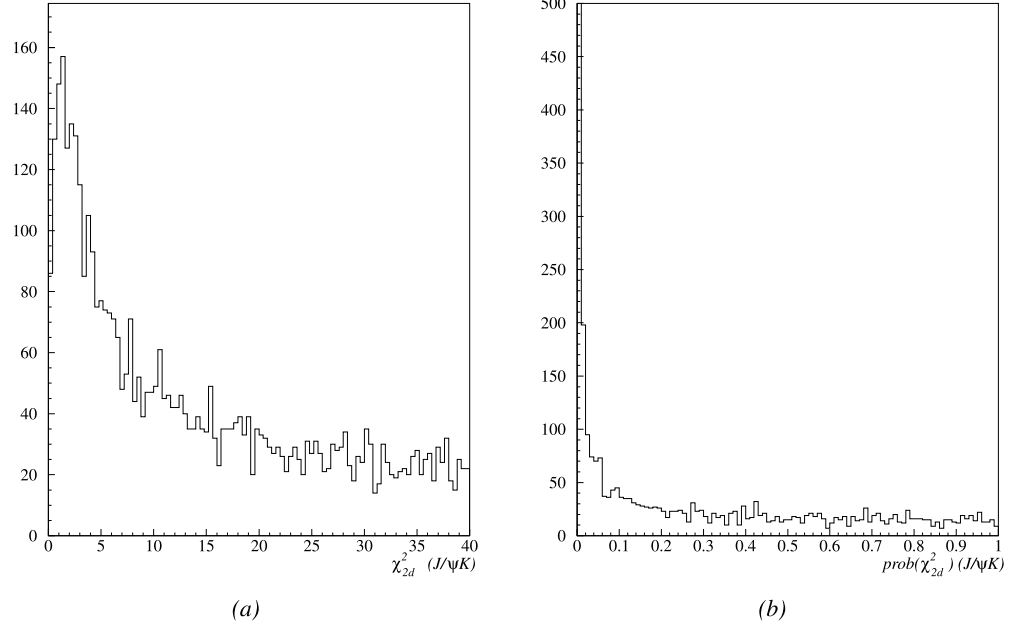


Figure 18: (a) χ^2_{2d} distribution for $B^+ \rightarrow J/\psi K^+$ candidate events found in the data, including background. The number of degrees of freedom for a kinematic fit to these events is 3. (b) χ^2 probability distribution for the same set of events. The first bin is cropped and extends to 2480 events.

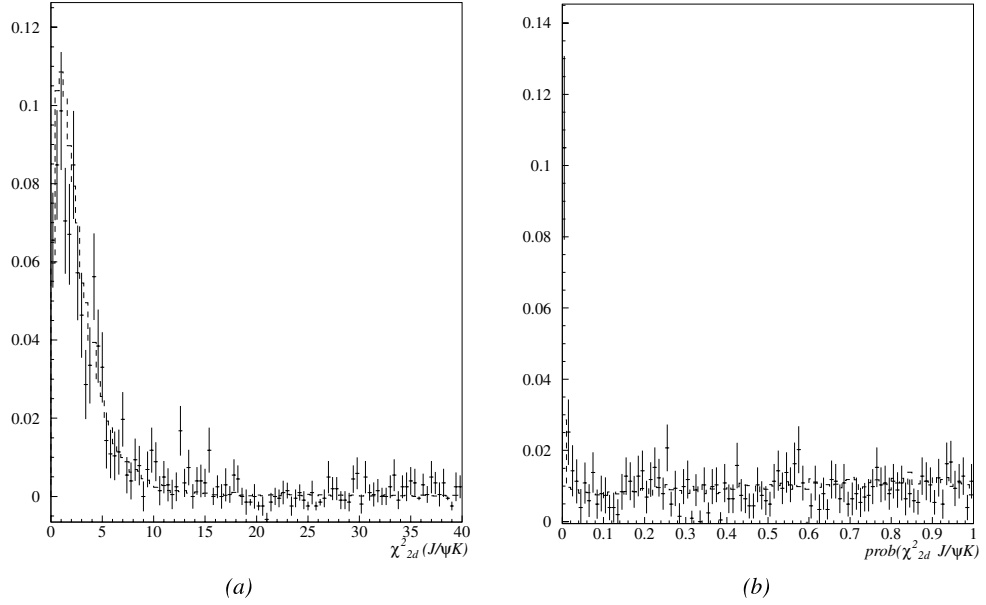


Figure 19: (a) Sideband-subtracted χ^2_{2d} distribution (with error bars) for $B^+ \rightarrow J/\psi K^+$ data events compared to the Monte Carlo (dashed). The number of degrees of freedom for a kinematic fit to these events is 3. (b) χ^2 probability distribution for the same set of events. Histograms are normalized to equal area for shape comparison.

on $prob(\chi^2|n_{dof}) > 1\%$ will then only eliminate 1% of the real events, while eliminating a much higher fraction of the background. The background events do not, in general, satisfy the constraints. The χ^2 from fits to a vertex containing tracks from combinatoric background will be larger than that of a B vertex. A fraction of the large peak at low probability also contains real B mesons with mismeasured track parameters and underestimated errors. By cutting on the 2-dimensional χ^2 , one hopes that the efficiency for retaining these latter type of events is improved by reducing the dependence on the z measurements.

The slope of the χ^2_{2d} probability distribution, which is more visible in the high-statistics Monte Carlo sample (compared to sideband-subtracted $B^+ \rightarrow J/\psi K^+$ data events) shown in Figure 19, merits further consideration. Omitting the peak at small probability, a linear fit to the Monte Carlo distribution gives a slope of $(26 \pm 9)\%$ per unit probability. The smaller statistics of the data are consistent, within errors, with zero slope. The χ^2_{2d} , as calculated above, does not strictly follow a true χ^2 distribution. The invariant mass constraint necessarily incorporates the z component of the track momenta (otherwise the constraint would apply to the transverse mass only). Thus, there will be a residual dependence of the transverse track parameters on the z_0 and the polar angle $\cot(\theta)$ measurements. The result is that, for those events where the opening angle between the muons occurs primarily in θ rather than in ϕ , the χ^2_{2d} per degree of freedom will be decreased relative to the corresponding χ^2_{3d} per degree of freedom. The probability distribution for 2-d χ^2 using a 3-d constraint behaves as a χ^2 with $n_{dof} = 3 - \epsilon$, where $\epsilon \approx 0.03$.²⁸ The χ^2_{3d} probability distribution in Figure 20 for the same Monte Carlo sample exhibits a zero slope, within statistical uncertainties, because the dimensionality of the constraints is commensurate with that of the track residuals.

4.3 Track Quality Cut

For proper reconstruction of the B decay vertices, the track parameters must be measured with high precision to reduce combinations of random tracks pro-

²⁸The χ^2 probability function can be generalized for non-integer values of the number of degrees of freedom using the incomplete gamma function: $P(\chi^2|\nu) = \frac{1}{\Gamma(\nu/2)} \int_{\chi^2/2}^{\infty} \exp^{-t} t^{\nu/2-1} dt$.

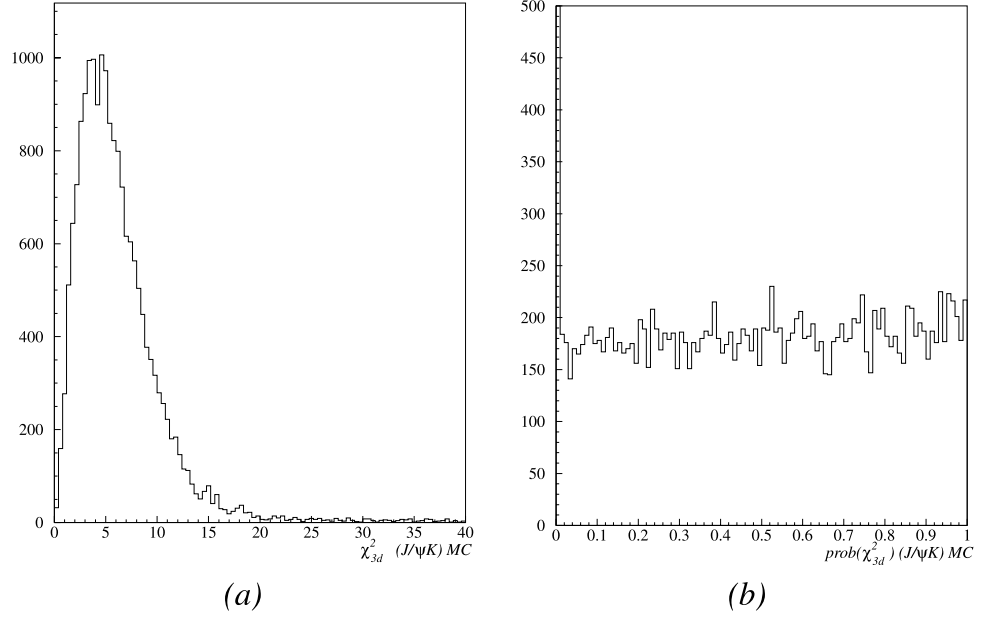


Figure 20: Figure (a) shows the χ^2_{3d} distribution for $B^+ \rightarrow J/\psi K^+$ events simulated by Monte Carlo. The number of degrees of freedom for a kinematic fit to these events is 6. Figure (b) is the χ^2 probability distribution for the same set of events.

duced in association with a prompt²⁹ J/ψ from producing a fake B . Figure 21 represents the displacement of decay vertices³⁰ of a sample of J/ψ events from CDF data as a function of the number of SVX hits required on each muon leg. All of these histograms show a contribution from prompt J/ψ and from combinatorial background. Both background components are symmetric in L_{xy} with clearly worsening resolution as the SVX requirements are loosened. Only the histogram for both legs with ≥ 3 SVX hits shows an identifiable positive-lifetime tail. Therefore, all tracks considered as decay products of a B will be required to have 3 or more hits in the SVX.

4.4 J/ψ Selection

In addition to the cuts on muon SVX hits and 2-dimensional χ^2 probability already considered, J/ψ events considered for further analysis are selected by requiring the reconstructed invariant mass (before constraints) to be within 50 MeV (3 standard deviations) of the PDG value: $|M(\mu^+\mu^-) - 3096.87| < 50$ MeV. [7, p. 46] At the average instantaneous luminosity during Run Ib, the number of reconstructed interaction vertices in each event is Poisson-distributed with a mean of ~ 2.5 . To avoid combining muons from different primary vertices, there is an additional cut requiring the z_0 measurements to lie within 5 cm of each other: $|z_0^{\mu_1} - z_0^{\mu_2}| < 5$ cm. Figure 22 shows the mass distribution of J/ψ candidates. There are 193051 ± 807 (*stat*) events from a

²⁹*i.e.*, not coming from a long-lived parent, but produced at the primary vertex

³⁰The measured displacement in the transverse plane is referred to at CDF as L_{xy} . This can be converted into a “proper lifetime” $c\tau$ by dividing by the velocity: $c\tau = L_{xy} \frac{M(B)}{P_T(B)}$. Both quantities are signed according to the dot product of the displacement and the momentum so that displaced vertices resulting from the decay of a particle have positive L_{xy} and $c\tau$.

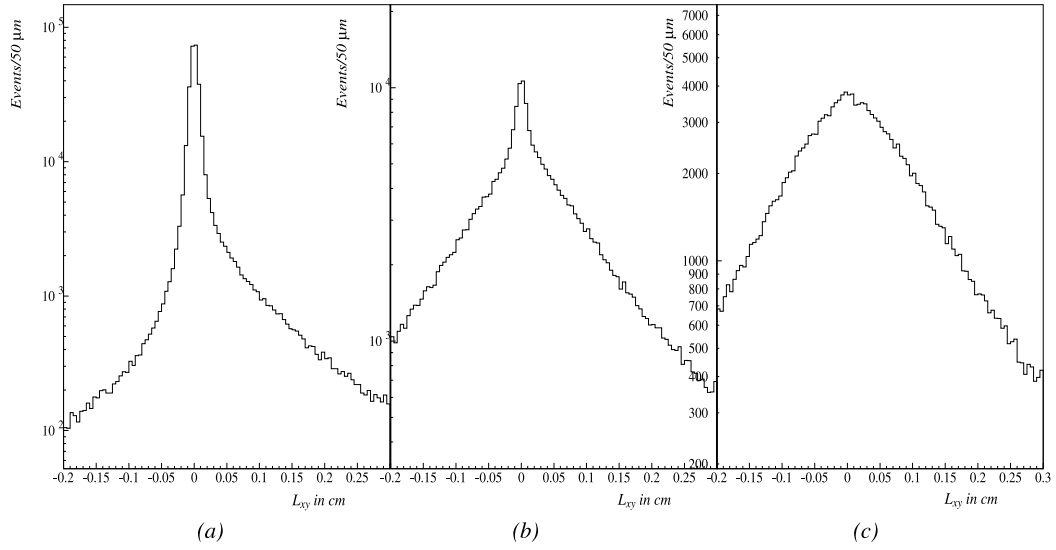


Figure 21: L_{xy} distributions for J/ψ events. (a) At least 3 SVX hits on each muon leg. (b) 3 or more SVX hits on one muon leg, with the other leg having < 3 SVX hits. (c) Fewer than 3 SVX hits on both muon legs. Note distributions are plotted on a logarithmic scale, so positive lifetime component visible in (a) has a linearly decreasing L_{xy} profile.

fit to the peak. The mass resolution is determined by a fit to the peak and gives $\sigma_M(J/\psi) = 16$ MeV. The contribution of background to the peak region ($\pm 3\sigma$) is found from a fit to the sidebands to be 12%.

4.5 Selection of B^+ and B_c mesons

After preselecting a sample of J/ψ events that pass the desired selection criteria, additional tracks are combined with the J/ψ to form B meson candidates. For the three-track vertices ($B_c^+ \rightarrow J/\psi\pi^+$ and $B^+ \rightarrow J/\psi K^+$), individual tracks in each event that pass the SVX quality cut and a minimal P_T cut ($P_T > 1$ GeV)³¹ are combined one at a time with the J/ψ via a kinematic fit with the following constraints: the two muons are fixed to the J/ψ mass, all three tracks are forced to come from the same secondary vertex, and the combined P_T^B vector must point back to the primary vertex. Of those combinations that pass the χ^2 probability cut, the combination with the best χ_{2d}^2 is selected. Multiple B mesons in a single event would be exceedingly rare (by a factor of $\sim 10^{-3}$ relative to single B production), and are not considered. At this stage, the principal source of background will be unassociated tracks that pass close to a J/ψ vertex in the transverse plane and fake the B decay signature.

In the $B_c^+ \rightarrow J/\psi\pi^+\pi^-\pi^+$ case, all combinations of three tracks that pass the SVX and $P_T > 1$ GeV cuts are considered. The kinematic fit requires both muons and all three added tracks to come from the same secondary vertex, with the combined P_T vector pointing back to the primary, and the

³¹The momentum distribution of unassociated tracks is sharply peaked at 0 and falls off rapidly. Secondary particles from B decay are expected to carry a significant fraction of the B P_T . We shall later require a more stringent cut on the track momentum for the final event selection.

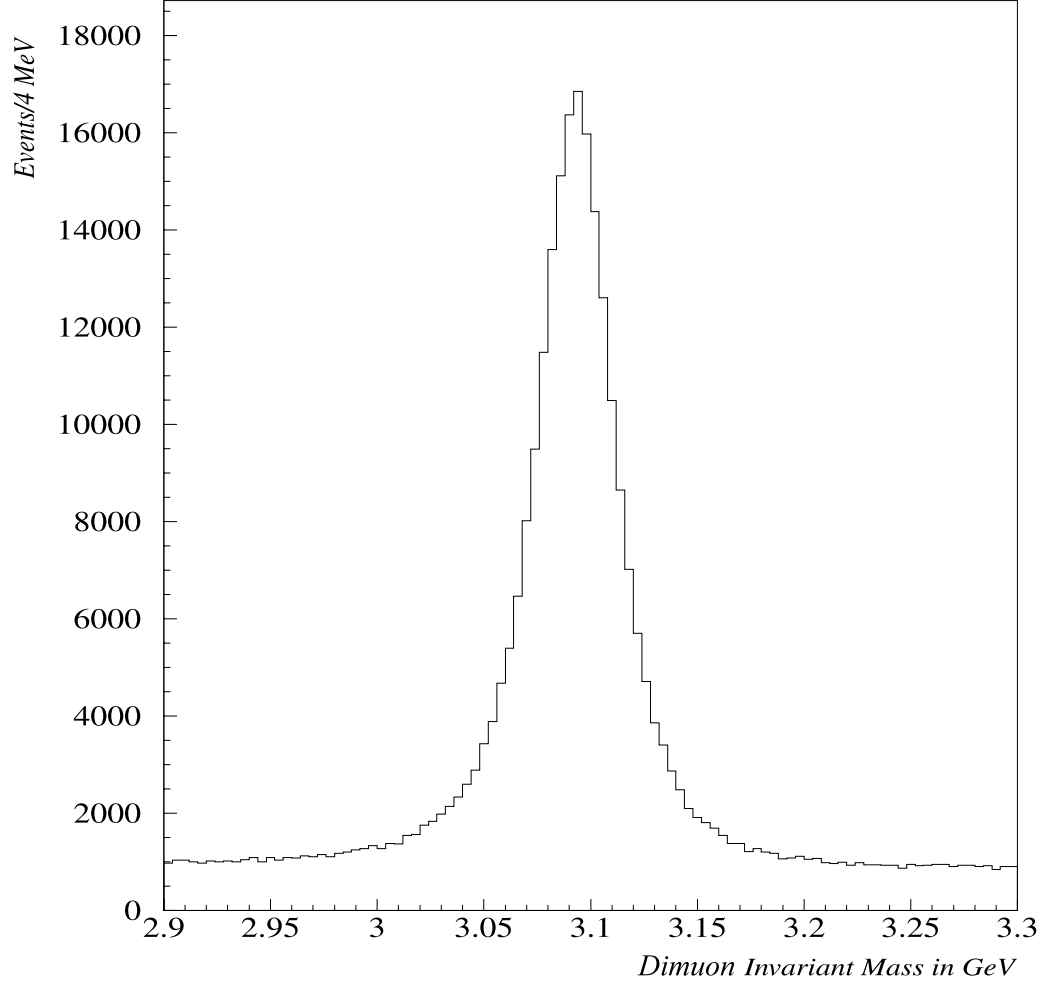


Figure 22: Invariant mass distribution of J/ψ events. A simultaneous fit to the peak and sideband regions indicates 193051 ± 807 events in the peak (taken to be $\pm 3 \sigma$), with a background contribution of 12%.

J/ψ mass constraint as above. The combination in each event with the best χ^2_{2d} that passes the probability cut is chosen for further analysis.

4.5.1 Optimization of Final Event Selection

In order to select events with a minimum of experimenter bias, it is useful to first outline the analysis procedure before examining the data. This eliminates the possibility of selecting cuts designed to specifically emphasize a peak in a given spectrum.

The optimization of cuts for the final event selection proceeds as follows:

- (1) Identify a set of kinematic and geometric quantities that can be used to discriminate data from background sources.
- (2) Choose statistical quantities to maximize or minimize for a given selection of cuts.
- (3) Use a large sideband region in the mass distribution to estimate background contribution.
- (4) Use the measured $\sigma \cdot \mathcal{B}$ ratio from the $B_c \rightarrow J/\psi \mu \nu$ analysis to estimate expected signal size of $B_c^+ \rightarrow J/\psi \pi^+$.
- (5) Generate B_c Monte Carlo events with a nominal mass of 6.2 GeV and lifetime from trilepton analysis, $\tau = 0.46$ ps. Normalize Monte Carlo events to the signal size predicted from step 4.
- (6) Iterate over all combinations of cuts to find the optimum set for the figure of merit from step 2.
- (7) Apply selected optimum set of cuts to J/ψ events.

4.5.2 Choice of Cut Variables

To determine the kinematic quantities to be considered as cut variables, one can appeal to those physical properties that distinguish a real B signal from background. The long lifetime of B^+ and B_c mesons suggest that the lifetime, $c\tau$, would be an obvious discriminating variable.³² Figure 23 shows the $c\tau$ distribution for $B_c^+ \rightarrow J/\psi\pi^+$ candidate events from the data and for Monte Carlo events generated with the nominal B_c lifetime 0.46 ps and with the variation between the $\pm 1\sigma$ ($-0.16, +0.18$ ps) uncertainties. Because no cuts other than the basic track quality and goodness-of-fit have yet been applied, the data sample is expected to be dominated by background. For this minimal choice of cuts, the Monte Carlo lifetime distributions are almost entirely uncorrelated with the choice of fragmentation functions.

The momentum spectrum of secondaries from heavy particles is significantly harder than that of random tracks not associated with the B . This difference can be observed in Figure 24, which compares the distribution of pion P_T (P_T^π) in the tentatively-identified $B_c^+ \rightarrow J/\psi\pi^+$ data sample to that of the Monte Carlo. The Monte Carlo P_T^π spectra peak near 1.5 GeV while the data, which consists almost exclusively of background, displays a rapid monotonic decline from $P_T^\pi = 0$. The effects of the lifetime variation and choice of fragmentation function on the Monte Carlo sample are compared in this plot as

³²Strictly speaking, the mean lifetime is a fixed, measurable quantity intrinsic to each particle species. The actual decay distance of an individual particle is treated here as a variable quantity, distributed according to an exponential decay, with the decay constant fixed to the species lifetime. When used as a selection criterion, the quantity $c\tau$ hereafter refers to the kinematic variable corresponding to the transverse decay length (the “proper lifetime”), not the species lifetime.

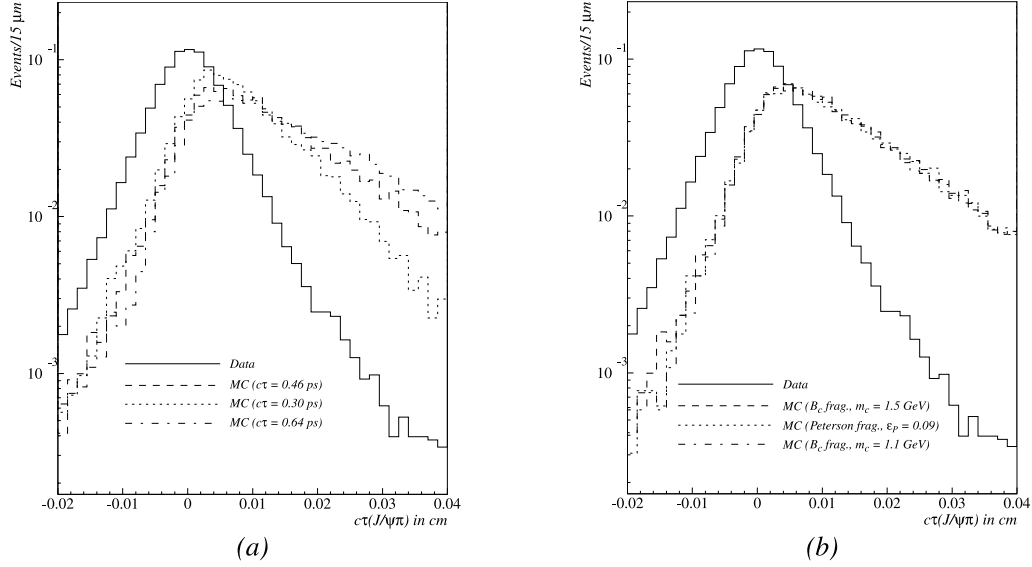


Figure 23: Distribution of $c\tau$ for $B_c^+ \rightarrow J/\psi\pi^+$ candidate events. (a) Solid histogram is $c\tau$ for $B_c^+ \rightarrow J/\psi\pi^+$ candidate events that pass only track quality and χ^2 cuts. Dashed and dotted histograms are Monte Carlo generated $B_c^+ \rightarrow J/\psi\pi^+$ events with the nominal lifetime, and ± 1 standard deviation in $c\tau$ that pass the same set of cuts. (b) Solid is the same $c\tau$ histogram from $B_c^+ \rightarrow J/\psi\pi^+$ data events. Dashed and dotted histograms show variation of Monte Carlo with choice of fragmentation function. All histograms are normalized to the same area and plotted on a logarithmic vertical scale for shape comparison.

well. The pion momentum is independent of the lifetime assumption and the fragmentation parameterization within the Monte Carlo statistics used here.

Likewise, the transverse momentum of the B itself, P_T^B , should be distributed over a broader momentum range than tracks combined with prompt J/ψ 's.³³ Figure 25 illustrates the utility of this cut variable by comparing the $B_c^+ \rightarrow J/\psi \pi^+$ sample to the Monte Carlo P_T^B distributions. The small variation of the Monte Carlo samples indicates that with this minimal cut selection, P_T^B has negligible correlation with either the assumed B_c lifetime or the choice of fragmentation function.

An additional possibility for removing random track combinations from the sample can be deduced from the geometry of these events. Particles that are not the result of a long-lived B decay will generally originate from either direct production at the primary vertex or from the strong or electromagnetic decay of a very short-lived particle produced at the primary vertex. The reconstructed tracks of these particles, therefore, will have a small impact parameter with respect to the primary vertex. Secondaries from B decay are produced at the secondary vertex and can not typically be extrapolated back to the primary vertex; these tracks will have a much broader distribution in d_0 . Figure 26 illustrates the distribution of the impact parameter from these sources. This reasoning suggests that a cut on the impact parameter significance, $\frac{d_0}{\sigma(d_0)}$, might be an effective tool for reducing background. The

³³The P_T^B cut may not be efficient for removing combinations of unassociated tracks and a J/ψ that does come from B decay, due to the significant momentum contribution from the J/ψ itself. Such events will not produce a peak in the $M(B)$ spectrum, however. In any case, it is hoped that the choice of the best χ^2 combination will reduce such a source of background.

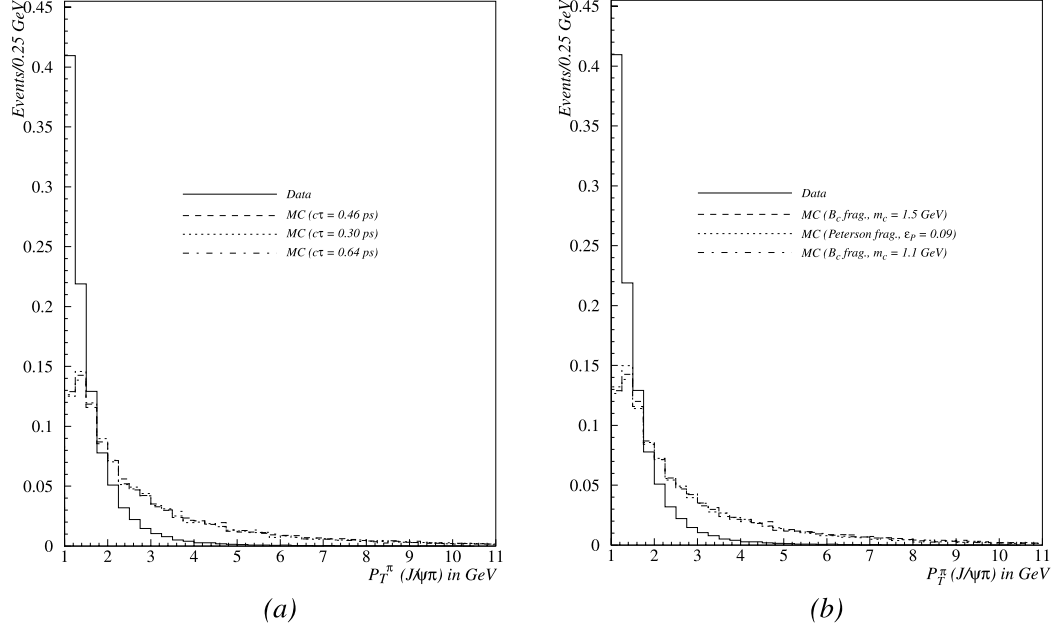


Figure 24: Distribution of P_T^π for $B_c^+ \rightarrow J/\psi \pi^+$ candidate events. (a) Solid histogram is P_T^π for $B_c^+ \rightarrow J/\psi \pi^+$ candidate events that pass only track quality and χ^2 cuts. Dashed and dotted histograms are Monte Carlo generated $B_c^+ \rightarrow J/\psi \pi^+$ events with the nominal lifetime, and ± 1 standard deviation in $c\tau$ that pass the same set of cuts. (b) Solid is same P_T^π histogram from $B_c^+ \rightarrow J/\psi \pi^+$ data events. Dashed and dotted histograms show variation of Monte Carlo with choice of fragmentation function. All histograms are normalized to the same area for comparison of shape.

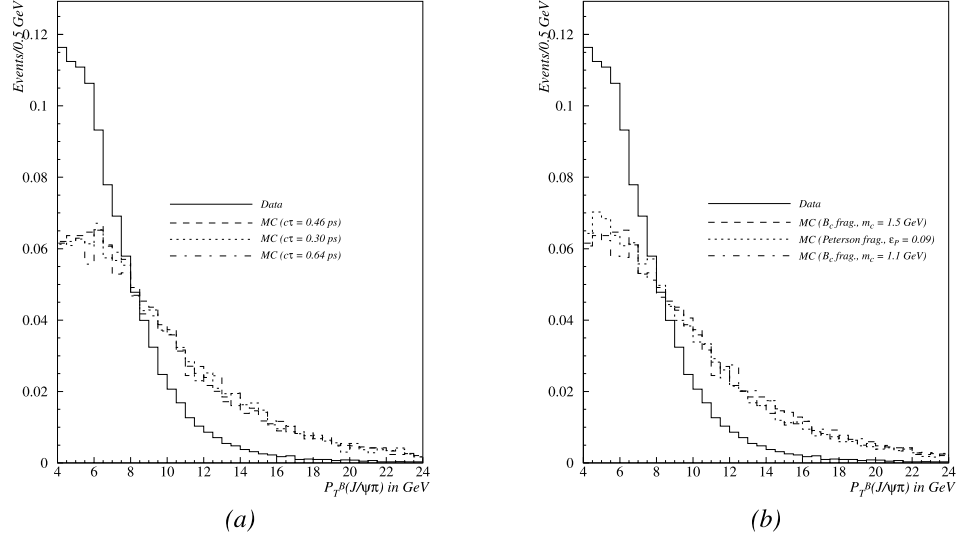


Figure 25: Distribution of P_T^B for $B_c^+ \rightarrow J/\psi \pi^+$ candidate events. (a) Solid histogram is P_T^B for $B_c^+ \rightarrow J/\psi \pi^+$ candidate events that pass only track quality and χ^2 cuts. Dashed and dotted histograms are Monte Carlo generated $B_c^+ \rightarrow J/\psi \pi^+$ events with the nominal lifetime, and ± 1 standard deviation in $c\tau$ that pass the same set of cuts. (b) Solid is same P_T^B histogram from $B_c^+ \rightarrow J/\psi \pi^+$ data events. Dashed and dotted histograms show variation of Monte Carlo with choice of fragmentation function. All histograms are normalized to the same area for comparison of shape.

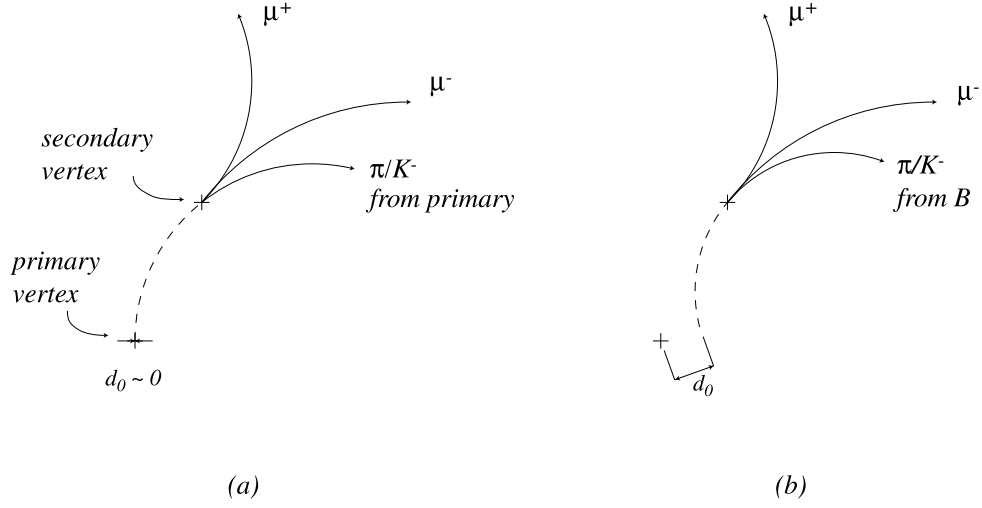


Figure 26: Illustration of impact parameter for (a) prompt tracks and (b) tracks from B decay. For prompt tracks that pass near a displaced secondary vertex formed by a J/ψ , the reconstructed d_0 will be small. For tracks that come from B decay, extrapolation back to the primary vertex results in a d_0 significantly different from zero.

efficacy of such a cut is somewhat diluted by the kinematic fit,³⁴ and also by the requirement of large track momentum.³⁵ Figure 27 shows the distributions of the impact parameter significance for the $B_c^+ \rightarrow J/\psi\pi^+$ data sample and Monte Carlo with $c\tau$ and fragmentation function variations. For smaller B_c lifetime, the secondary vertex lies closer to the primary, and the reconstructed d_0 is smaller (the distribution is more sharply peaked at 0), making the impact

³⁴The vertex constraint can pull random tracks into the secondary vertex and therefore broaden d_0 , although at the expense of a larger χ^2 .

³⁵In the limit of large momentum, this track will carry most of the B P_T , and will point back to the primary vertex; its small curvature ($1/P_T$) will then give a small d_0 .

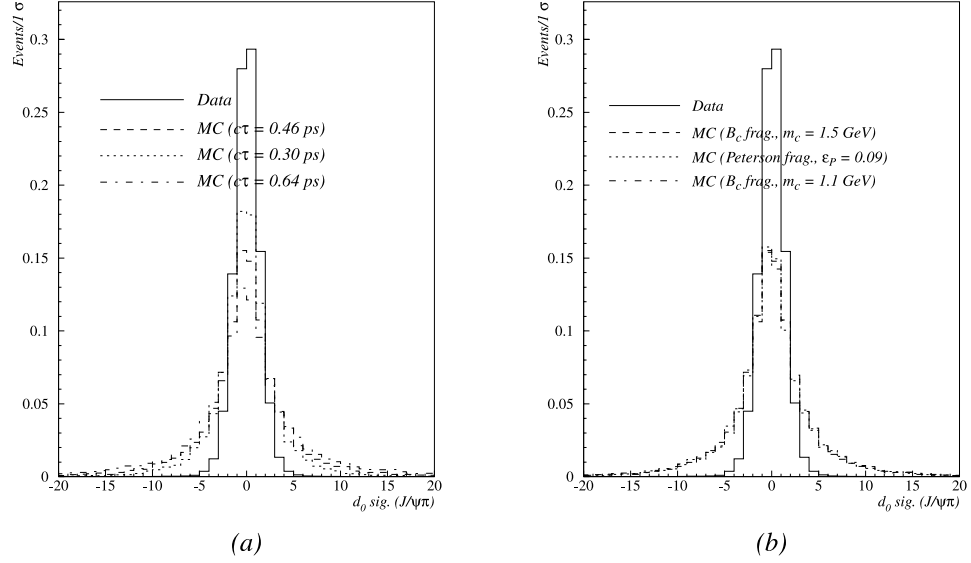


Figure 27: Distribution of pion impact parameter for $B_c^+ \rightarrow J/\psi\pi^+$ candidate events. (a) Solid histogram is pion impact parameter significance for $B_c^+ \rightarrow J/\psi\pi^+$ candidate events that pass only track quality and χ^2 cuts. Dashed and dotted histograms are Monte Carlo generated $B_c^+ \rightarrow J/\psi\pi^+$ events with the nominal lifetime, and ± 1 standard deviation in $c\tau$ that pass the same set of cuts. (b) Solid is the same histogram of impact parameter significance from $B_c^+ \rightarrow J/\psi\pi^+$ data events. Dashed and dotted histograms show the variation of Monte Carlo events with the choice of fragmentation function. All histograms are normalized to the same area for comparison of shape.

parameter significance cut somewhat less effective. No discernible correlation with the fragmentation functions is observed with this minimal set of cuts.

4.5.3 Choice of Statistical Measures

The next step in the optimization procedure is to determine a statistical quantity to serve as a measure of the desirability of a particular set of cuts. For $B^+ \rightarrow J/\psi K^+$ there is a known and well-studied excess of signal events over background, and one may unambiguously choose to maximize the signal significance, $\sqrt{\frac{S^2}{S+B}}$ to determine the “best” set of cuts. The background estimate, B, is determined by choosing a sideband region of fixed width in the $J/\psi K^+$ invariant mass distribution and interpolating into the mass peak region.³⁶ The distribution away from any real particle or resonance is expected to be approximately flat (or monotonically decreasing according to some fit function, here taken to be linear). The signal size, S, can be obtained from a Gaussian fit to the peak region.

For the $B_c^+ \rightarrow J/\psi \pi^+$ channel, we expect a small signal ($\sim 10^{-3} \times N_{B^+}$) and a background level of comparable size. It is not known in advance whether the signal is statistically significant or not. For small signal searches, the mean value theorem no longer holds³⁷ for the signal size, and the background becomes the dominant term in the uncertainty. Therefore, $\sqrt{\frac{S^2}{B}}$ is a more rational choice for the signal significance. In fact, the number of background events may be so small that it no longer satisfies the mean value theorem either,

³⁶The peak region for $B^+ \rightarrow J/\psi K^+$ is defined as $|M_{fit} - 5.2789 \text{ GeV}| < 50 \text{ MeV}$, corresponding to ± 3 standard deviations. The sidebands are defined as $200 \text{ MeV} < |M_{fit} - 5.2789 \text{ GeV}| < 400 \text{ MeV}$.

³⁷The number of events corresponds more closely to Poisson, rather than Gaussian, statistics. Hence the uncertainty is not proportional to \sqrt{N} .

making a generalized form of $\sqrt{\frac{S^2}{S+B}}$ that allows for a background contribution distributed according to Poisson statistics desirable. One way to accomplish this is by relating the cumulative Poisson probability to the cumulative Gaussian to obtain a quantity that represents how many “standard deviations” a particular Poisson-distributed signal lies above the measured background. Thus, if μ_B is the mean background determined from a fit to the sideband regions and n_S is the number of signal events in a predefined peak region, the equation:

$$\frac{1}{\Gamma(\mu_B + 2n_S + 1)} \int_{n=\mu_B}^{\infty} \exp^{-n} n^{\mu_B+2n_S} dn = \int_{x=-\infty}^{x_S} \frac{1}{\sqrt{2\pi}} \exp^{-\frac{x^2}{2}} dx, \quad (4.2)$$

is solved for x_S , which is the equivalent number of standard deviations away from the Poisson mean $\mu_B + n_S$ that the signal lies. Note that if for a particular measurement the “signal” fluctuates below the background level, x_S may take on a negative value. In the limit $\lim_{\mu_B \rightarrow \infty}$, $x_S = \frac{n_S}{\sqrt{n_S + \mu_B}}$ the identification with the $\sqrt{\frac{S^2}{S+B}}$ statistic becomes exact.

4.5.4 Optimized Selection of $B^+ \rightarrow J/\psi K^+$ Events

As an initial test of the cut optimization procedure, a final sample of $B^+ \rightarrow J/\psi K^+$ events is obtained and is used as a normalization in the measurement of the B_c branching fractions. Due to the large signal size and high purity of the $B^+ \rightarrow J/\psi K^+$ sample, an impact parameter cut is not used in selecting these events. However, this cut is considered for the B_c selection where reducing the background is of primary importance. To select the optimal set of cuts for the $B^+ \rightarrow J/\psi K^+$ events, I choose a range of acceptable cut values for P_T^B (5 to 15 GeV), P_T^K (1 to 6 GeV) and $c\tau$ (0 to 200 μm)³⁸ and subdivide each range

³⁸The choice of a lower limit on P_T^B of 5 GeV is made to avoid the region of non-factorizable fragmentation at low P_T . If P_T^B is allowed to be less than the order of the b -quark mass,

into ten equally spaced cut values. For each of these 10^3 combinations of cuts, the signal significance, $\sqrt{\frac{S^2}{S+B}}$, is calculated using a Gaussian fit to the B^+ mass peak for S , and a linear fit to the sideband regions for B . The set of cuts that maximizes this quantity determines the final selection of $B^+ \rightarrow J/\psi K^+$ events. This procedure would clearly be biased if the intent were to discover the B^+ or to measure its cross section. Since the $B^+ \rightarrow J/\psi K^+$ events are used only as a normalization for the B_c decay channels, optimization of the $B^+ \rightarrow J/\psi K^+$ signal does not introduce a bias to the B_c search. Figures 28, 29, and 30 represent slices through this 3-dimensional space of cut variables. The height of the bins in these figures corresponds to the value of $\sqrt{\frac{S^2}{S+B}}$ for a given set of cuts. The x - and y -axes are two of the kinematic cut values (with the third cut held to an indicated constant value). There are, of course, $3 \times 10^1 = 30$ such plots one could make to give a complete depiction of the correlations between these three cut variables. The three plots shown correspond to the three orthogonal slices through the optimal set of cuts.

The main objective in examining these plots is to ensure that the optimization procedure outlined above does not give rise to any pathological behavior before it is applied to the $B_c^+ \rightarrow J/\psi \pi^+$ channel. In a sample containing a statistically significant signal such as $B^+ \rightarrow J/\psi K^+$, the variation in the optimized quantity ($\sqrt{\frac{S^2}{S+B}}$) should be a smooth function of the cut variables. It should not be subject to large statistical fluctuations. By examining the shape of these 2-dimensional histograms, it is clear that the signal significance is indeed a well-behaved function of the cut variables. The optimal

the fragmentation function used in the Monte Carlo becomes invalid and the efficiency calculation is rendered meaningless.

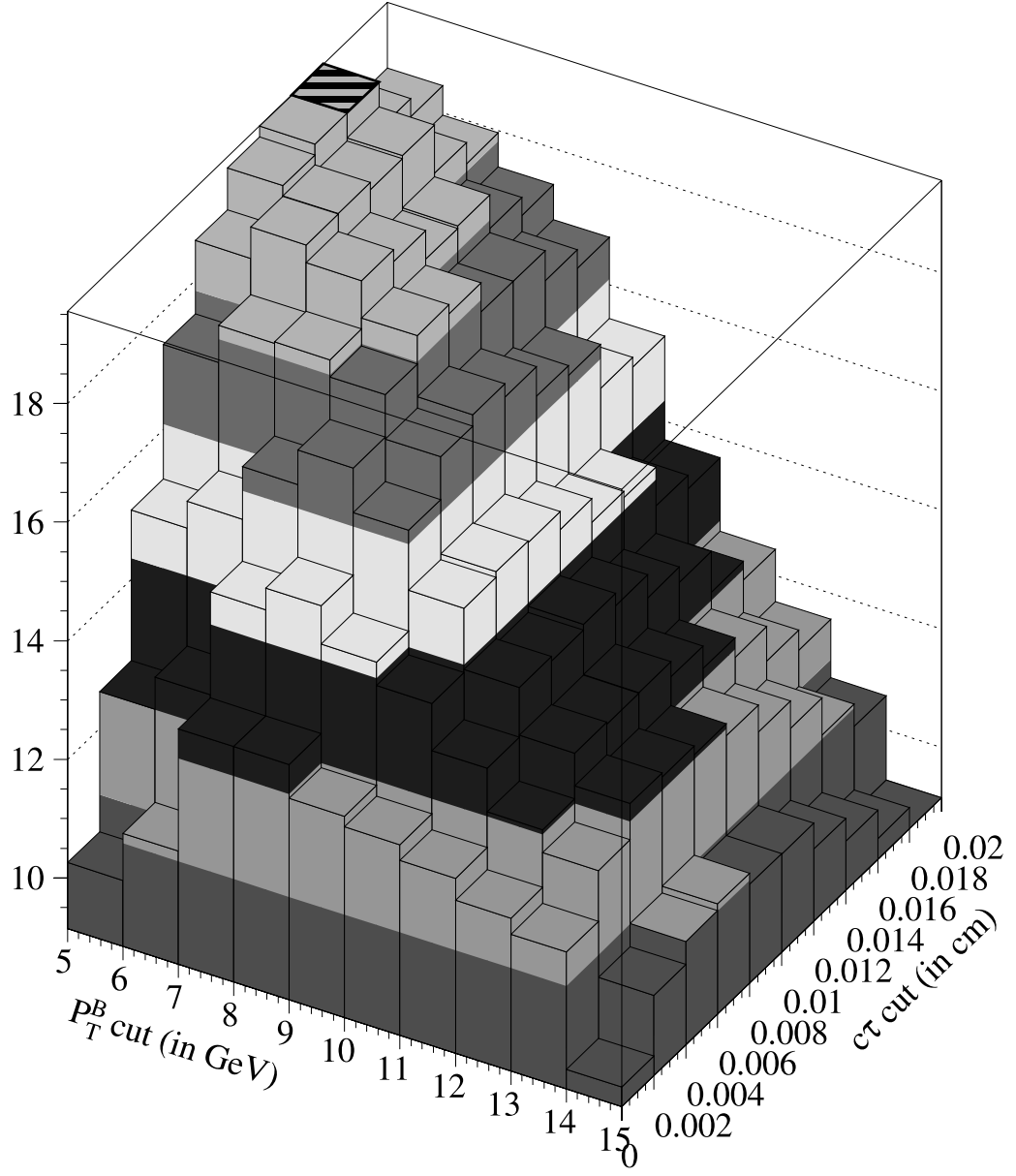


Figure 28: Signal significance $\sqrt{\frac{S^2}{S+B}}$ for $B^+ \rightarrow J/\psi K^+$ events as a function of P_T^B and $c\tau$ cuts. Hatched bin corresponds to optimized set of cuts. Shaded bands represent ~ 2 standard deviation variations in $\sqrt{\frac{S^2}{S+B}}$. In this plot, P_T^K is held constant at the optimized value: $P_T^K > 1.5$ GeV.

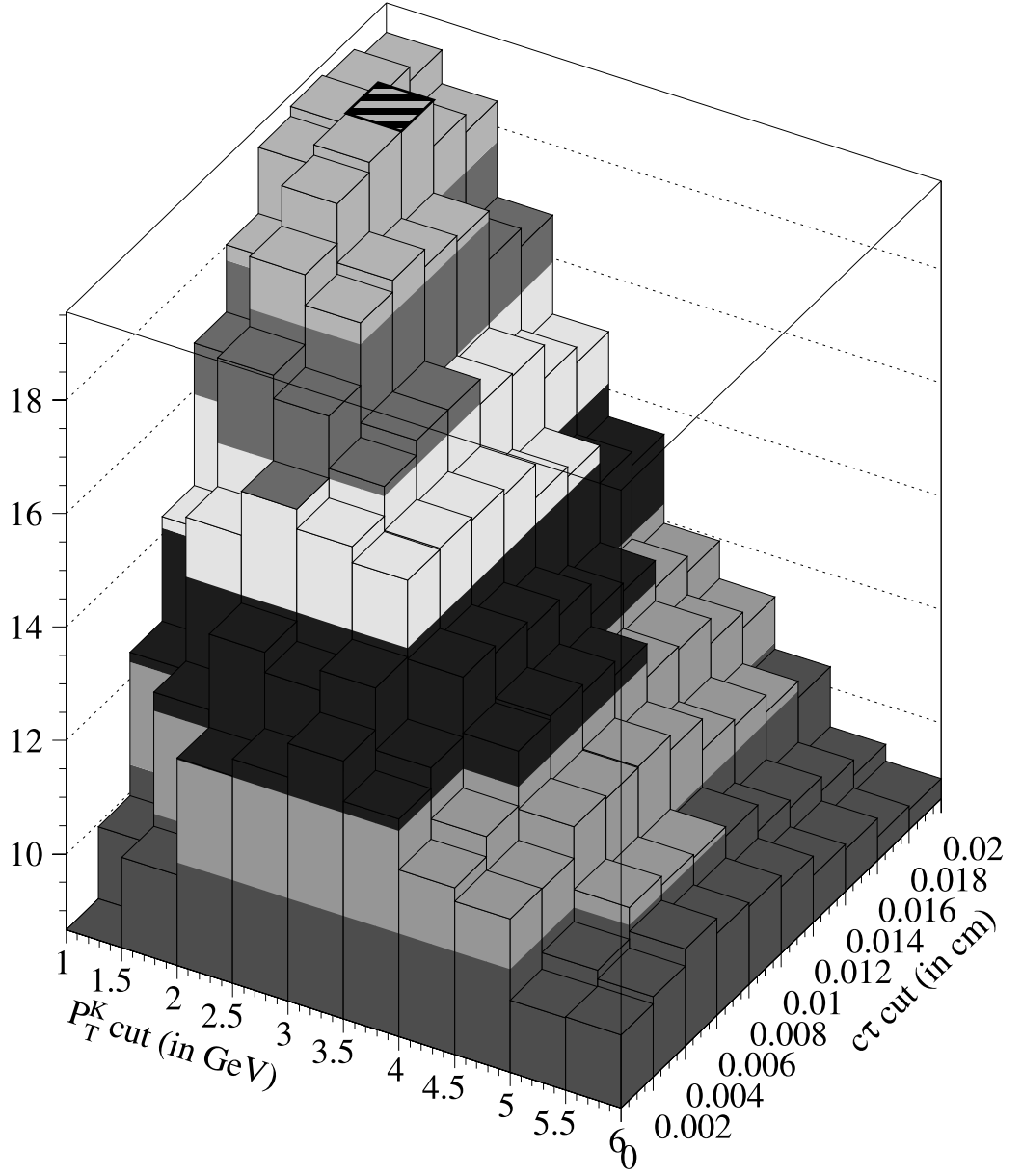


Figure 29: Signal significance $\sqrt{\frac{S^2}{S+B}}$ for $B^+ \rightarrow J/\psi K^+$ events as a function of P_T^K and $c\tau$ cuts. Hatched bin corresponds to optimized set of cuts. Shaded bands represent ~ 2 standard deviation variations in $\sqrt{\frac{S^2}{S+B}}$. In this plot, P_T^B is held constant at the optimized value: $P_T^B > 5.0$ GeV.

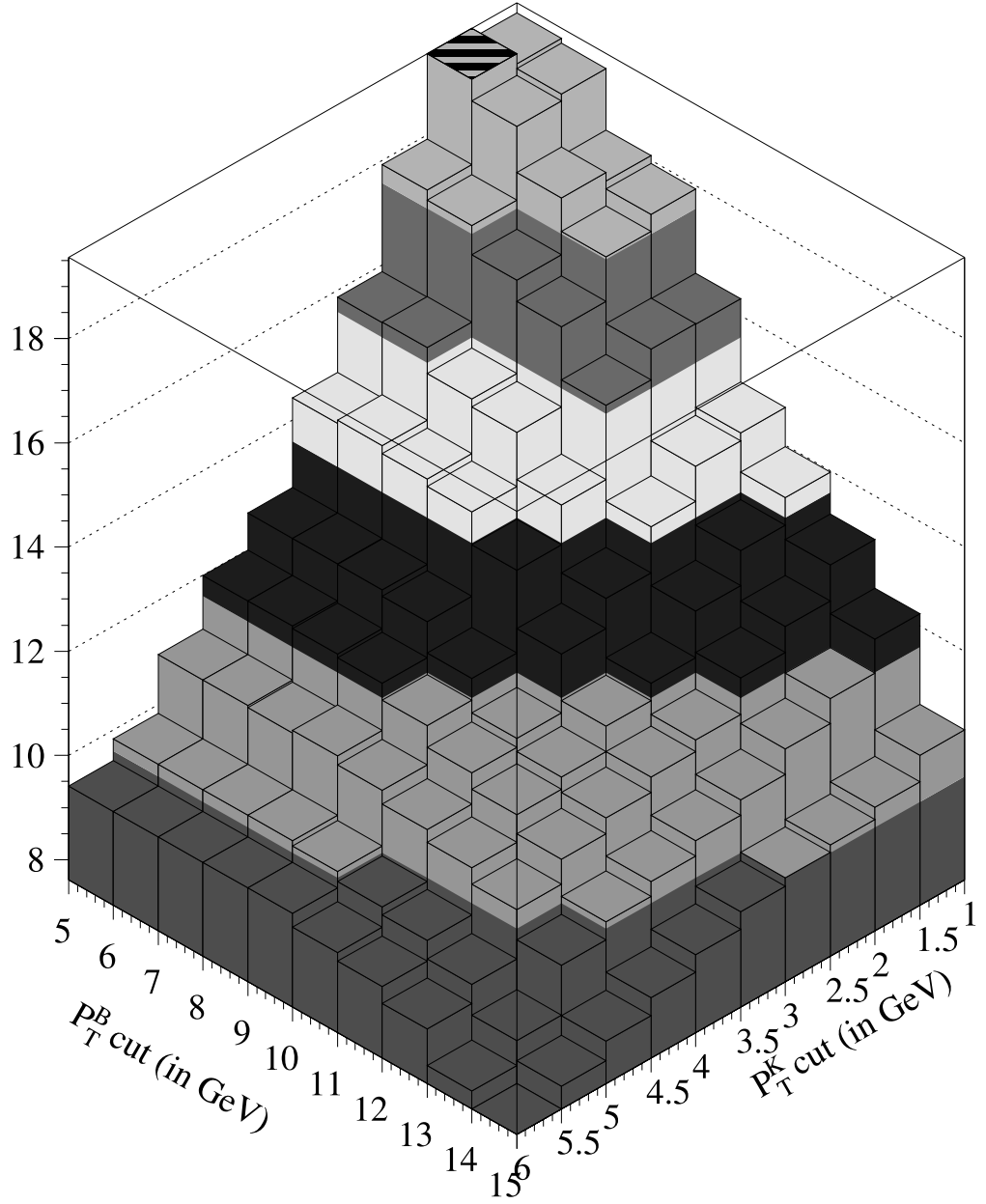


Figure 30: Signal significance $\sqrt{\frac{S^2}{S+B}}$ for $B^+ \rightarrow J/\psi K^+$ events as a function of P_T^B and P_T^K cuts. Hatched bin corresponds to optimized set of cuts. Shaded bands represent ~ 2 standard deviation variations in $\sqrt{\frac{S^2}{S+B}}$. In this plot, $c\tau$ is held constant at the optimized value: $c\tau > 140 \mu\text{m}$.

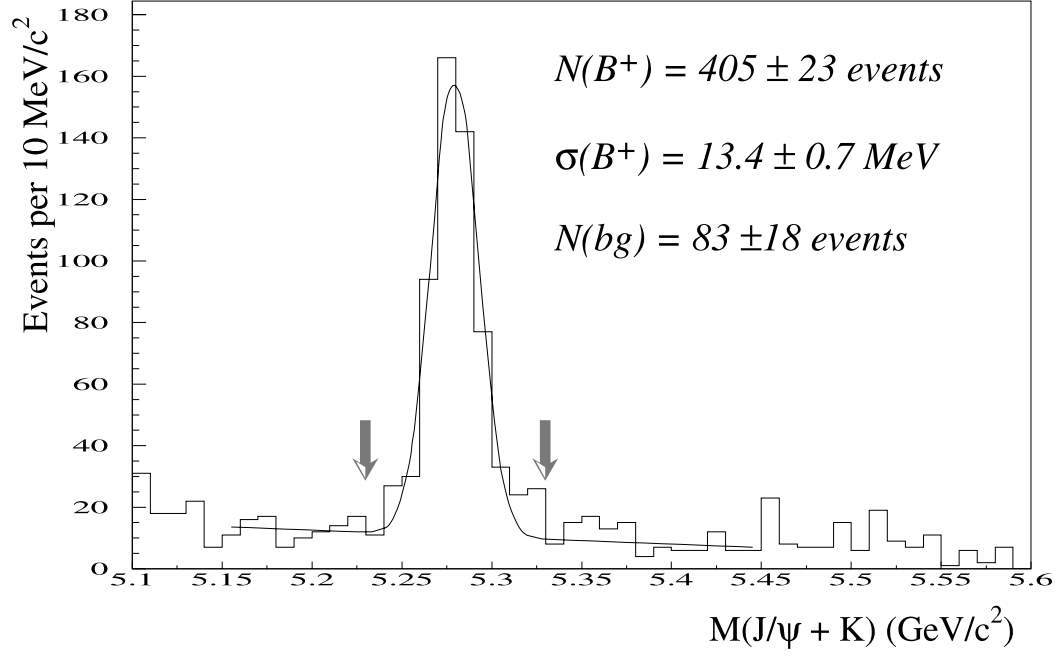


Figure 31: Invariant mass distribution of $B^+ \rightarrow J/\psi K^+$ events selected with the optimized cuts. The arrows indicate the width of the peak region. $N(B^+)$ and $N(bg)$ are the number of signal events and background events in the peak region, respectively.

choice determined by this method is:

$$\begin{aligned}
 P_T^K &> 1.5 \text{ GeV} \\
 P_T^B &> 5.0 \text{ GeV} \\
 c\tau &> 140 \text{ } \mu\text{m}
 \end{aligned}
 \tag{4.3}$$

The statistical significance for this choice of cuts is $\sqrt{\frac{S^2}{S+B}} = 19.6$ and a Gaussian fit to the mass peak plus a linear background gives 450 ± 23 $B^+ \rightarrow J/\psi K^+$ events between $M(J/\psi K^+) = 5.228$ and 5.330 GeV. The mass resolution is found to be 13.4 ± 0.7 MeV and the background is 83 ± 18 events in the peak

| N_K | ϵ_K | N_{bg} |
|--------------|-----------------------|-------------|
| 450 ± 23 | $(14.18 \pm 0.13) \%$ | 83 ± 18 |

Table 7: Number of $B^+ \rightarrow J/\psi K^+$ events (N_K) determined from a fit to the invariant mass distribution, Monte Carlo efficiency (ϵ_K), and estimated background (N_{bg}) in peak region. Errors are statistical only. Cuts used are those listed in Equation 4.3.

region. Figure 31 shows the invariant mass distribution of the $B^+ \rightarrow J/\psi K^+$ events selected with the optimized cuts. These numbers along with the efficiency from the Monte Carlo sample are used later in calculating the $\sigma \cdot \mathcal{B}$ ratios for the B_c hadronic decay modes. Table 7 summarizes these results. The selection of loose momentum cuts by the optimization procedure indicates that the B lifetime is the most effective discriminator between background and data. After applying an optimized $c\tau$ cut, loose momentum cuts simply maximize the acceptance.

Given this relatively clean sample of $B^+ \rightarrow J/\psi K^+$ events, it is possible to cross-check the Monte Carlo distributions to ensure that they can be relied upon for analyzing the yet-unknown B_c decays. Figures 32, 33, 34, and 35 compare the Monte Carlo distributions for $c\tau$, P_T^B , P_T^K , and kaon impact parameter significance with the same distributions for the events in the $B^+ \rightarrow J/\psi K^+$ mass peak, minus the background contributions interpolated from the sideband regions. The error bars in these histograms reflect the statistics in the data only. The shape of all of the distributions for the sideband-subtracted $B^+ \rightarrow J/\psi K^+$ events are in good agreement with the Monte Carlo distributions.

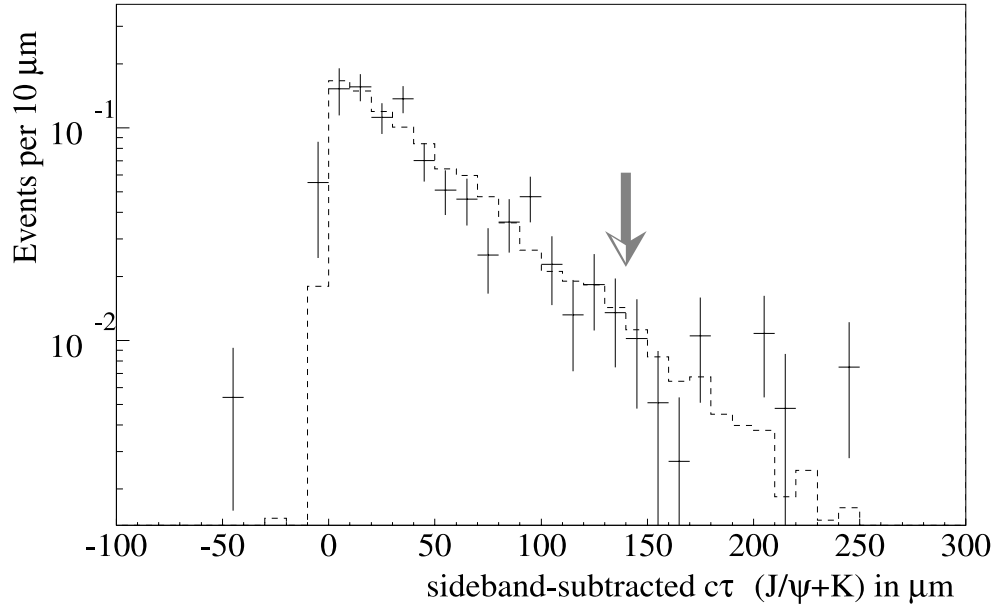


Figure 32: $c\tau$ distribution of $B^+ \rightarrow J/\psi K^+$ events selected with the optimized cuts (except for $c\tau$). Error bars on the data are from statistics only. Dashed histogram represents Monte Carlo events passing the same cuts. The arrow indicates optimized $c\tau$ cut selection. Histograms normalized to same area for shape comparison.

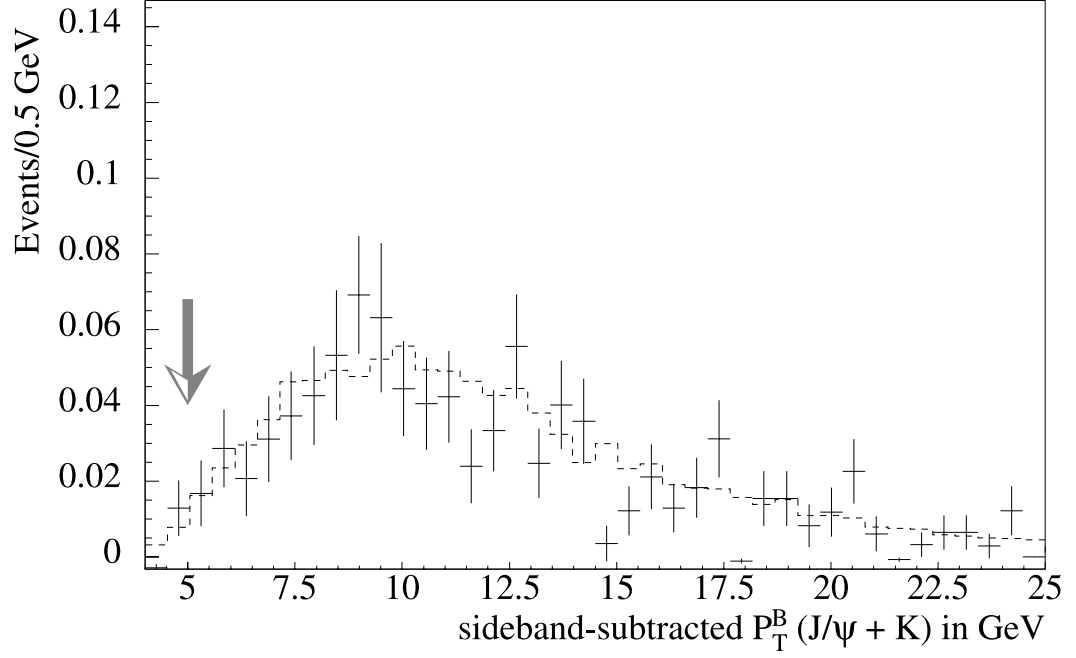


Figure 33: P_T^B distribution of $B^+ \rightarrow J/\psi K^+$ events selected with the optimized cuts (except for P_T^B). Error bars are from data statistics only. Dashed histogram represents Monte Carlo events passing the same cuts. The arrow indicates optimized P_T^B cut selection. Histograms normalized to same area for shape comparison.

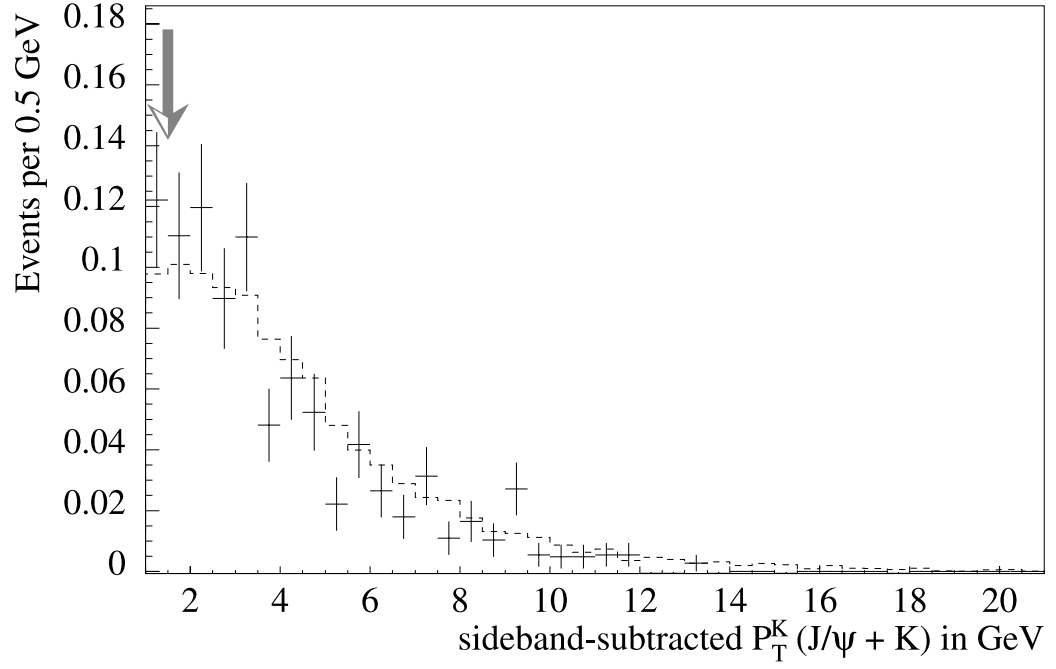


Figure 34: P_T^K distribution of $B^+ \rightarrow J/\psi K^+$ events selected with the optimized cuts (except for P_T^K). Error bars are from data statistics only. Dashed histogram represents Monte Carlo events passing the same cuts. The arrow indicates optimized P_T^K cut selection. Histograms normalized to same area for shape comparison.

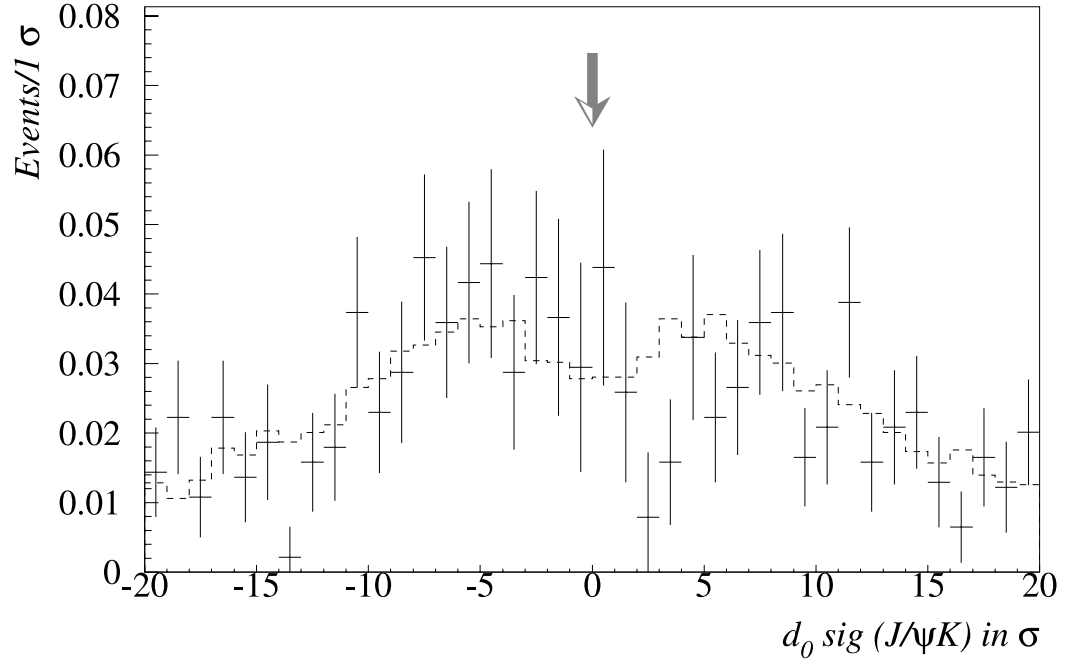


Figure 35: d_0 significance distribution of $B^+ \rightarrow J/\psi K^+$ events selected with the optimized cuts. Error bars are from data statistics only. Dashed histogram represents Monte Carlo events passing the same cuts. Arrow at 0 indicates that no impact parameter cut was used in selecting these events. Histograms normalized to same area for shape comparison.

4.5.5 Background Estimation For B_c Decay Modes

The width of the B_c mass distribution can be estimated by scaling the B^+ mass resolution by the ratio of the meson masses:³⁹

$$\sigma(M_{B_c}) \simeq \sigma(M_{B^+}) \frac{M(B_c)}{M(B^+)} = 13.4 \text{ MeV} \frac{6.2 \text{ GeV}}{5.28 \text{ GeV}} = 16 \text{ MeV}. \quad (4.4)$$

By choosing a mass window of $\pm 3\sigma$ (± 50 MeV) around the nominal B_c mass (taken to be 6.2 GeV from the theoretical predictions), the remainder of the mass spectrum between 5.6 and 6.8 GeV⁴⁰ can be fit to a parametric form (a straight line or constant, depending on statistics) and interpolated into the mass peak window to estimate the background. Even if the true B_c mass lies in a different region of the spectrum, by choosing a wide enough sideband region (> 50 standard deviations) the background events will dominate whatever signal may be present in the sidebands. The $\sigma \cdot \mathcal{B}$ limit is determined as a function of the assumed B_c mass by counting the events in each mass window, interpolating the background from the sidebands to each window, and calculating an upper limit based on these numbers. The selection cuts used in this procedure are those optimized for Monte Carlo events generated with the nominal mass value $M(B_c) = 6.2$ GeV. The detection efficiency from Monte Carlo is similarly determined by generating a given number of events at the center of each mass window. The efficiency is defined as the ratio of the number of events that pass the cuts to the number of events that pass the trigger requirements alone.

³⁹In principle, the B_c mass width could be obtained from Monte Carlo. However, the Monte Carlo does not reproduce the detector resolutions with any great degree of accuracy.

⁴⁰These limits on the range of the B_c mass are chosen to be compatible with the full range of theoretical predictions and with the $B_c^+ \rightarrow J/\psi \mu^+ \nu_\mu$ measurement by CDF.

4.5.6 Estimation of $B_c^+ \rightarrow J/\psi \pi^+$ Signal

In choosing the optimal cuts for selecting $B_c^+ \rightarrow J/\psi \pi^+$ events, the data is used only for estimating background, which cannot be obtained by Monte Carlo alone. The signal events and efficiency are determined by applying the cuts to a “signal” comprised of Monte Carlo events in order to avoid selecting cuts based solely on fluctuations in the data. An estimate of the expected signal size is necessary to normalize the Monte Carlo events. The cuts must be applicable to a small sample of real events, yet must exhibit the smooth variations that come from a large sample of generated events. The only data available on the production cross section of B_c is the $\sigma \cdot \mathcal{B}$ ratio from the trilepton analysis. One may obtain an estimate of cross section times branching ratio for $B_c^+ \rightarrow J/\psi \pi^+$ by scaling this value with a ratio of hadronic-to-leptonic $\sigma \cdot \mathcal{B}$ from ordinary B^+ decays:

$$\sigma_{B_c} \cdot \mathcal{B}(B_c^+ \rightarrow J/\psi \pi^+) \simeq \sigma_{B^+} \cdot \mathcal{B}(B^+ \rightarrow \overline{D}^*(2007)^0 \pi^+) \frac{\sigma_{B_c} \cdot \mathcal{B}(B_c^+ \rightarrow J/\psi \mu^+ \nu_\mu)}{\sigma_{B^+} \cdot \mathcal{B}(B^+ \rightarrow \overline{D}^*(2007)^0 \mu^+ \nu_\mu)}. \quad (4.5)$$

The $\overline{D}^*(2007)^0$ decay modes are chosen because the $\overline{D}^*(2007)^0$ is a vector meson, like the J/ψ , so that the spin-dependent components of the decay matrix elements are comparable.

Using the PDG values [7, p. 40] for these decay fractions⁴¹ and the $\sigma \cdot \mathcal{B}$ ratio of $B_c^+ \rightarrow J/\psi \mu^+ \nu_\mu$ from CDF [13] ($\frac{\sigma \cdot \mathcal{B}(B_c^+ \rightarrow J/\psi \mu^+ \nu_\mu)}{\sigma \cdot \mathcal{B}(B^+ \rightarrow J/\psi K^+)} = 0.132_{-0.037}^{+0.041}(\text{stat.}) \pm 0.031(\text{syst.})_{-0.020}^{+0.032}(\text{lifetime})$), Equation 4.5 is simplified to:

$$\sigma_{B_c} \cdot \mathcal{B}(B_c^+ \rightarrow J/\psi \pi^+) \simeq \sigma_{B^+} \cdot \mathcal{B}(B^+ \rightarrow J/\psi K^+) \cdot (1.15 \pm 0.57) \times 10^{-2}. \quad (4.6)$$

The cross section times branching ratio for each decay mode is related to the

⁴¹ $\Gamma(\overline{D}^*(2007)^0 \pi^+)/\Gamma_{total} = 0.0046 \pm 0.0004$. $\Gamma(\overline{D}^*(2007)^0 \mu^+ \nu_\mu)/\Gamma_{total} = 0.053 \pm 0.008$.

number of observed events via the relations:

$$N(J/\psi K^+) = \epsilon_K \cdot \sigma_{B^+} \cdot \mathcal{B}(B^+ \rightarrow J/\psi K^+) \cdot \int \mathcal{L} dt \quad (4.7)$$

and

$$N(J/\psi \pi^+) = \epsilon_\pi \cdot \sigma_{B_c} \cdot \mathcal{B}(B_c^+ \rightarrow J/\psi \pi^+) \cdot \int \mathcal{L} dt. \quad (4.8)$$

The integrated luminosity is imprecisely known, but is common to all decay channels, so it can be factored out. The quantity $\sigma \cdot \mathcal{B}(J/\psi K^+)$ is estimated from Equation 4.7 using the results of Table 7 to obtain:

$$\sigma_{B^+} \cdot \mathcal{B}(B^+ \rightarrow J/\psi K^+) \cdot \int \mathcal{L} dt \simeq (3.17 \pm 0.16) \times 10^3 \text{ events}. \quad (4.9)$$

Substituting into Equation 4.6 gives the estimated number of $B_c^+ \rightarrow J/\psi \pi^+$ to which the Monte Carlo sample will be scaled:

$$\frac{N(J/\psi \pi^+)}{\epsilon_\pi} \simeq 36.3 \pm 18.0 \text{ events}. \quad (4.10)$$

4.6 Optimized Selection of $B_c^+ \rightarrow J/\psi \pi^+$ Events

In the same way that cuts are chosen to maximize the $\sqrt{\frac{S^2}{S+B}}$ significance of the $B^+ \rightarrow J/\psi K^+$ events, the generalized statistic x_S is maximized over a set of cuts. The signal events used in calculating x_S are taken from Monte Carlo with the expected normalization of Equation 4.10 and the background is measured by averaging the number of events in a wide mass window around the nominal B_c mass. The limits of the cut variation are the same as those for the $B^+ \rightarrow J/\psi K^+$ optimization, with the following exceptions:

- (1) The minimum P_T^π considered is 1.5 GeV. Daughters from the heavier B_c decay are expected to have a harder momentum distribution than those from B^+ decay. The optimized P_T^K cut for

$B^+ \rightarrow J/\psi K^+$ is chosen as the minimum of the pion P_T for B_c decay.

- (2) The impact parameter significance cut of the pion is allowed to vary from 0 to 10 standard deviations. While this cut was not used in selecting $B^+ \rightarrow J/\psi K^+$ events because of the known existence of a large signal, it may be useful in reducing combinatoric background in searching for $B_c^+ \rightarrow J/\psi \pi^+$ events.

There are now six orthogonal 2-dimensional slices that can be made through the 4-dimensional space of cut variables. Of the $6 \times 10^2 = 600$ possible histograms that completely specify the variation of x_S with all four cut variables, Figures 36 and 37 display those six planes that mutually pass through the set of cuts chosen to maximize x_S . The set of cuts that optimizes x_S for the $B_c^+ \rightarrow J/\psi \pi^+$ channel is:

$$\begin{aligned}
P_T^\pi &> 2.5 \text{ GeV} \\
P_T^B &> 7.0 \text{ GeV} \\
c\tau &> 120 \text{ } \mu\text{m} \\
\text{pion } d_0 \text{ sig.} &> 3\sigma
\end{aligned} \tag{4.11}$$

The value of x_S for this set of cuts is 1.54 (σ). This corresponds to a scaled Monte Carlo size of 3.56 events, with a background contribution in the B_c mass peak region of 2.73 events. Figure 38 displays the $B_c^+ \rightarrow J/\psi \pi^+$ data events (used to calculate background), with the scaled Monte Carlo distribution for the optimized x_S cuts. Table 8 summarizes the size of the data sample after optimization and the efficiency calculated with the Monte Carlo. The efficiency is used in the $\sigma \cdot \mathcal{B}$ ratio determination.

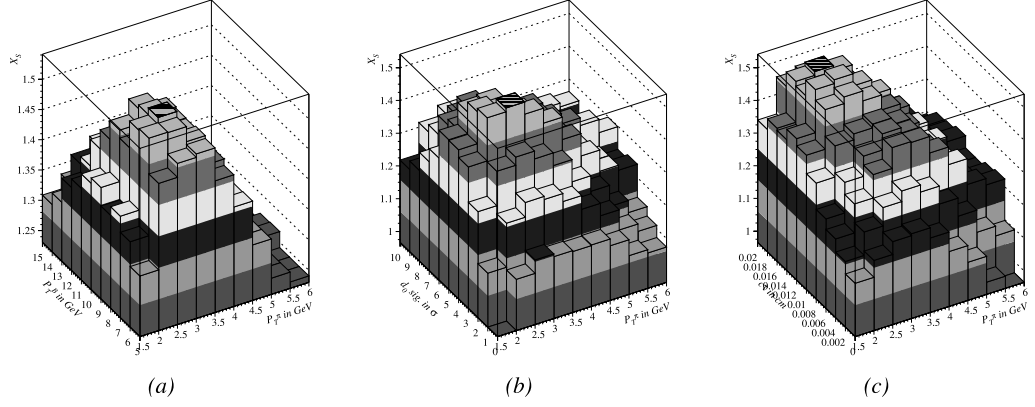


Figure 36: Statistical significance x_S for $B_c^+ \rightarrow J/\psi\pi^+$ events as a function of cut variables. Hatched bin corresponds to optimized set of cuts. Shaded bands represent ~ 0.3 standard deviation variations in x_S . Cut variables not represented by each distribution are fixed to optimal values. Figure (a) shows variation of x_S with choices of P_T^π and P_T^B cuts. Figure (b) shows variation with P_T^π and pion d_0 significance. Figure (c) show variation with P_T^π and $c\tau$ cuts.

| N_π | ϵ_π |
|------------|----------------------|
| 32 (total) | $(3.13 \pm 0.09) \%$ |

Table 8: Total number of $B_c^+ \rightarrow J/\psi\pi^+$ candidate events in the mass range 5.6 – 6.8 GeV and efficiency determined with Monte Carlo. Errors are statistical only. Cuts used are those listed in Equation 4.11.

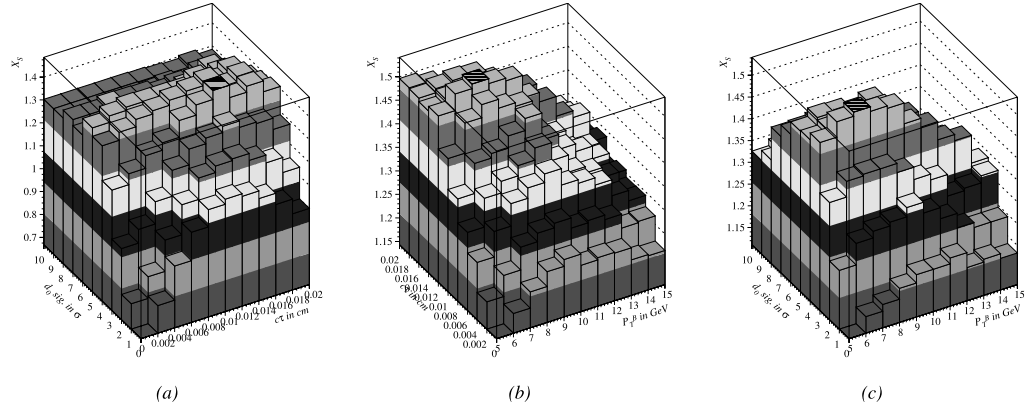


Figure 37: Statistical significance x_S for $B_c^+ \rightarrow J/\psi \pi^+$ events as a function of cut variables. Hatched bin corresponds to optimized set of cuts. Shaded bands represent ~ 0.3 standard deviation variations in x_S . Cut variables not represented by each distribution are fixed to optimal values. Figure (a) shows variation of x_S with choices of $c\tau$ and pion d_0 significance cuts. Figure (b) shows variation with P_T^B and $c\tau$ cuts. Figure (c) show variation with P_T^B and pion d_0 significance cuts.

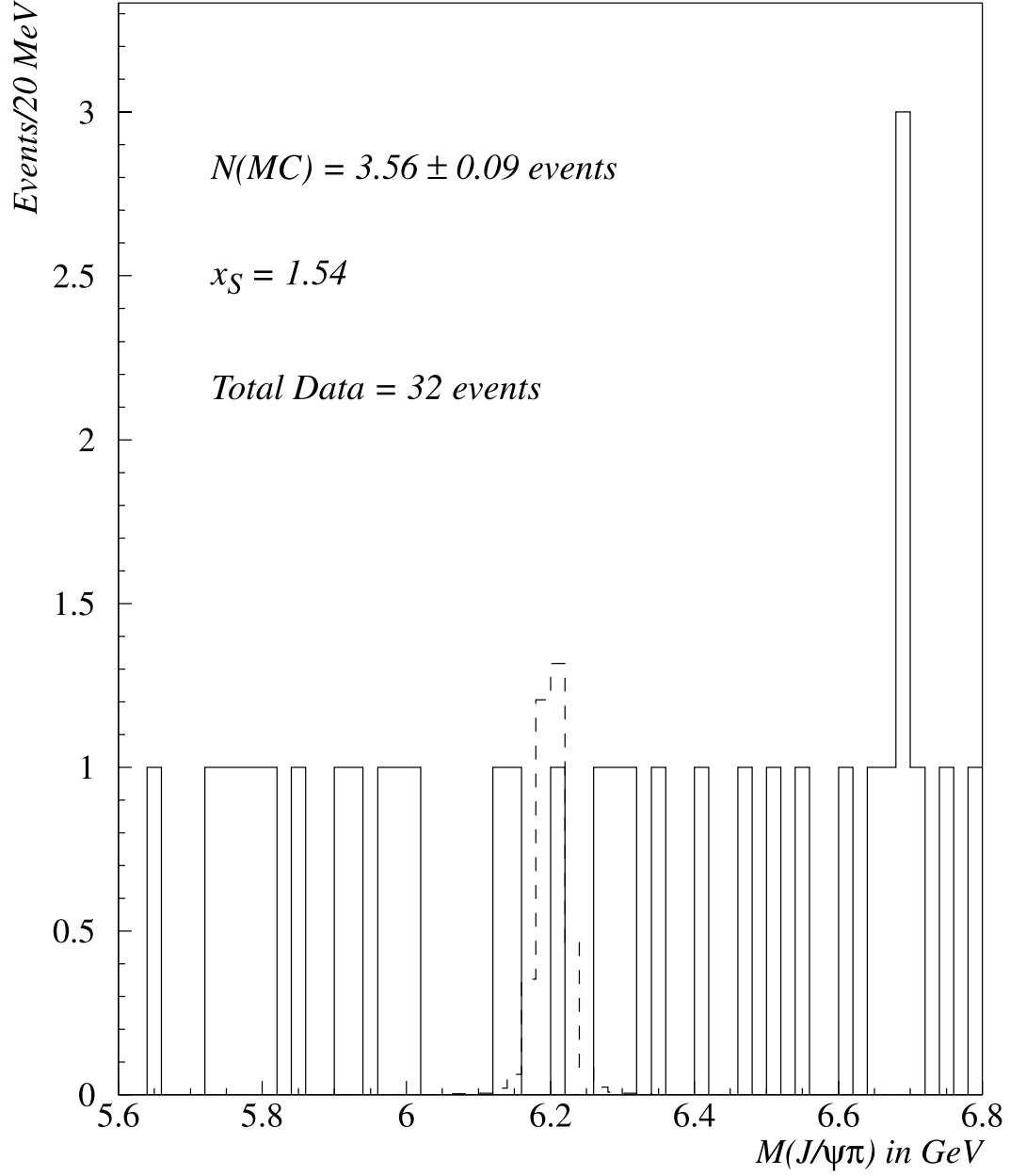


Figure 38: Mass distribution of $B_c^+ \rightarrow J/\psi \pi^+$ candidate events passing the final selection of Equation 4.11. Monte Carlo sample normalized to the expected signal size is overlaid. Statistical significance x_S is 1.54 for this set of cuts.

Examination of the x_S distributions indicates that both the proper lifetime and the impact parameter significance cuts are the most effective at maximizing the signal significance. The distributions are relatively flat over a large range in P_T^B . Use of the high-statistics Monte Carlo sample normalized to a small number of events together with the x_S significance, which was designed to provide a consistent generalization of $\sqrt{\frac{S^2}{S+B}}$ valid over a wider range of sample sizes, make the optimization procedure insensitive to fluctuations in the data. Figures 39 and 40 display the distributions of the relevant kinematic and geometric variables of the data using the final event selection requirements. The lack of a significant excess of events in any region in Figure 38 yields only an upper limit on the production cross section of the B_c times the branching ratio of the B_c to $J/\psi\pi$.

4.7 Selection of $B_c^+ \rightarrow J/\psi\pi^+\pi^-\pi^+$ Events

To search for the decay mode $B_c^+ \rightarrow J/\psi\pi^+\pi^-\pi^+$, no additional optimization of the cuts is necessary. Using the PDG value: [7, p.40]

$$\frac{\Gamma(B^+ \rightarrow \overline{D}^*(2007)^0\pi^+\pi^-\pi^+)}{\Gamma(B^+ \rightarrow \overline{D}^*(2007)^0\pi^+)} = \frac{(9.4 \pm 2.6) \times 10^{-3}}{(4.6 \pm 0.4) \times 10^{-3}} \quad (4.12)$$

and Equations 4.5 and 4.10, one obtains an estimate of

$$\frac{N(J/\psi\pi^+\pi^-\pi^+)}{\epsilon_{3\pi}} \simeq 74.1 \pm 40.4 \text{ events.} \quad (4.13)$$

This is roughly twice the number of scaled $B_c^+ \rightarrow J/\psi\pi^+$ events obtained in the x_S optimization for the single-pion case. Despite the larger expected branching fraction, the cut efficiencies are more than a factor of two smaller than the corresponding single-pion efficiencies due to the larger fraction of combinatoric background. If no excess is observed in the $B_c^+ \rightarrow J/\psi\pi^+$ channel, one should not expect to observe any $B_c^+ \rightarrow J/\psi\pi^+\pi^-\pi^+$ events. There

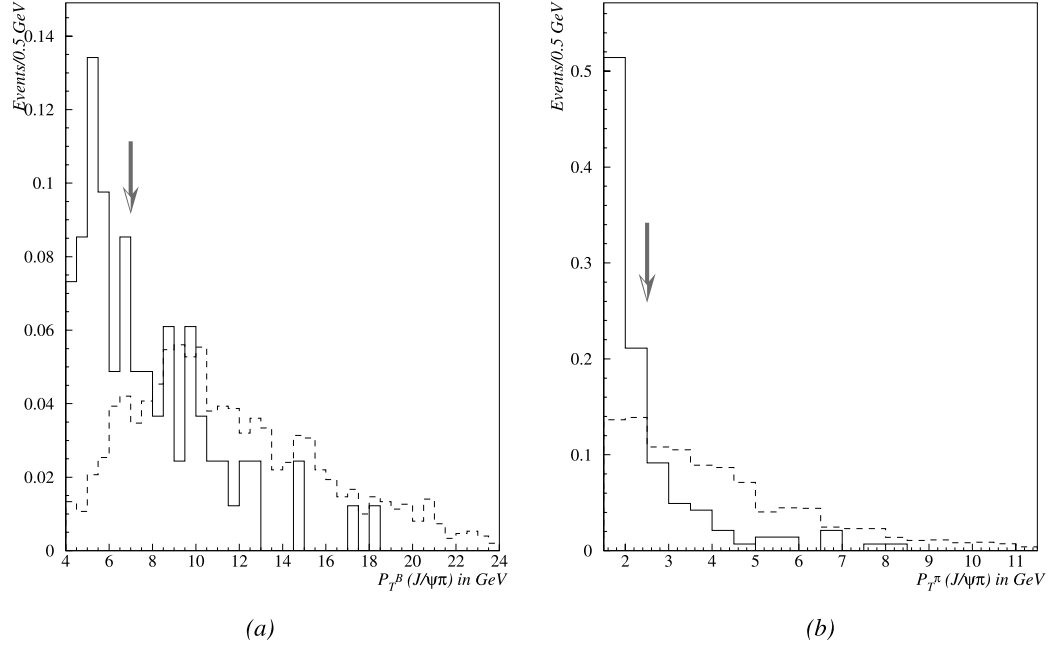


Figure 39: (a) P_T^π distribution for $B_c^+ \rightarrow J/\psi\pi^+$ events passing optimized cuts. (b) P_T^B distribution for same events. Dashed histograms are Monte Carlo $B_c^+ \rightarrow J/\psi\pi^+$ events passing the same cuts. Arrows indicate cut selection.

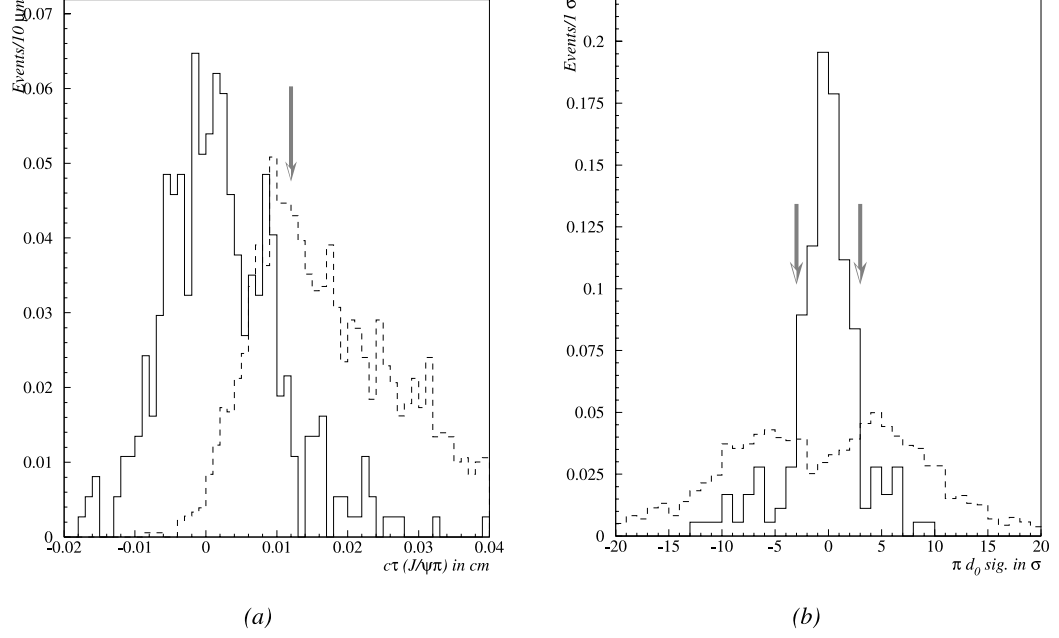


Figure 40: (a) $c\tau$ distribution for $B_c^+ \rightarrow J/\psi\pi^+$ events passing optimized cuts. (b) pion d_0 significance distribution for same events. Dashed histograms are Monte Carlo $B_c^+ \rightarrow J/\psi\pi^+$ events passing the same cuts. The arrows indicate cut selection.

are also more pragmatic reasons for not optimizing the cuts for this channel. The computation time necessary for sampling all of the possible combinations of cuts grows exponentially with the number of cut variables. To optimize the three-pion channel properly, one should allow for different, looser cuts on the second and third pions. Instead of four possible cut variables, one could easily construct eight or more for the three-pion case. Even if one reduced the granularity of the sampling procedure, the methodical nature of the **FORTRAN** routines that access the data on disk and perform the necessary statistical calculations translates into weeks of computer time for such a case. Additionally, it is desirable to use similar cuts across the decay channels for internal consistency in the analysis.

The cut selection used for this sample is:

$$\begin{aligned}
&\text{at least one } \pi \text{ with } P_T^\pi > 2.5 \text{ GeV} \\
&P_T^B > 7.0 \text{ GeV} \\
&c\tau > 120 \text{ } \mu\text{m} \\
&\text{at least one } \pi \text{ with } d_0 \text{ sig.} > 3\sigma
\end{aligned} \tag{4.14}$$

The invariant mass distribution for $B_c^+ \rightarrow J/\psi \pi^+ \pi^- \pi^+$ events selected with this set of cuts is shown in Figure 41. A Monte Carlo sample of $B_c^+ \rightarrow J/\psi \pi^+ \pi^- \pi^+$ events normalized to the expected value given in Equation 4.13 is overlaid onto this plot. The total number of events in the data spectrum is 41, and the normalized Monte Carlo sample contains 1.14 ± 0.62 events.⁴² Table 9 summarizes the total number of $B_c^+ \rightarrow J/\psi \pi^+ \pi^- \pi^+$ events and the detection efficiency from Monte Carlo, which are used in the determination of $\sigma \cdot \mathcal{B}$ for this decay channel. As with the $B_c^+ \rightarrow J/\psi \pi^+$ channel, there is no

⁴²The uncertainty on this number is due to the large uncertainty on the normalization factor, not due to Monte Carlo statistics.

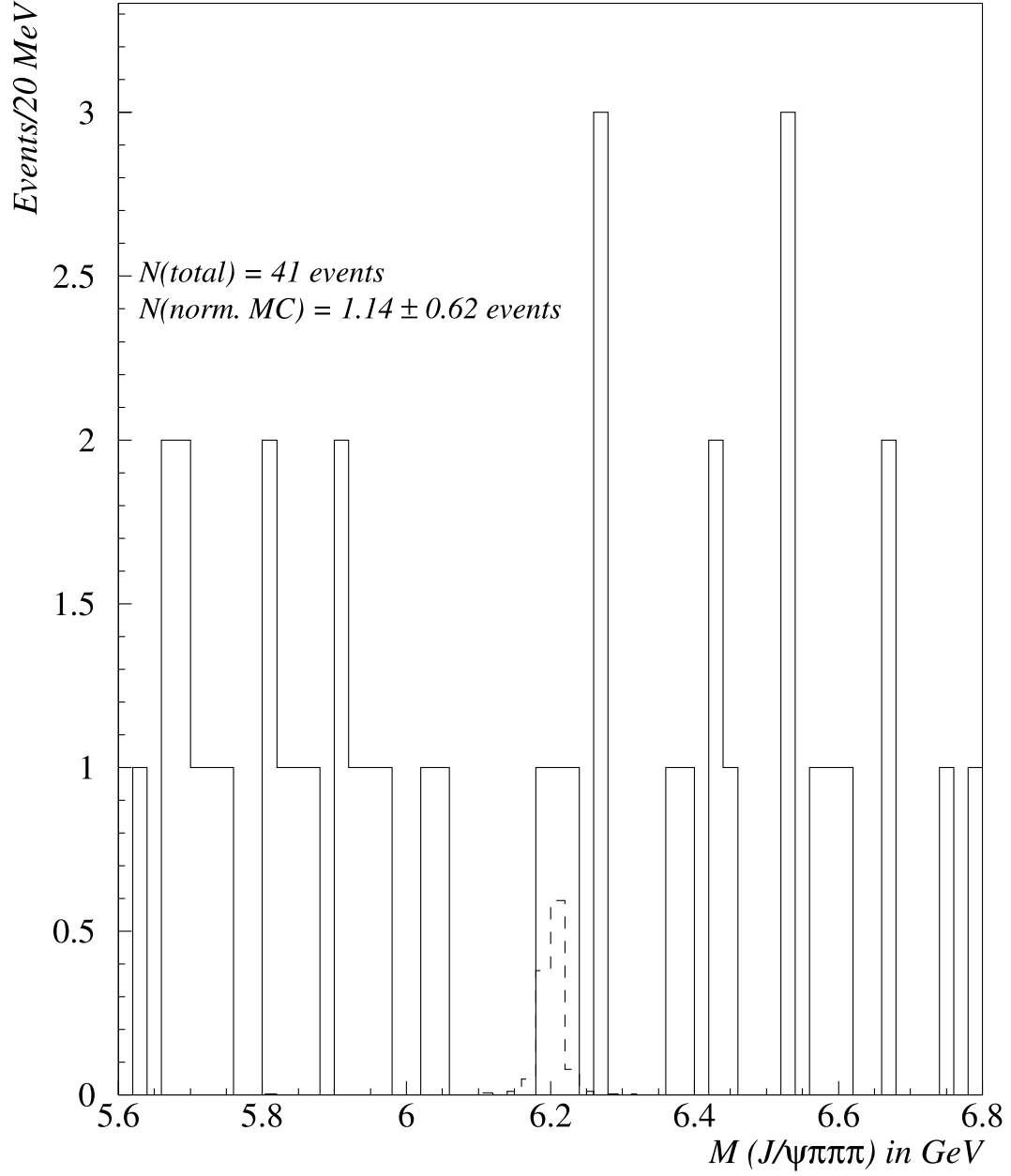


Figure 41: Invariant mass distribution of $B_c^+ \rightarrow J/\psi\pi^+\pi^-\pi^+$ events selected with cuts optimized for $B_c^+ \rightarrow J/\psi\pi^+$. Monte Carlo sample normalized to the expected signal size is overlaid.

statistically significant excess of events over background in any region of the invariant mass spectrum. Therefore, an upper limit will be set on the $\sigma \cdot \mathcal{B}$ for $B_c^+ \rightarrow J/\psi \pi^+ \pi^- \pi^+$.

| $N_{3\pi}$ | $\epsilon_{3\pi}$ |
|------------|----------------------|
| 41 (total) | $(2.38 \pm 0.10) \%$ |

Table 9: Total number of $B_c^+ \rightarrow J/\psi \pi^+ \pi^- \pi^+$ candidate events in the mass range 5.6 – 6.8 GeV and detection efficiency from Monte Carlo. Errors are statistical only. Cuts used are those listed in Equation 4.14.

Figure 42 compares the proper lifetime and P_T^B distributions of the data with the Monte Carlo calculations. The $c\tau$ plot with the impact parameter significance cut applied clearly demonstrates the correlated nature of the impact parameter with the B lifetime. Referring to Equation 2.2, for a pion track with $P_T = 1$ GeV (the minimum P_T considered for any track), the resolution of the impact parameter is $\sim 50 \mu\text{m}$. To pass the impact parameter significance cut, such a track would need a reconstructed $d_0 > 150 \mu\text{m}$. For pions from a real B , which are produced with momenta primarily along the direction of the parent meson, this condition is not generally satisfiable for small decay lengths. There is no such restriction on the background tracks combined with a prompt J/ψ . For a 3σ cut on the impact parameter, it is clear that a $c\tau$ cut of $\sim 100 \mu\text{m}$ or greater is necessary to reduce background. The long positive lifetime distribution of the data that survive the d_0 cut indicates that some of the events are from real B mesons with unassociated background tracks passing near the decay vertex. Figure 43 compares the P_T^π and pion d_0 significance distributions for the highest- and lowest-momentum pions. The similarity of the shapes of these distributions further indicates that a sizable

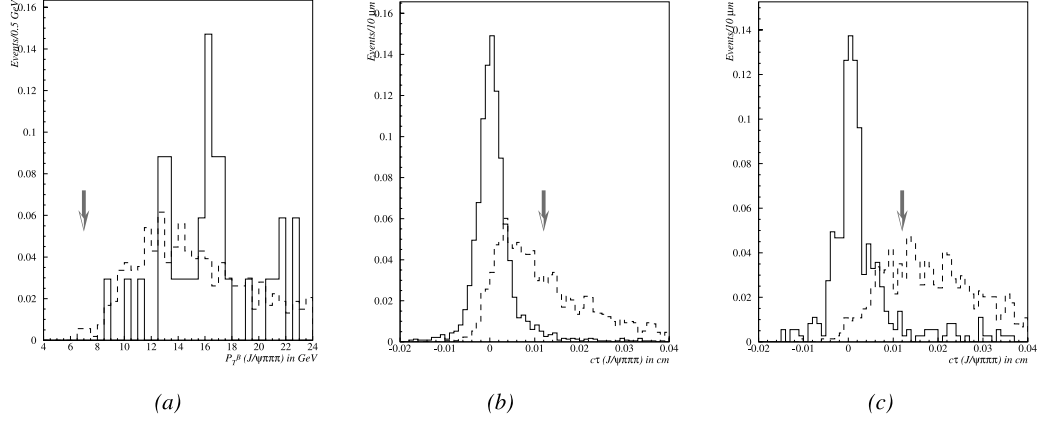


Figure 42: (a) P_T^B distribution for $B_c^+ \rightarrow J/\psi \pi^+ \pi^- \pi^+$ events compared with Monte Carlo sample. (b) $c\tau$ distribution for $B_c^+ \rightarrow J/\psi \pi^+ \pi^- \pi^+$ events compared with Monte Carlo sample. No impact parameter significance cut was applied to this plot. (c) $c\tau$ distribution for $B_c^+ \rightarrow J/\psi \pi^+ \pi^- \pi^+$ events compared with Monte Carlo sample, including d_0 significance cut. Solid lines are data, dashed are Monte Carlo. All histograms are normalized to the same area for shape comparison. Cuts used are those of 4.14 except for the cut variable displayed. Arrows indicate cut selection.

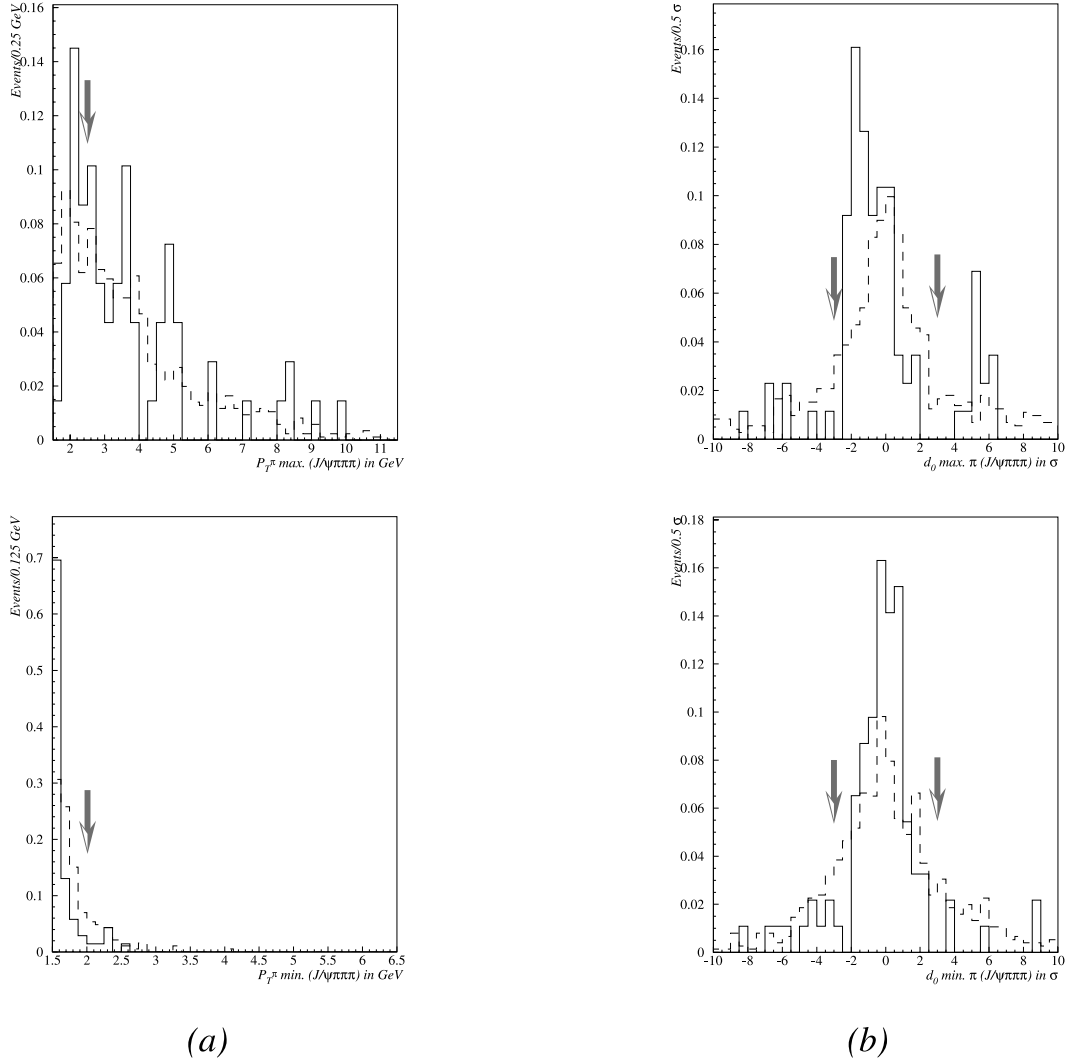


Figure 43: (a) Upper plot is P_T^π distribution for highest P_T pion in $B_c^+ \rightarrow J/\psi\pi^+\pi^-\pi^+$ events. Lower plot is the same distribution for lowest P_T pion. (b) Pion d_0 Distribution for $B_c^+ \rightarrow J/\psi\pi^+\pi^-\pi^+$ events compared with Monte Carlo. Solid lines are data, dashed are Monte Carlo. All histograms are normalized to the same area for shape comparison. Cuts used are those of 4.14 except for the cut variable displayed. Arrows indicate cut selection (only one of the three added tracks need pass the cut).

fraction of other B decays contribute to these events. One more observation about the impact parameter distributions bears further consideration. A large fraction of each distribution shifts by $\sim 1.0\sigma$ in opposite directions, depending on the relative P_T . The pion with the highest P_T shifts downward in the d_0 significance, whereas the pion with the least P_T shifts upward. This is a purely geometric effect, as illustrated by Figure 44. It can be proven under rather general assumptions⁴³ that the average P_T for unassociated tracks which happen to fall near the secondary vertex is larger for those events with negative d_0 and smaller for positive d_0 . Note that the diagrams in Figure 44 are only a representative case. For a range of d_0 angles about the primary vertex, it is possible to construct a larger P_T for the positively signed impact parameter than the negative. When integrated uniformly over all angles, however, the negatively signed d_0 has a higher average P_T .

⁴³The first assumption is that the displacement of the secondary vertex is much larger than d_0 , which is nearly always true. The second is that the impact parameter vector is symmetric about the primary vertex. This latter assumption is true for random tracks coming from the primary that pass near the J/ψ vertex, but is not true for B daughters. Hence the Monte Carlo distributions remain invariant under selection of relative pion momentum. (*i.e.*, the d_0 distribution of the smallest P_T pion is the same as that for the largest P_T pion.)

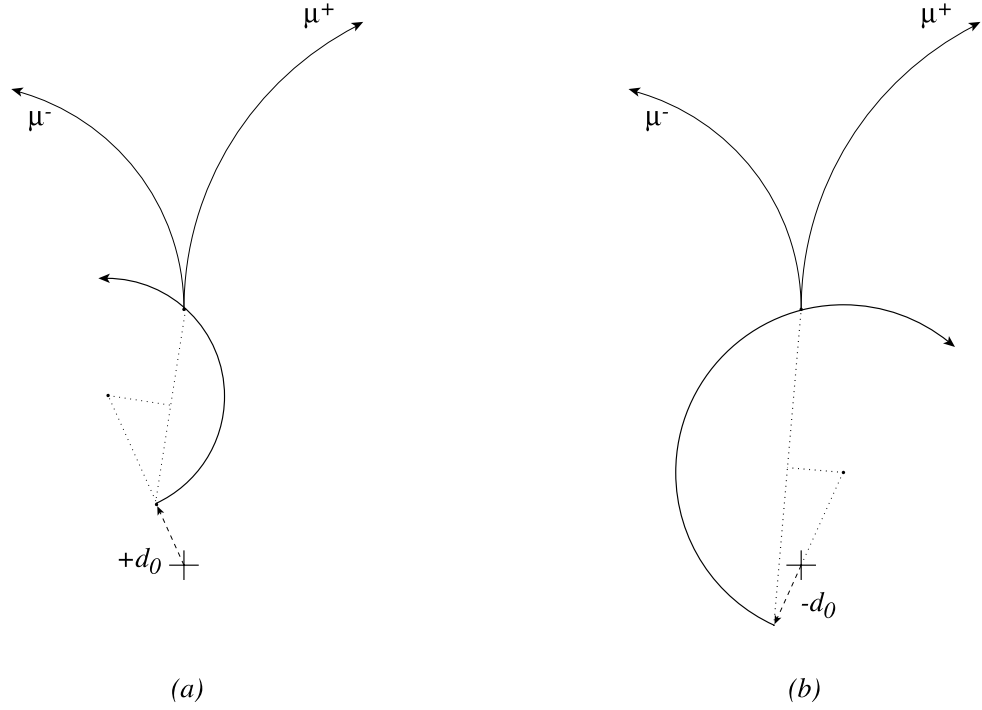


Figure 44: Figure (a) illustrates geometric construction of momentum, given a positive d_0 and a displaced vertex that the track helix must intersect. Figure (b) constructs the momentum from a negative d_0 (of the same magnitude and opposite direction) and the same displaced vertex. The cross indicates the position of the primary vertex. Momentum is proportional to the turning radius of the helix. Track curvatures and distance scales are greatly exaggerated for illustrative purposes.

Chapter 5

Efficiency Corrections and Systematic Uncertainties

5.1 Introduction

The Monte Carlo efficiencies calculated to this point assume nominal values for the B_c lifetime, mass, and choice of fragmentation function. These quantities are based on the measurement of $B_c^+ \rightarrow J/\psi \mu^+ \nu_\mu$ and on theoretical considerations. The missing neutrino momentum in the $B_c^+ \rightarrow J/\psi \mu^+ \nu_\mu$ measurement prohibits a precise reconstruction of the mass and lifetime of the B_c , and the theoretical assumptions that form the basis of the hadronization scheme are not known to any great degree of accuracy. To determine the systematic uncertainties on the efficiencies, the mass, lifetime, and fragmentation models are varied. Additionally, the Monte Carlo calculations assume that the daughter pions and kaons from B decays are stable, and that the tracking efficiency for detecting a pion is the same as that for a kaon. These simplified assumptions need to be examined more closely to determine their validity.

5.2 Uncertainty of B_c Mass

In calculating the nominal efficiencies for the B_c decay channels, I have used Monte Carlo samples with a fixed value of $M_{B_c} = 6.2$ GeV. The uncertainty on the B_c mass is large, however, so it is necessary to determine upper limits of $\sigma \cdot \mathcal{B}$ over the entire range of possible mass values. Since a separate limit is calculated for each 100 MeV mass bin, I generate twelve Monte Carlo samples with $M_{B_c} = 5.6, \dots, 6.7$ GeV. An independent calculation of the efficiency

is performed for each of the 100 MeV bins in mass. The variation is small, but measurable with the Monte Carlo statistics.⁴⁴ For the $B_c^+ \rightarrow J/\psi\pi^+$ events, the efficiency dropped from a maximum of $(3.27 \pm 0.09)\%$ at 5.6 GeV to $(3.02 \pm 0.08)\%$ at 6.8 GeV. These results are tabulated in Table 10. For

| M_{B_c} GeV | ϵ_π |
|---------------|----------------------|
| 5.6 | $(3.27 \pm 0.09) \%$ |
| 5.7 | $(3.21 \pm 0.09) \%$ |
| 5.8 | $(3.25 \pm 0.09) \%$ |
| 5.9 | $(3.22 \pm 0.09) \%$ |
| 6.0 | $(3.18 \pm 0.09) \%$ |
| 6.1 | $(3.19 \pm 0.09) \%$ |
| 6.2 | $(3.13 \pm 0.09) \%$ |
| 6.3 | $(3.12 \pm 0.09) \%$ |
| 6.4 | $(3.09 \pm 0.08) \%$ |
| 6.5 | $(3.11 \pm 0.09) \%$ |
| 6.6 | $(3.08 \pm 0.08) \%$ |
| 6.7 | $(3.02 \pm 0.08) \%$ |

Table 10: Efficiency of $B_c^+ \rightarrow J/\psi\pi^+$ events with optimized cuts, as a function of the assumed B_c mass. Errors are statistical only.

the $B_c^+ \rightarrow J/\psi\pi^+\pi^-\pi^+$ channel, the efficiency calculated with Monte Carlo rose as a function of the B_c mass from $(1.84 \pm 0.08)\%$ for $M_{B_c} = 5.6$ GeV to $(2.53 \pm 0.11)\%$ at 6.8 GeV. Table 11 enumerates these results.

⁴⁴The Monte Carlo samples vary in size, depending on the relative accuracy desired. All samples contain at least 1M generated events prior to event selection.

| M_{B_c} GeV | $\epsilon_{3\pi}$ |
|---------------|----------------------|
| 5.6 | $(1.84 \pm 0.08) \%$ |
| 5.7 | $(1.88 \pm 0.08) \%$ |
| 5.8 | $(1.91 \pm 0.09) \%$ |
| 5.9 | $(2.12 \pm 0.09) \%$ |
| 6.0 | $(2.24 \pm 0.10) \%$ |
| 6.1 | $(2.28 \pm 0.10) \%$ |
| 6.2 | $(2.38 \pm 0.10) \%$ |
| 6.3 | $(2.49 \pm 0.11) \%$ |
| 6.4 | $(2.47 \pm 0.10) \%$ |
| 6.5 | $(2.46 \pm 0.10) \%$ |
| 6.6 | $(2.50 \pm 0.11) \%$ |
| 6.7 | $(2.53 \pm 0.11) \%$ |

Table 11: Efficiency of $B_c^+ \rightarrow J/\psi \pi^+ \pi^- \pi^+$ events with optimized cuts, as a function of the assumed B_c mass. Errors are statistical only.

5.3 Uncertainty of B_c Lifetime

In the previous CDF analysis of hadronic B_c decays, [36] only theoretical predictions for the lifetime were available. Using the lifetime measurement, $\tau = (0.46^{+0.18}_{-0.16}) \times 10^{-12}$ s, [13, 7, p. 45] the input lifetime to CLEOMC is varied between 0.30 and 0.64 ps. The variation in the efficiencies from the nominal value is then taken to be the systematic uncertainty. Tables 12 and 13 summarize these results.

| τ_{B_c} | ϵ_π |
|--------------|----------------------|
| 0.30 ps | $(2.06 \pm 0.07) \%$ |
| 0.46 ps | $(3.13 \pm 0.09) \%$ |
| 0.64 ps | $(4.23 \pm 0.10) \%$ |

Table 12: Efficiency of $B_c^+ \rightarrow J/\psi\pi^+$ events with optimized cuts, as a function of the assumed B_c lifetime. Errors are statistical only.

| τ_{B_c} | $\epsilon_{3\pi}$ |
|--------------|----------------------|
| 0.30 ps | $(1.46 \pm 0.08) \%$ |
| 0.46 ps | $(2.38 \pm 0.10) \%$ |
| 0.64 ps | $(3.26 \pm 0.11) \%$ |

Table 13: Efficiency of $B_c^+ \rightarrow J/\psi\pi^+$ events with optimized cuts, as a function of the assumed B_c lifetime. Errors are statistical only.

The efficiency increases approximately exponentially with lifetime, as expected.⁴⁵ Selecting the largest variation, the systematic uncertainty on ϵ_π is 1.10% and the systematic uncertainty on $\epsilon_{3\pi}$ is 0.92%.

⁴⁵As the lifetime increases, the integral over the events with $c\tau > 120\mu\text{m}$ increases exponentially as well.

5.4 Uncertainty of Fragmentation

In the absence of any experimental motivation for preferring one fragmentation scheme over another, or one set of parameters over another, I vary the default fragmentation function of B_c (Equation 3.1) by setting the c -quark mass 1 standard deviation below its nominal value. This is equivalent to varying the input parameter R from its default value of 0.25 to 0.196. I also generate another Monte Carlo sample with the Peterson fragmentation function. This function is generally used for fragmenting the b -quarks to B mesons containing a light quark. Using Peterson's scaling principle for the quark masses, I set the parameter value to $\epsilon_P = (m_c/m_b)^2 = (\frac{1.4 \text{ GeV}}{4.7 \text{ GeV}})^2 = 0.09$.⁴⁶ Tables 14 and 15 give the numerical results. The largest variation for $B_c^+ \rightarrow J/\psi\pi^+$ is 0.12%

| <i>Fragmentation Function</i> | ϵ_π |
|---|----------------------|
| B_c Frag. ($R = 0.25$) (default) | $(3.13 \pm 0.09) \%$ |
| B_c Frag. ($R = 0.196$) | $(3.25 \pm 0.09) \%$ |
| Peterson ($\epsilon_P = 0.09$) | $(3.16 \pm 0.08) \%$ |

Table 14: Efficiency of $B_c^+ \rightarrow J/\psi\pi^+$ events with optimized cuts, as a function of fragmentation parameterization. Errors are statistical only.

and the largest variation for $B_c^+ \rightarrow J/\psi\pi^+\pi^-\pi^+$ is 0.05%. Both of these are completely negligible and consistent with the nominal efficiency. Thus, no systematic uncertainty is assigned for the fragmentation parameterization.

⁴⁶Here I use the HQET quark masses instead of the conventional pole mass or running mass.

| <i>Fragmentation Function</i> | $\epsilon_{3\pi}$ |
|---|----------------------|
| B_c Frag. ($R = 0.25$) (default) | $(2.38 \pm 0.10) \%$ |
| B_c Frag. ($R = 0.196$) | $(2.43 \pm 0.10) \%$ |
| Peterson ($\epsilon_P = 0.09$) | $(2.36 \pm 0.09) \%$ |

Table 15: Efficiency of $B_c^+ \rightarrow J/\psi \pi^+ \pi^- \pi^+$ events with optimized cuts, as a function of the fragmentation parameterization. Errors are statistical only.

5.5 Decay-in-Flight Correction

In the generated Monte Carlo samples, the daughter π and K mesons from B decay are modeled as stable particles to provide an idealized set of events from which the geometric and kinematic acceptances can be extracted. The physical particles do have a finite lifetime, however, and a fraction of the pions and kaons from B decay will themselves decay within the tracking volume. To estimate an upper bound on the effect that these “decays-in-flight” have on the $\sigma \cdot \mathcal{B}$ ratio, one may conservatively assume that 100% of the particles that decay before traversing the entire tracking volume will fail the pattern recognition (or alternatively, that the components of the error matrix of the track and the calculated residuals become so large that the event fails the χ^2_{2d} probability cut.) The lifetime of the π meson is $(2.6033 \pm 0.0005) \times 10^{-8}$ s, [7, p.27] and that of the K meson is $(1.2386 \pm 0.0024) \times 10^{-8}$ s. [7, p. 32] The fraction of mesons that remain undecayed after traversing the tracking volume is

$$\frac{N_{\pi,k}(\text{undecayed})}{N_{\pi,K}(\text{total})} = \exp\left(-\frac{L_{CTC} M_{\pi,K}}{P_T c\tau_{\pi,K}}\right), \quad (5.1)$$

where L_{CTC} is the length (in the transverse plane) of the particle trajectory, M is the pion or kaon mass in GeV, and $c\tau$ is the velocity of light times the

lifetime. For $P_T > 1$ GeV, the helical path length differs from a straight line by < 2 cm in the transverse plane, so that Equation 5.1 becomes

$$\frac{N_{\pi,k}(\text{undecayed})}{N_{\pi,K}(\text{total})} \approx \exp\left(-\frac{R_{CTC} M_{\pi,K}}{P_T c\tau_{\pi,K}}\right). \quad (5.2)$$

The outer radius of the CTC is 1.32 m. Weighting the momentum distribution for pions and kaons from B decay by the inverse of Equation 5.2 provides an upper bound on the total number of events produced, of which only the undecayed fraction is assumed to be observable. Figure 45 shows both the weighted and unweighted P_T^K distributions for a Monte Carlo sample of $B^+ \rightarrow J/\psi K^+$ events which pass the cuts optimized for the statistical significance of the $B^+ \rightarrow J/\psi K^+$ signal in the data. The weighted P_T^K distribution contains $(9.80 \pm 0.23)\%$ more events than the unweighted sample (error is due to Monte Carlo statistics only). Figure 45 also compares the P_T^π distributions for weighted and unweighted Monte Carlo $B_c^+ \rightarrow J/\psi \pi^+$ events which pass the cuts optimized for the significance of the Monte Carlo $B_c^+ \rightarrow J/\psi \pi^+$ signal with background determined from data (the “ x_S cuts.”) The weighted P_T^π distribution contains $(1.16 \pm 0.13)\%$ more events than the unweighted sample. Clearly, the shorter K lifetime ensures that, to the extent that the P_T distributions are similar, a larger fraction of kaon daughters from B^+ will decay in the tracking volume than pion daughters from B_c .

These numbers are upper bounds only on the size of the effect. Charged particles that decay inside the CTC will be reconstructed with a finite, non-zero efficiency which depends on the track momenta, the presence of additional tracks in the event, and the distance that the particles travel before decay. Since the B_c decay channels are normalized to the $B^+ \rightarrow J/\psi K^+$ decay, a decrease in the $B^+ \rightarrow J/\psi K^+$ detection efficiency of 9.8% would result in a corresponding decrease in the upper limit of $\sigma \cdot \mathcal{B}$. Conservatively, one should

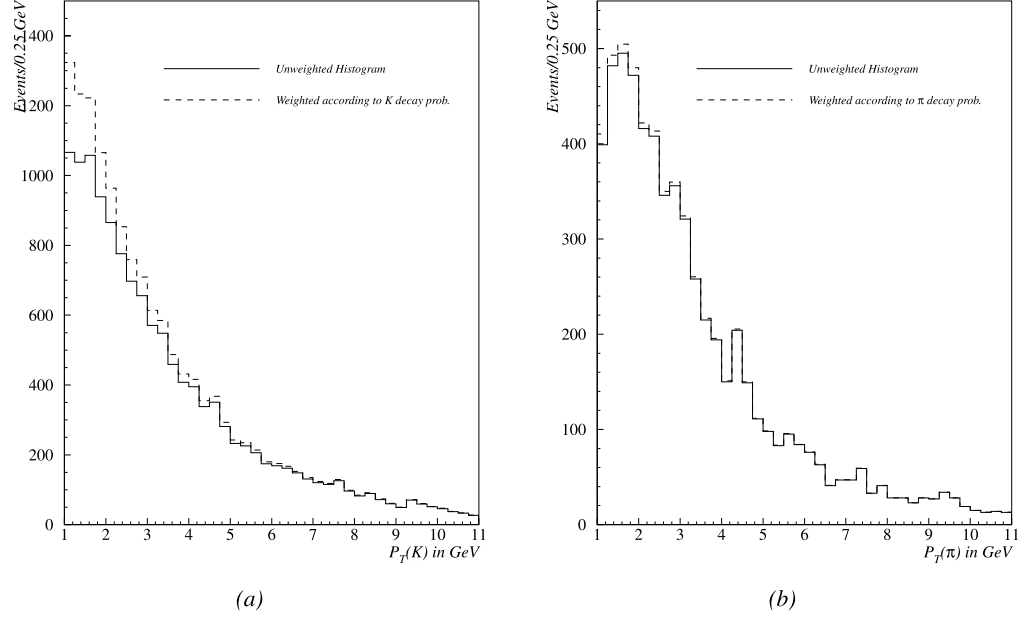


Figure 45: (a) Unweighted (solid) and weighted (dashed) P_T^K histograms for Monte Carlo $B^+ \rightarrow J/\psi K^+$ events passing optimized cuts. (b) Unweighted (solid) and weighted (dashed) P_T^π histograms for Monte Carlo $B_c^+ \rightarrow J/\psi \pi^+$ events passing optimized cuts. Weighted histograms indicate maximum total number of events (decayed + undecayed), assuming that all particles that decay within the tracking volume are undetected.

neglect the kaon decays-in-flight and consider only the pion decays, which will increase the limit. The true value for the single-pion efficiency correction lies somewhere between 0.0% and -1.16% . For the three-pion case, the maximum correction is $(1 - 0.0116)^3 - 1 = 0.9656 - 1 = -3.44\%$ of the nominal three-pion efficiency. In calculating the final efficiency for $B_c^+ \rightarrow J/\psi\pi^+$, I apply a correction of 0.994, with a systematic uncertainty of 0.006.⁴⁷ For $B_c^+ \rightarrow J/\psi\pi^+\pi^-\pi^+$, the correction is 0.983 with a systematic uncertainty of 0.017. The correction to the kaon efficiency is conservatively taken to be 0%.

5.6 Tracking Efficiency Correction

In calculating the relative detection efficiencies of $B_c^+ \rightarrow J/\psi\pi^+$ and $B^+ \rightarrow J/\psi K^+$ events using Monte Carlo samples, many common acceptance factors cancel in the ratio. In the measurement of other $\sigma\mathcal{B}$ ratios of B decays at CDF, however, it has been observed [61] that there is a residual tracking efficiency which does not cancel when comparing decays involving pion tracks to decays involving kaon tracks. While the origin of such a residual tracking efficiency is not well understood, there are a number of factors that contribute to the degradation of the overall tracking performance during Run I. Most notably, the instantaneous luminosity increased by roughly a factor of 10 in Run Ib. Higher luminosity results in a larger number of primary vertices per event and a larger track multiplicity in each event. Additionally, the gas quality in the tracking volume degraded over time, becoming a more pronounced source of tracking inefficiency.

In Warburton's study, [61] Monte Carlo-generated pion tracks from

⁴⁷This contribution is negligible when combined with other sources of uncertainty, such as the B_c lifetime, but is nonetheless included in the calculation for completeness.

the decay $B^+ \rightarrow J/\psi(2S)K^+$; $J/\psi(2S) \rightarrow \pi^+\pi^-$ were embedded into the $B^+ \rightarrow J/\psi K^+$ candidate events from the raw data and reconstructed using the full CDF tracking software to determine the necessary corrections to the relative efficiency of pattern recognition, as a function of track multiplicity, instantaneous luminosity, and primary vertex multiplicity. It was determined that the primary contributing factor to CTC tracking inefficiency was the occupancy, particularly of the inner superlayers, during periods of high luminosity. He also concluded that pattern recognition efficiencies of two-pion tracks in an event were correlated, but that the correlation became insignificant when systematic uncertainties were included. The relevant results of Warburton's study which I apply to this analysis are the aggregate single-track efficiency, 0.928 ± 0.020 (valid for $P_T(\text{track}) > 0.4$ GeV), and the double-track efficiency, 0.881 ± 0.043 ($P_T > 0.4$ GeV). For the $B_c^+ \rightarrow J/\psi \pi^+ \pi^- \pi^+$ channel, I note that the correlation is in fact small.⁴⁸ By combining the single-track and double-track efficiencies (assuming no correlation) a “triple-track” efficiency of 0.818 ± 0.044 is derived. These corrections are applied to the corresponding acceptance efficiencies calculated via Monte Carlo. The uncertainties are used in calculating the final limit on $\sigma \cdot \mathcal{B}$ as the systematic uncertainty due to the tracking efficiency.

⁴⁸ $\sqrt{0.881} = 0.939$ is the same as the single-track efficiency within the quoted uncertainty.

Chapter 6

Results and Conclusions

6.1 Introduction

Given the number of observed events in each mass bin, the corrected Monte Carlo efficiencies with their associated uncertainties, and the distribution of background events outside the bin, it is now possible to set an upper limit on the cross section times branching fraction ratio for the B_c decay channels. The framework currently endorsed by the PDG [7, p. 200-201] for constructing a confidence interval that obeys “coverage” properties is not compatible with the general case of setting an upper limit on a small-signal (Poisson-distributed) sample with known background and additional sources of uncertainty. The calculation of upper limits used here is described in greater detail in Appendix A. The basis of this method is that each term in the ratio: $z = \frac{N_{B_c} \epsilon_{B^+}}{N_{B^+} \epsilon_{B_c}}$ ⁴⁹ can be considered to be distributed according to its own probability density function (pdf). Integrating an appropriate combination of these pdf’s allows for a limit to be determined on the combined ratio rather than on the number of B_c events alone.

6.2 $B_c^+ \rightarrow J/\psi \pi^+$ Upper Limits

For this calculation, the pdf’s for each of the $\sigma \cdot \mathcal{B}$ terms are as follows:

$$f_{B^+}(x) = \frac{1}{\sqrt{2\pi}\sigma_{N(B^+)}} \exp \left(- \left(\frac{x - N(B^+)}{\sqrt{2}\sigma_{N(B^+)}} \right)^2 \right),$$

⁴⁹After cancellation of the integrated luminosity and common detector efficiency factors, this ratio is equivalent to the ratio $\frac{\sigma(B_c) \cdot \mathcal{B}(B_c^+ \rightarrow J/\psi \pi^+)}{\sigma(B^+) \cdot \mathcal{B}(B^+ \rightarrow J/\psi K^+)}$.

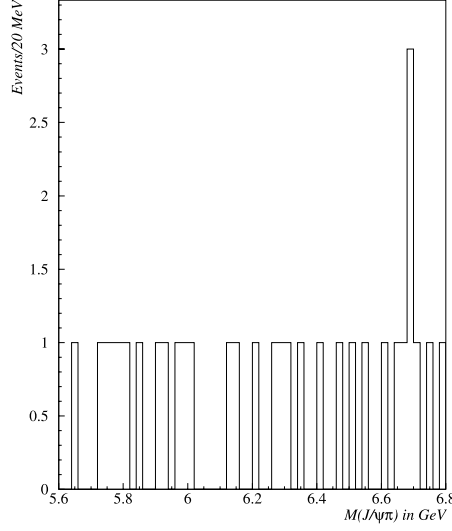


Figure 46: $J/\psi\pi^+$ invariant mass distribution with the optimized selection cuts.

$$\begin{aligned}
 f_{B_c}(n; x + B) &= \frac{1}{n!} e^{-(x+B)} (x+B)^n, \\
 E_{B^+}(x) &= \frac{1}{\sqrt{2\pi}\sigma_{\epsilon(B^+)}} \exp\left(-\left(\frac{x - \epsilon(B^+)}{\sqrt{2}\sigma_{\epsilon(B^+)}}\right)^2\right), \\
 E_{B_c}(x) &= \frac{1}{\sqrt{2\pi}\sigma_{\epsilon(B_c)}} \exp\left(-\left(\frac{x - \epsilon(B_c)}{\sqrt{2}\sigma_{\epsilon(B_c)}}\right)^2\right).
 \end{aligned} \tag{6.1}$$

The number of $B^+ \rightarrow J/\psi K^+$ events, $N(B^+)$, and its uncertainty $\sigma_{N(B^+)}$ are 450 and 23 respectively (from Table 7). The background N_{bg} (taken with negligible uncertainty due to the higher sideband statistics⁵⁰) and number of $B_c^+ \rightarrow J/\psi\pi^+$ events N_π are determined for each mass bin by the mass plot reproduced in Figure 46. The $B^+ \rightarrow J/\psi K^+$ Monte Carlo efficiency ϵ_{B^+}

⁵⁰Uncertainties on the background estimate could be included by performing an additional integration via Equation A.11, the final upper limit calculation varies by less than 2% when this is included. For clarity and simplicity, I have omitted this source of uncertainty.

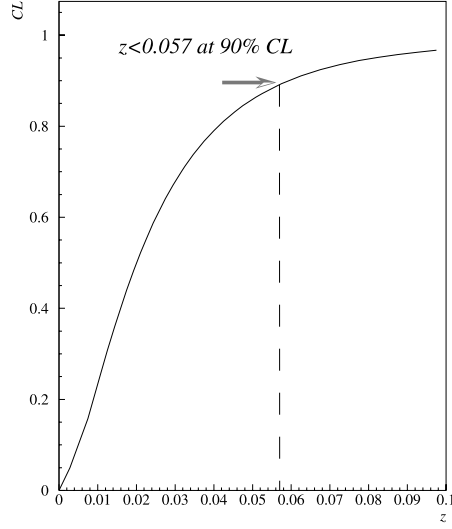


Figure 47: Calculation of the upper limit for the $B_c^+ \rightarrow J/\psi\pi^+$ decay with $M(B_c) = 6.2$ GeV. Horizontal axis indicates $\sigma \cdot \mathcal{B}$ ratio z and vertical axis represents the value of the integral over the combined pdf of Equation A.14. The arrow indicates 90% CL limit, corresponding to a limit on $\sigma \cdot \mathcal{B}$ of 0.057.

and uncertainty $\sigma_{\epsilon(B^+)}$ is $14.18 \pm 0.13\%$ (statistical uncertainty only) from Table 7. The $B_c^+ \rightarrow J/\psi\pi^+$ Monte Carlo efficiency ϵ_π and its uncertainty $\sigma_{\epsilon(\pi)}$ are collected in Table 16. The efficiencies include decay-in-flight and tracking corrections. The uncertainties are the Monte Carlo statistics combined in quadrature with the decay-in-flight, tracking, and lifetime systematic uncertainties in this table. The final column of Table 16 contains the upper limit (at 90% confidence level) on the ratio $\frac{\sigma(B_c) \cdot \mathcal{B}(B_c^+ \rightarrow J/\psi\pi^+)}{\sigma(B^+) \cdot \mathcal{B}(B^+ \rightarrow J/\psi K^+)}$ calculated using Equations A.14 and A.15 described in Appendix A. The lifetime systematic dominates the uncertainty. Figure 47 displays a sample curve of the integration involved in calculating the upper limit for the $B_c^+ \rightarrow J/\psi\pi^+$ decay with an input mass of 6.2 GeV for B_c .

| M_{B_c} | ϵ_π | N_π | N_{bg} | z (90% CL) |
|-----------|----------------------|---------|----------|--------------|
| 5.6 | $(3.02 \pm 1.10) \%$ | 1 | 2.82 | 0.033 |
| 5.7 | $(2.96 \pm 1.10) \%$ | 4 | 2.55 | 0.070 |
| 5.8 | $(3.00 \pm 1.10) \%$ | 2 | 2.73 | 0.042 |
| 5.9 | $(2.97 \pm 1.10) \%$ | 4 | 2.55 | 0.069 |
| 6.0 | $(2.93 \pm 1.10) \%$ | 1 | 2.82 | 0.035 |
| 6.1 | $(2.94 \pm 1.10) \%$ | 2 | 2.73 | 0.044 |
| 6.2 | $(2.89 \pm 1.10) \%$ | 3 | 2.64 | 0.057 |
| 6.3 | $(2.88 \pm 1.10) \%$ | 2 | 2.73 | 0.045 |
| 6.4 | $(2.85 \pm 1.10) \%$ | 2 | 2.73 | 0.045 |
| 6.5 | $(2.87 \pm 1.10) \%$ | 2 | 2.73 | 0.045 |
| 6.6 | $(2.84 \pm 1.10) \%$ | 6 | 2.36 | 0.112 |
| 6.7 | $(2.79 \pm 1.10) \%$ | 3 | 2.64 | 0.060 |

Table 16: Corrected Monte Carlo efficiency ϵ_π with total uncertainty (statistical and systematic), number of $B_c^+ \rightarrow J/\psi\pi^+$ events in each bin N_π , background (average of remaining bins) N_{bg} , and calculated upper limit at 90% CL on z .

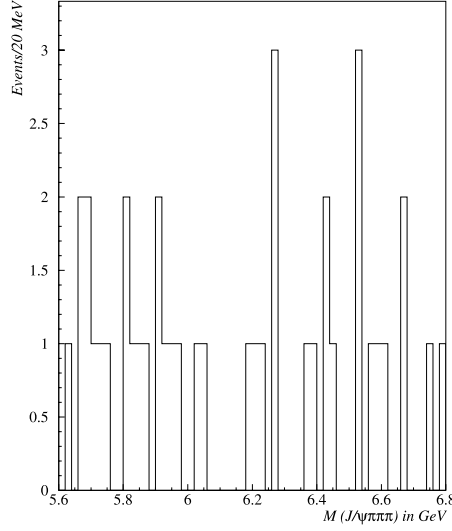


Figure 48: $J/\psi\pi^+\pi^-\pi^+$ invariant mass distribution.

6.3 $B_c^+ \rightarrow J/\psi\pi^+\pi^-\pi^+$ Upper Limits

Proceeding in the same fashion for $B_c^+ \rightarrow J/\psi\pi^+\pi^-\pi^+$, the pdf's for each of the terms in z are identical to those of Equation 6.1.

The number of $B^+ \rightarrow J/\psi K^+$ events and Monte Carlo efficiency are the same as for the $J/\psi\pi^+$ sample. The background N_{bg} (taken with negligible uncertainty) and number of $J/\psi\pi^+\pi^-\pi^+$ events $N_{3\pi}$ are determined for each mass bin from Figure 48. The Monte Carlo efficiency $\epsilon_{3\pi}$ for $B_c^+ \rightarrow J/\psi\pi^+\pi^-\pi^+$ and its uncertainty $\sigma_{\epsilon(3\pi)}$ are collected in Table 17. The efficiencies include decay-in-flight and tracking corrections. The uncertainties come from the Monte Carlo statistics combined in quadrature with the decay-in-flight, tracking, and lifetime systematic uncertainties in this table. The final column of Table 17 contains the upper limit at 90% confidence level on the ratio $z = \frac{\sigma(B_c) \cdot \mathcal{B}(B_c^+ \rightarrow J/\psi\pi^+\pi^-\pi^+)}{\sigma(B^+) \cdot \mathcal{B}(B^+ \rightarrow J/\psi K^+)}$ calculated using the method described in Appendix A. The systematic in the lifetime dominates the uncertainty.

| M_{B_c} | $\epsilon_{3\pi}$ | $N_{3\pi}$ | N_{bg} | z (90% CL) |
|-----------|----------------------|------------|----------|--------------|
| 5.6 | $(1.48 \pm 0.92) \%$ | 5 | 3.27 | 0.196 |
| 5.7 | $(1.51 \pm 0.92) \%$ | 3 | 3.45 | 0.121 |
| 5.8 | $(1.54 \pm 0.93) \%$ | 5 | 3.27 | 0.187 |
| 5.9 | $(1.70 \pm 0.93) \%$ | 5 | 3.27 | 0.162 |
| 6.0 | $(1.80 \pm 0.93) \%$ | 2 | 3.54 | 0.076 |
| 6.1 | $(1.83 \pm 0.93) \%$ | 1 | 3.63 | 0.061 |
| 6.2 | $(1.91 \pm 0.93) \%$ | 5 | 3.27 | 0.136 |
| 6.3 | $(2.00 \pm 0.93) \%$ | 2 | 3.54 | 0.066 |
| 6.4 | $(1.99 \pm 0.93) \%$ | 3 | 3.45 | 0.082 |
| 6.5 | $(1.98 \pm 0.93) \%$ | 5 | 3.27 | 0.129 |
| 6.6 | $(2.01 \pm 0.93) \%$ | 3 | 3.45 | 0.081 |
| 6.7 | $(2.03 \pm 0.93) \%$ | 2 | 3.54 | 0.064 |

Table 17: Corrected Monte Carlo efficiency $\epsilon_{3\pi}$ with total uncertainty (statistical and systematic), number of $B_c^+ \rightarrow J/\psi \pi^+ \pi^- \pi^+$ events in each bin $N_{3\pi}$, background (average of remaining bins) N_{bg} , and calculated upper limit at 90% CL on z .

6.4 Conclusions

By reconstructing events containing a J/ψ displaced from its production vertex and additional tracks, I search for the decays $B_c^+ \rightarrow J/\psi\pi^+$ and $B_c^+ \rightarrow J/\psi\pi^+\pi^-\pi^+$ in the CDF experiment at Fermilab. No statistically significant excess of events in the invariant mass spectrum is observed. An upper limit on the cross section times branching fraction (relative to $B^+ \rightarrow J/\psi K^+$ decays) for these decays in $p\bar{p}$ collisions at 1.8 TeV is determined. This upper limit is expressed as a function of the B_c mass, which is not yet determined. The $\sigma \cdot \mathcal{B}$ ratio limits can be compared to the PDG limits by multiplying by the $b \rightarrow B^+$ and $B^+ \rightarrow J/\psi K^+$ branching fractions: [7, p. 44, 40]

$$\mathcal{B}(b \rightarrow B^+) = (38.9 \pm 1.3)\%; \quad \mathcal{B}(B^+ \rightarrow J/\psi K^+) = (10.0 \pm 1.0) \times 10^{-4}. \quad (6.2)$$

Applying these values to the bin in each mass distribution with the largest limit gives the following maximum upper limits:

$$\frac{\Gamma(B_c^+ \rightarrow J/\psi\pi^+)}{\Gamma(B_c \rightarrow X)} \times \mathcal{B}(\bar{b} \rightarrow B_c) < 4.4 \times 10^{-5} (90\% \text{CL}) \quad (6.3)$$

$$\frac{\Gamma(B_c^+ \rightarrow J/\psi\pi^+\pi^-\pi^+)}{\Gamma(B_c \rightarrow X)} \times \mathcal{B}(\bar{b} \rightarrow B_c) < 7.6 \times 10^{-5} (90\% \text{CL}). \quad (6.4)$$

These can be compared with the current PDG limits:

$$\frac{\Gamma(B_c^+ \rightarrow J/\psi\pi^+)}{\Gamma(B_c \rightarrow X)} \times \mathcal{B}(\bar{b} \rightarrow B_c) < 8.2 \times 10^{-5} (90\% \text{CL}) \quad (6.5)$$

$$\frac{\Gamma(B_c^+ \rightarrow J/\psi\pi^+\pi^-\pi^+)}{\Gamma(B_c \rightarrow X)} \times \mathcal{B}(\bar{b} \rightarrow B_c) < 5.7 \times 10^{-4} (90\% \text{CL}). \quad (6.6)$$

In Run II of the Tevatron⁵¹, CDF should see an accumulation of 2 fb⁻¹ of data (an increase of ~ 20 over the present statistics), observation of hadronic decays of the B_c is assured. The upgraded silicon vertex detector and tracking

⁵¹slated to begin in March, 2001

system will allow for a precise determination of the B_c mass and lifetime. Measurement of the hadronic decay fractions of the B_c will open up a new tool for understanding the QCD dynamics of heavy quark systems. Heavy quark physics will play a critical role in the next generation high-energy physics program as the Higgs boson is either discovered or the Standard Model is modified to accomodate its absence.

Appendix A

Incorporation of Errors Into Branching Ratio Limit

A.1 Introduction

The problem of determining an upper limit, with a specified significance level, of a small number of events in a multi-channel spectrum is frequently encountered in the study of rare decays and in searches for new particles. In determining limits on compound quantities, such as the ratio $z = \frac{\sigma(B_c)\mathcal{B}(B_c \rightarrow J/\psi \ X)}{\sigma(B_u^+)\mathcal{B}(B_u^+ \rightarrow J/\psi \ K^+)}$, care must be taken not only to include the effects of background uncertainty on the number of B_c candidate events observed in the data, but also to include the uncertainty in the number of observed B^+ events (as well as systematic uncertainties in the detection efficiencies). The following is a method of modifying the probability distribution functions in such a way that allows the calculation of an upper limit on the combined quantities, with their various sources of uncertainty, that is valid under the same interpretation of confidence intervals as the more familiar small-signal particle searches. The traditional method is to construct a likelihood function from the Poisson probability with known background, smear it according to estimated uncertainties, and use the convolved likelihood function to produce a confidence interval. This method is not generally consistent with the meaning of a confidence interval as it is usually applied to a system with negligible sources of uncertainty.

Many points of view regarding the appropriate mathematical and philosophical frameworks that physicists should employ in solving problems of this nature have been expressed. [63, 64, 65] In addition to the well-known statistical methods of Bayesian and frequentist confidence intervals, the PDG

currently favors a more baroque approach based on frequentism, but with an emphasis on setting limits which cover the “true” value of a measured parameter. [66] There also exists a Bayesian analog of the same method. [67] Such attempts to construct a statistically sound methodology free of the taint of subjectivity⁵² invariably result in a numerical answer, the significance of which is not easily translated into human language; there is no simple interpretation that one can understand without the benefit of several paragraphs of text describing the numerical result. An answer that is not readily apprehended is of dubious value to most researchers. In any event, upper limits calculated using these optimum coverage methods have so far only been applied to cases involving precisely known backgrounds and no additional sources of error. It is therefore desirable to develop a means of introducing error terms into the conventional confidence interval method for small signals with background. Where appropriate and significant in the following sections, the mode of reasoning (Bayes v. frequentist) will be explicitly stated.

Prior to 1997, the PDG [68] recommended a specific method for setting an upper limit on a quantity distributed according to Poisson statistics with a known background contribution:

$$1 - \alpha = 1 - \frac{e^{-(\mu_B + N)} \sum_{n=0}^{n_0} \frac{(\mu_B + N)^n}{n!}}{e^{-\mu_B} \sum_{n=0}^{n_0} \frac{\mu_B^n}{n!}}, \quad (\text{A.1})$$

where α is the desired confidence level, μ_B is the mean of the background contribution, N is the number of peak events, and n_0 is the number of events

⁵²I would argue that pure objectivity is neither a practically realizable nor a desirable goal for any scientific endeavor. Subjectivity is an intrinsic component of every analysis. Indeed, the very term “confidence interval” implies a quantifiable “degree of belief.” I adopt a hybrid view that combines frequentist methodology with the intuitive understanding most physicists have regarding Bayesian results.

actually observed. It is useful and instructive at this point to examine the derivation of this probability distribution in order to discern how it may be generalized to include additional sources of error and additional multiplicative terms that are themselves distributed according to sets of assumed probability distributions.

A.2 Peak Area Probability Distribution

If there are N events in the peak of a distribution with B background events, the Poisson probability of observing n events in the same region is:

$$P(n) = \frac{e^{-(B+N)}(B+N)^n}{n!}. \quad (\text{A.2})$$

Here, N and B are taken to be the parameters of the probability function $P(n)$ determining the probability of finding n events (n is a discrete variable here) in a set of bins. This interpretation of the probability is correct if N and B are the “true” values of the signal and background. We are interested, however, in the inverse problem. Given B , the predicted number of background events based on Monte Carlo or theory, and n , the total number of observed events in the region of interest actually found by the experiment, we wish to know the distribution of the number of peak events, N . In a Bayesian approach to this problem, one assumes a prior probability distribution function⁵³ of the unknown parameter and then performs an experiment to update this prior distribution. The choice of the prior pdf is based on information available to the experimenter before the experiment is performed to avoid biasing the

⁵³Referenced hereafter as “pdf,” which should not be confused with the earlier introduced abbreviation for “parton distribution function.”

interpretation of the results of the experiment.⁵⁴ The updated distribution is then known as the posterior pdf of the experiment and may be used to infer the likelihood of the actual value of the unknown parameter. This process of updating the pdf is accomplished via Bayes' Rule. If one assumes the background is known precisely, the only unknown parameter is the signal rate, N . Bayes' Rule can then be formulated as:

$$g(N; n) = \frac{f(n; N)g(N)}{\int_0^\infty f(n; N')g(N')dN'}, \quad (\text{A.3})$$

where $f(n; N)$ is the conditional probability to observe n events, given the signal rate N , $g(N)$ is the prior pdf, and $g(N; n)$ is the conditional posterior pdf of N , given n observed events. The upper level estimate N_α for confidence level α is then obtained by integrating this posterior pdf:

$$1 - \alpha = \int_0^{N_\alpha} g(N'; n)dN'. \quad (\text{A.4})$$

The key element at this stage is the choice of the prior distribution. There exists a variety of conflicting opinions on what constitutes a valid prior pdf. Faced with such a lack of consensus among statisticians and experimenters alike, it is at this point that many choose to abandon the Bayesian approach altogether and fall back on the classical frequentist approach. High-energy physicists generally opt for a non-informative prior (*i.e.*, one which does not rely on results of previous experiments on the grounds that the experiment can not thereafter be independent of those previous experiments and the results can not be combined). As the subject of this thesis is an independent evaluation of limits and the first such experiment by this author, there is little

⁵⁴Strict frequentists generally refer to this as the “subjective” prior, in the pejorative sense. Priors are rarely chosen in a wholly arbitrary fashion, however, and should properly reflect one’s knowledge of the allowed values of the parameter, or lack thereof.

danger in following this precedent. I will also follow precedent established by other new particle searches in assuming that the choice of a non-informative prior should be a flat distribution in N , ranging from 0 to ∞ . In this case, substituting the Poisson probability for $f(n; N)$

$$f(n; N) = e^{-(N+B)} \frac{(N+B)^n}{n!} \quad (\text{A.5})$$

and applying Bayes' Rule produces a posterior which is comfortably familiar:

$$g(N) = \frac{e^{-(N+B)} (N+B)^n}{n!}. \quad (\text{A.6})$$

It should be noted that the choice of a flat distribution in N , while seemingly innocuous, actually hides many dangers. One obvious objection is that if one can choose a flat distribution of an unknown parameter, then one can equally choose a flat distribution of any function of this unknown parameter. Since I am setting a limit (at least for now) on N , the natural choice is to choose N itself as the function assumed to be flat. Others have argued somewhat more rigorously that a valid non-informative prior pdf must obey certain transformational properties or be constructed so that the posterior distribution exhibits certain limit properties. One popular choice of a non-informative prior for a Poisson statistic is proportional to $1/N$, despite the provable result that this can lead to an upper limit on small signal searches that is well below the resolution of the detector. [65] While mindful of such arbitrariness in selecting non-informative priors, I again defer to precedents set by other high-energy physics analyses in the choice of a flat distribution in N .

A.3 Poisson Signals With Background Contribution

In using the Poisson distribution for $(N+B)$ in the preceding section, I have omitted a subtle point, which becomes significant for searches in a region

where no peak is evident. I have assumed that the probability for observing n events, given N average signal events and B background events, is the product of the Poisson probabilities in N and B individually, and summed over all combinations that add up to n : [69]

$$f(n; N + B) = \sum_{n_b=0}^n f(n_b; B) f(n - n_b; N), \quad (\text{A.7})$$

which reduces to equation A.5. This relation is inappropriate for calculating a limit on N , however, as it allows for the possibility of a negative (hence unphysical) limit on the true number of signal events. If we have measured n events in the data and expect B background events, $f(n_b; B)$ must be renormalized to account for the fact that n_b can not take on values larger than n :

$$f'(n_b; B) = \frac{f(n_b; B)}{\sum_{n_b=0}^n f(n_b; B)}. \quad (\text{A.8})$$

The product of the individual probabilities then becomes

$$f'(n; N + B) = \frac{f(n; N + B)}{\sum_{n_b=0}^n f(n_b; B)}. \quad (\text{A.9})$$

The α confidence level upper limit on N can now be determined by repeatedly integrating by parts to obtain the sum:

$$1 - \alpha = 1 - \frac{\sum_{n_a=0}^n f(n_a; N_\alpha + B)}{\sum_{n_b=0}^n f(n_b; B)}, \quad (\text{A.10})$$

which is the same form as the expression in Equation A.1. Errors on the background estimate B can be incorporated by integrating over the assumed background distribution $g(b)$:

$$1 - \alpha = 1 - \frac{\sum_{n_a=0}^n \int_0^\infty g(b) f(n_a; N_\alpha + b) db}{\sum_{n_b=0}^n \int_0^\infty g(b) f(n_b; b) db}. \quad (\text{A.11})$$

A.4 Generalization of Upper Limit

So far, I have merely demonstrated the principles involved in one possible derivation of the “old” PDG-prescribed method for calculating the upper limit on a Poisson process with background. It is necessary now to generalize this to encompass additional multiplicative terms (the selection efficiencies and number of observed $B^+ \rightarrow J/\psi K^+$ events) with their own sources of error. Suppose I have two distributions in two different unknown variables, $p(x)$ and $q(y)$. I wish to know the probability distribution $r(z)$ of the combined quantity $z = xy$. This can be accomplished for a given z by integrating over all intermediate values of the arguments of p and q such that the product of those arguments remains constant and equal to z :

$$r(z) = \int_{-\infty}^{+\infty} p(x)q(z/x)\frac{1}{x}dx. \quad (\text{A.12})$$

Likewise, if z represents the ratio, rather than the product, of x and y , the combined probability $s(z)$ is:

$$s(z) = \int_{-\infty}^{+\infty} p(xz)q(x)xdx. \quad (\text{A.13})$$

The factors $\frac{1}{x}$ and x in these two equations are the Jacobian factors of the variable transformations and maintain the normalization of the combined probability distributions.

A.5 Inclusion of Systematic Errors in Final Limit Calculation

In calculating the preliminary upper limits on the $\sigma \cdot \mathcal{B}$ ratio in the cut optimization procedure, the selection efficiencies were taken to be known precisely. If instead, one assumes that the efficiency terms are distributed according to

a Gaussian, with a mean given by the nominal value and width determined by combining the systematic shifts in quadrature, Equations A.12 and A.13 can be used to construct a new probability distribution function. The combined pdf of the final ratio $z = \frac{N_{B_c} \epsilon_{B^+}}{N_{B^+} \epsilon_{B_c}}$ can then be expressed as:

$$g(n; z) = \int_{y=0}^{\infty} \int_{x=0}^{\infty} \int_{N'=0}^{\infty} f_{B_c}(n; N'x+B) f_{B^+}(N') E_{B^+}(yz/x) E_{B_c}(y) \frac{N'y}{x} dN' dx dy, \quad (\text{A.14})$$

where $f_{B_c}(n; N'x+B)$ is the probability distribution for finding n or fewer events in the data with expected background contribution B and $N'x$ B_c signal events, as given by Equation A.5; $f_{B^+}(N')$ is a Gaussian distribution in the number of observed B^+ events N' with mean and width determined by a fit to the $J/\psi K^+$ mass spectrum; and $E_i(q)$ is the efficiency distribution with the nominal mean efficiency ϵ_i for each decay channel i and width determined by summing uncertainties in quadrature. I have also switched⁵⁵ from a Bayesian interpretation of $f_{B_c}(n; N'x+B)$ to a frequentist one in order to make the number of signal events n an explicit variable instead of an implicit one. By assuming that the systematic errors can be folded into the efficiency distributions and combined with the original pdf for the observed number of events, I have in fact already shifted the interpretation to a frequentist view by assuming that this is an estimation of the “true” value of z . The new interpretation is that $g(n; z)$ represents the probability of measuring the $\sigma \cdot \mathcal{B}$ ratio z , given the number of observed events n in the B_c decay mode. The background

⁵⁵à la. [69] The PDG96 method for calculating upper limits on Poisson process with background is only Bayesian on the surface. The underlying assumptions that allow one to use Bayes’ Rule to calculate confidence intervals are essentially frequentist. If a constant prior is used, one obtains results consistent with the frequentist approach if one blindly follows the Bayesian prescription without being unduly rigorous about the interpretation of the pdfs and the result.

normalization term in Equation A.9 has been implicitly absorbed in taking the positive integration path over $N'x$. Strictly speaking, there should be similar renormalization terms in the denominator of Equation A.14 to prevent the efficiencies and number of B^+ events from fluctuating to non-physical negative values. The means of these distributions are significantly large (> 5 standard deviations in all cases) that such correction factors contribute negligibly to the integrals. The normalization of the truncated distributions is handled by integration (the denominator in Equation A.15 below), which improves the readability of the integral equation A.14.

The upper limit on the ratio z can now be obtained by integration:

$$1 - \alpha = 1 - \frac{\int_0^{z_\alpha} g(n; z) dz}{\int_0^\infty g(n; z) dz}. \quad (\text{A.15})$$

The interpretation of the confidence level limit obtained in this fashion is that in the limit of an infinite number of measurements of z , the frequency with which one obtains a $\sigma \cdot \mathcal{B}$ ratio of no more than z_α is α .

A.6 Numerical Methods and Evaluation of Accuracy

The multiple integrations in Equations A.14 and A.15 are carried out by recursively calling a one-dimensional integration routine based on the method of Gaussian quadratures. [70, 71, 72, pp. 147-156] This method was chosen because it has faster convergence properties than other means of multi-dimensional integration (*e.g.*, Monte Carlo integration). The principle underlying Gaussian quadratures is that given prior knowledge about the functional form of an integrand, one may find a set of weights and abscissas at which to evaluate the integrand which greatly improves the accuracy of the integration with a smaller number of function evaluations than other numerical methods.

A remarkable feature of Gaussian quadrature is that the integral becomes exact for classes of integrands that are polynomials times a function $W(x)$, where the form of $W(x)$ dictates how the abscissas and weights are to be calculated. Given $W(x)$ and an integer N (the number of function evaluations), the set of abscissas x_j and weights w_j can be calculated such that the approximation:

$$\int_a^b W(x)f(x)dx \approx \sum_{j=1}^N w_j f(x_j) \quad (\text{A.16})$$

becomes exact if $f(x)$ is a polynomial of order $2N-1$ or less. In Equation A.14, $W(x)$ can be chosen to be Gaussian ($W(x) = \exp^{-x^2}$) for the N' and y integrations and $W(x) = x^\alpha \exp^{-x}$ for the N' integration.⁵⁶ With these choices for $W(x)$, the weights are determined by

$$w_j = \frac{\langle p_{N-1} | p_{N-1} \rangle}{p_{N-1}(x_j) p'_N(x_j)}, \quad (\text{A.17})$$

where $p'_N(x_j)$ is the derivative of the orthogonal⁵⁷ polynomial p_N evaluated at its root x_j and the scalar product $\langle p_n | p_m \rangle$ is defined as:

$$\langle f | g \rangle = \int_a^b W(x) f(x) g(x) dx. \quad (\text{A.18})$$

For the Gaussian case with indefinite limits, the p_N are the Hermite polynomials; for the Poisson integration, the p_N are the Laguerre polynomials. In calculating the confidence limit by integrating over z , $W(x) = 1$ and the p_N are the Legendre polynomials. In all cases, the roots of the polynomials are found by iteration via Newton's Method, [73] and derivatives are obtained analytically from recurrence relations involving lower-order polynomials to eliminate

⁵⁶In fact, the integration over y is carried out analytically, but gives the same result as the Gaussian quadrature integration of order $N = 1$, since $f(x)$ is a constant (with an appropriate change of variables).

⁵⁷In the sense of scalar products defined by Equation A.18.

sources of error due to numerical differentiation. The order of the orthogonal polynomials in each integral is determined by starting at $N = 1$ and incrementing until the fractional difference between successive iterations is less than the desired accuracy.

Solving Equation A.15 for z_α requires a root-finding algorithm in conjunction with the integrating routine. For this purpose, I chose a method developed by Brent [74] which guarantees at least linear convergence for functions known to contain a root within the initially selected interval.

In order to test the implementation of these integration and root-finding methods, it is necessary to have an alternate calculation that does not depend on the numerical methods. In the case of the quadruple integration carried out in Equation A.15, there is no simplification to an analytical solution except in the case of trivial choices of the Gaussian widths.

As a test of both the root-finding mechanism and the full quadruple-integral in Equation A.15, I calculate a series of z_α using $\sigma_i \rightarrow 0$. As the widths of the Gaussian distributions in Equation A.14 vanish, the distributions approach delta-functions, and Equation A.15 reproduces $z_\alpha = \frac{N_\alpha \cdot \epsilon_{B+}}{N_{B+} \cdot \epsilon_{B_c}}$ in the limit (N_α is the confidence level limit on the number of B_c events determined by Equation A.1). This is also precisely the limit in which the integration routines would be expected to break down. Numerical integration methods work best on smooth, well-behaved functions. As the widths approach zero, the value of z_α should approach the value of N_α times the various nominal efficiency factors until the functions become so sharply peaked that the numerical integration fails. In the implementation of the gaussian quadrature calculation, I have also effected a change of variable so that the numerical integrations are always over a Gaussian distribution with $\sigma = 1$. This ensures adequate sampling of the Gaussian lineshape where it contributes most to the integral. The tradeoff

is that the lower cutoff of the Gaussians must be integrated over with a larger degree of precision as the widths decrease from unity. For simplicity, I have chosen to use the measured values of σ_i and scale them all uniformly:

$$\sigma'_i = \sigma_i \delta, \delta \rightarrow 0.$$

Figure 49 shows the behavior of the numerical solution to Equation A.15 compared to the value of z calculated using the default N_α from Equation A.1. At $\delta = 0.75$, the difference between the generalized confidence limit and the PDG value (which assumes no uncertainty contributions) is already $< 1 \times 10^{-4}$. This is the same order as the accuracy limit specified to the numerical integration routine. No significant deviation from the limit is observed for any reasonable values of δ .

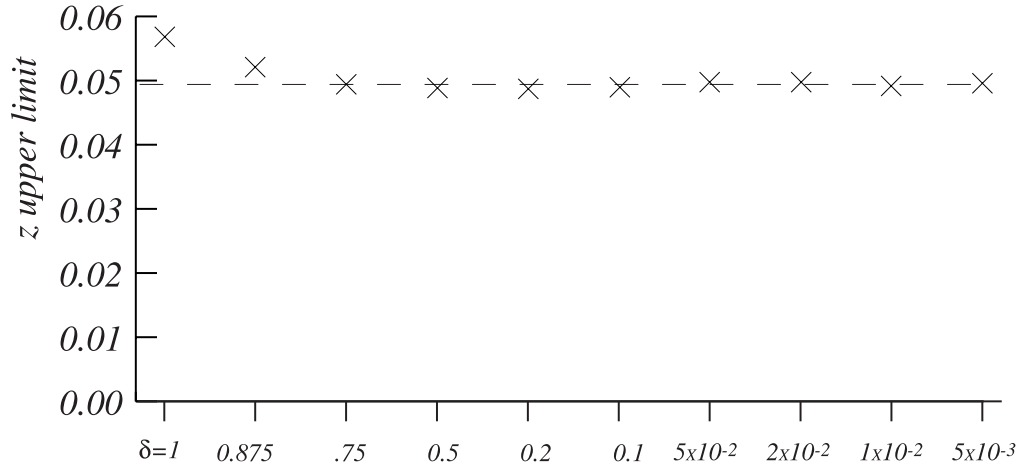


Figure 49: Generalized confidence level limit of Equation A.15 is compared with the simplified confidence level calculation with no uncertainties. These calculations are performed for the $J/\psi\pi^+$ mass bin of 6.2 GeV. The “X” points represent a calculation of the quadruple integral. In the limit $\delta \rightarrow 0$, the calculation converges to the ordinary single confidence level limit integral for a Poisson-distributed signal with finite background contribution. The value at $\delta = 1$ corresponds to the quoted upper limit for this mass bin.

References

- [1] S. Glashow, *Nucl. Phys.* **22**, 579 (1961).
- [2] S. Weinberg, *Phys. Rev. Lett.* **19**, 1264 (1967).
- [3] A. Salam, *Elementary Particle Theory*, 367 (1969).
- [4] M. Gell-Mann, W. Bardeen, H. Fritzsch, *Scale and Conformal Symmetry in Hadron Physics*, 139 (1973).
- [5] S. Weinberg, *Phys. Rev. Lett.* **31**, 494 (1973).
- [6] D. Gross, F. Wilczek, *Phys. Rev.* **D8**, 3633 (1973).
- [7] Particle Data Group, D. E. Groom *et al.*, *Eur. Phys. J.* **C15** (2000).
- [8] M. Kobayashi, T. Maskawa, *Prog. Theor. Phys.* **49**, 652 (1973);
N. Cabibbo, *Phys. Rev. Lett.* **10**, 531 (1963).
- [9] F. J. Gilman, K. Kleinknecht, and B. Renk, *Eur. Phys. J.* **C15**, 110 (2000).
- [10] M. Goldhaber, L. Grodzins, and A. Sunyar, *Phys. Rev.* **109**, 1015 (1958).
- [11] C. S. Wu *et al.*, *Phys. Rev.* **105**, 1413 (1957).
- [12] S. Bennett *et al.*, *Phys. Rev. Lett.* **19**, 993 (1967); D. Dorfman *et al.*, *Phys. Rev. Lett.* **19**, 987 (1967).
- [13] “The Discovery of the B_c Meson,” B. T. Huffman, J. Suzuki, P. Singh, S. Kim, E. Engels Jr., and P. Shepard, CDF document CDF/ANAL/BOTTOM/CDFR/3991 (1997); B. T. Huffman *et al.*, “The B_c Meson Lifetime,” CDF document CDF/ANAL/BOTTOM/CDFR/4118 (1997);

- F. Abe *et al.*, *Phys. Rev.* **D58**, 112004 (1998); F. Abe *et al.*, *Phys. Rev. Lett.* **81**, 2432 (1998).
- [14] F. Halzen, A. D. Martin, *Quarks and Leptons*, John Wiley & Sons, Inc., 203 (1984).
- [15] M. Masetti, F. Sartogo; *Preprint hep-ph/9503491* (1995).
- [16] M. Lusignoli, M. Masetti, S. Petrarca, *Phys. Lett.* **B266**, 142 (1991).
- [17] K. Cheung, *Phys. Rev. Lett.* **71**, 3413 (1993); K. Cheung, T. C. Yuan, *Phys. Rev.* **D53**, 1232 (1996).
- [18] C.-H. Chang, Y.-Q. Chen, *Phys. Rev.* **D46**, 3845 (1992); E. Braaten, K. Cheung, T. C. Yuan, *Phys. Rev.* **D48**, R5049 (1993).
- [19] M. J. Alguard *et al.*, *Phys. Rev. Lett.* **37**, 1261 (1976); *ibid.* **41**, 70 (1978).
- [20] G. Baum *et al.*, *Phys. Rev. Lett.* **51**, 1135 (1983).
- [21] K. Abe *et al.*, *Phys. Rev. Lett.* **74**, 346 (1995).
- [22] J. Ashman *et al.*, *Nucl. Phys.* **B328**, 1 (1989).
- [23] B. Adeva *et al.*, *Phys. Lett.* **B412**, 414 (1997).
- [24] K. Kolodziej, A. Leike, R. Rückl, *Phys. Lett.* **B355**, 337 (1995).
- [25] C.-H. Chang, Y.-Q. Chen, G.-P. Han, H.-T. Jiang, *Phys. Lett.* **B364**, 78 (1995); C.-H. Chang, Y.-Q. Chen, R. J. Oakes, *Phys. Rev.* **D54**, 4344 (1996).
- [26] A. V. Berezhnoi, A. K. Likhoded, M. V. Shevlyagin, *Phys. Atom. Nucl.* **58**, 672 (1995); A. V. Berezhnoi, A. K. Likhoded, O.P. Yushchenko,

- Phys. Atom. Nucl.* **59**, 709 (1996); A. V. Berezhnoi, V. V. Kiselev, A. K. Likhoded, *Z. Phys.* **A356**, 79 (1996).
- [27] C. Quigg, FERMILAB-Conf-93/265-T; W. Kwong and J. Rosner, *Phys. Rev.* **D44**, 212 (1991).
- [28] E. Eichten and C. Quigg, *Phys. Rev.* **D49**, 5845 (1994).
- [29] W. Buchmüller, S.-H. Tye, *Phys. Rev.* **D24**, 132 (1981).
- [30] K. Ackerstaff *et al.*, *Phys. Lett.* **B420**, 157 (1998).
- [31] M. Lusignoli and M. Masetti, *Z. Phys.* **C51**, 549 (1991); D. Du and Z. Wang, *Phys. Rev.* **D39**, 1342 (1989).
- [32] P. Colangelo *et al.*, *Z. Phys.* **C57**, 43 (1993); M. Beneke and G. Buchalla, *Phys. Rev.* **D53**, 4991 (1996); I. I. Bigi, *Phys. Lett.* **B371**, 105 (1996).
- [33] V. V. Kiselev, A. V. Tkabladze, *Phys. Rev.* **D48**, 5208 (1993).
- [34] V. V. Kiselev, *Preprint IHEP 95-80 [hep-ph/9507228]* (1995).
- [35] C.-H. Chang and Y.-Q. Chen, *Phys. Rev.* **D49**, 3399 (1994).
- [36] CDF Collaboration, F. Abe *et al.*, *Phys. Rev. Lett.* **81**, 2432 (1996); F. Abe *et al.*, FERMILAB-CONF-95-202-E (1995); F. Abe *et al.*, CDF document CDF/PUB/BOTTOM/PUBLIC/3268 (1995); B. T. Huffman, CDF document CDF/ANAL/BOTTOM/CDFR/3125 (1995).
- [37] DELPHI Collaboration, P. Abreu *et al.*, *Phys. Lett.* **B398**, 207 (1997).
- [38] G. W. Foster *et al.*, *Nucl. Inst. Meth.* **A269**, 93 (1988).
- [39] R. Blair *et al.*, CDF document CDF/MEMO/CDF/CDFR/1467 (1992).

- [40] P. Nason, S. Dawson, R. K. Ellis, *Nucl. Phys.* **B303**, 607 (1988); *Nucl. Phys.* **B327**, 49 (1988).
- [41] M. Mangano, P. Nason, G. Ridolfi, *Nucl. Phys.* **B373**, 295 (1992).
- [42] CDF Collaboration, F. Abe *et al.*, *Phys. Rev.* **D52**, 4784 (1995).
- [43] O. Helene, *Nucl. Instr. and Meth.* **212**, 319 (1983).
- [44] G. Zech, *Nucl. Instr. and Meth.* **A277**, 608 (1989).
- [45] A. D. Martin, W. J. Stirling, and R. G. Roberts, *Int. J. Mod. Phys.* **A10**, 2885 (1995).
- [46] C. Peterson, D. Schlatter, I. Schmidt, and P. M. Zerwas, *Phys. Rev.* **D27**, 105 (1983).
- [47] D. Bortoletto *et al.*, *Phys. Rev.* **D37**, 1719 (1988).
- [48] G. Alexander *et al.*, *Phys. Lett.* **B364**, 93 (1995).
- [49] J. Chrin, *Z. Phys.* **C36**, 163 (1987).
- [50] E. Braaten, K. Cheung, T. C. Yuan, *Phys. Rev.* **D48**, R5049 (1993).
- [51] K. Cheung, T. C. Yuan, NUHEP-TH-93-30.
- [52] N. Isgur, M. B. Wise, *Phys. Lett.* **B232**, 113 (1989), *ibid* **B237**, 527 (1990); M. B. Voloshin, M. Shifman, *Sov. J. Nucl. Phys.* **45**, 292 (1987), *ibid* **47**, 511 (1988); S. Nussinov, W. Wetzel, *Phys. Rev.* **D36**, 130 (1987).
- [53] H. Georgi, *Phys. Lett.* **B240**, 447 (1990).
- [54] A. F. Falk, M. Neubert, M. E. Luke, *Nucl. Phys.* **B388**, 363 (1992).

- [55] M. Neubert, *Phys. Reports* **245**, 259 (1994).
- [56] J. D. Lewis, P. Avery, CDF document
CDF/DOC/MONTECARLO/PUBLIC/2724 (1994).
- [57] M. Shapiro *et al.*, CDF document CDF/ANAL/MONTECARLO/PUBLIC/1810
(1992).
- [58] F. DeJongh, R. Hans, CDF document CDF/ANAL/TRIG/CDFR/1999 (1993).
- [59] P. P. Stephan, CDF document CDF/ANAL/TRIGGER/CDFR/3070 (1993).
- [60] J. Marriner, CDF document CDF/DOC/SEC_VTX/PUBLIC/1996 (1993).
- [61] A. Warburton, Ph.D. Thesis, University of Toronto (1998).
- [62] Particle Data Group, *Eur. J.* **C3** (1998).
- [63] B. Efron, *Am. Stat.* **40**, 11 (1986).
- [64] R. D. Cousins, *Am. J. Phys.* **63**, 398 (1995).
- [65] G. D'Agostini, "Bayesian reasoning in High Energy Physics - principles
and applications," CERN lecture notes,
http://www.cern.ch/Training/ACAD/reglec_E.html (1998).
- [66] G. J. Feldman and R. D. Cousins, *Phys. Rev.* **D57**, 3873 (1998).
- [67] C. Giunti, *Phys. Rev.* **D59**, 053001 (1999).
- [68] Particle Data Group, D. E. Groom *et al.*, *Phys. Rev.* **D54**, 166 (1996).
- [69] G. Zech, *Nucl. Inst. Meth.* **A277**, 608 (1989); O. Helene, *Nucl. Inst. Meth.*
212, 319 (1982).

- [70] C. F. Gauss, “Methodus nova integralium valores per approximationem inveniendi” *Werke*, Vol. 3, 163 (1816).
- [71] J. Stoer and R. Bulirsch, *Introduction to Numerical Analysis*, Springer-Verlag (1980).
- [72] W. H. Press, S. A. Teukolsky, W. T. Vetterling, and B. P. Flannery, *Numerical Recipes in C*, Cambridge University Press (1992).
- [73] I. Newton, *Methodus fluxionum et serierum infinitarum*, (1664-1671).
- [74] R. P. Brent, *Algorithms for Minimization without Derivatives*, Prentice-Hall (1973).



2017 ProQuest Distribution Agreement

This Agreement is between the author (Author) and ProQuest LLC, through its ProQuest Dissertation Distribution business (formerly ProQuest/UMI). Under this Agreement, Author grants ProQuest certain rights to preserve, archive and distribute the dissertation or thesis (the Work), abstract, and index terms provided by Author to ProQuest.

This page must accompany your manuscript and the rest of the submission materials

Please check type of manuscript:

Dissertation/Master's Thesis Submission Form

Please print clearly in block letters

☐ M (Master's Thesis)

☒ D (Dissertation)

Personal Information

Last Name Reher
First Name Douglas

Middle Name or Initial Corey
Country (ies) of Citizenship U.S.

Degree & Dissertation Information

Title of Dissertation/ Thesis A Search for Fully Hadronic Decay Modes of the B_c Meson at CDF

Institution conferring degree Univ. of California, Berkeley
College, School, or Division College of Letters and Science
Department or Program Physics
Degree awarded (abbreviate; e.g., Ph.D.) Ph.D.
Year degree awarded 2000
Year manuscript completed 2000

Advisor/Committee Chair Marjorie D. Shapiro

Committee Member Kam-Biu Luk

Committee Member Stephen D'Errenzo

Committee Member _____

Language of manuscript English

Primary Subject Category: Enter the 4-digit code and category name from the Subject Category Guide that most closely describes the area of your research.

Code 0798 Category Particle Physics

You may suggest two additional subject categories that may aid in the discovery of your work in our digital database.

Code _____ Category _____ Code _____ Category _____

Section I. License for Inclusion of the Work in ProQuest Publishing Program

Grant of Rights. Author hereby grants to ProQuest the **non-exclusive**, worldwide right to reproduce, distribute, display and transmit the Work (in whole or in part) in such tangible and electronic formats as may be in existence now or developed in the future. Author further grants to ProQuest the right to include the abstract, bibliography and other metadata in the ProQuest Dissertations & Theses database (PQDT) and in ProQuest Dissertation Abstracts International and any successor or related index and/or finding products or services.

ProQuest Publishing Program - Election and Elements. The rights granted above shall be exercised according to the publishing option selected by Author in Section III, Author Options, and subject to the following additional Publishing Program requirements:

- **Distribution of the Work.** Except as restricted by Author in the publishing option selected, the rights granted by Author automatically include (1) the right to allow sale and distribution of the Work, in whole or in part, by ProQuest and its sales agents and distributors and (2) the right to make the Abstract, bibliographic data and any meta data associated with the Work available to search engines and harvesters.
- **Restrictions.** ProQuest will use commercially reasonable efforts to restrict the distribution of the Work as provided under the publishing option selected by Author or *as later elected by Author* through direct contact with ProQuest. Such election is subject to Author's Degree Granting Institution Directives. With respect to restrictions requested after submission of the Work, Author acknowledges that ProQuest cannot recall or amend previously distributed versions of the Work.
- **Removal of Work from the Program.** ProQuest may elect not to distribute the Work if it believes that all necessary rights of third parties have not been secured. Refer to the website http://www.proquest.com/products_umi/dissertations/ for information about copyright and your dissertation or thesis. If Author's degree is rescinded, and/or the degree-granting institution so directs, ProQuest will expunge the Work from its publishing program in accordance with its then current publishing policies.
- **Degree Granting Institution Directives.** Author is solely responsible for any conflict between policies and directions of Author's degree-granting institution, Author's choice of publishing model, and/or any restriction Author places on the use of the Work. For the avoidance of doubt, ProQuest is not responsible for access to the Work that is provided by Author's degree-granting institution through its library or institutional repository. Author must work directly with Author's degree granting institution to ensure application of any restrictions to access relating to the Work by Author's degree granting institution.

Delivery of the Work. Author shall provide to ProQuest the Work and all necessary supporting documents during the online submission process, according to the Instructions accompanying this agreement.

Rights Verification. Author represents and warrants that Author is the copyright holder of the Work and has obtained all necessary rights to permit ProQuest to reproduce and distribute third party materials contained in any part of the Work, including all necessary licenses for any non-public, third party software necessary to access, display, and run or print the Work. Author is solely responsible and will indemnify ProQuest for any third party claims related to the Work as submitted for publication.

Open Access Publishing Plus

- ☒ I want the broadest possible dissemination of my work, and I want to provide free global access to the electronic copy of my work via the internet.
- ☒ I understand that I will not be eligible to receive royalties.

I want major search engines (e.g. Google, Yahoo) to discover my work. Learn more: <http://www.proquest.com/en-US/products/dissertations/google.shtml>

- ☒ Yes
☐ No

Acknowledgment: I have read, understand and agree to this ProQuest Publishing Agreement, including all rights and restrictions included within the publishing option chosen by me as indicated above.

REQUIRED Author's signature Douglas C. Reher Date 7/29/17

(Print Name) Douglas C. Reher

Institution conferring degree Univ. California, Berkeley

Provide up to 6 keywords or short phrases for citation indices, library cataloging, and database searching.

Current Contact Information

Current Email
Address

doug.r@comcast.net

Please provide your postal address if you are interested in receiving royalties on sales of your thesis.

City _____ Province _____ Daytime Phone _____

Country _____ Postal Code _____ Evening Phone _____

**Permanent Contact
Information**

Permanent
Email Address

doug.r@comcast.net

Street Address
(line 1)

2210 Rock St. #20

City Mountain View Province CA Future Phone (510) 967-8552

Country USA Postal Code 94043 Alternate
Future Phone _____

THIS PAGE MUST ACCOMPANY YOUR MANUSCRIPT AND THE REST OF YOUR SUBMISSION MATERIALS

Subject Categories

The ProQuest Dissertations & Theses (PQDT) database and the ProQuest citation indices are arranged by subject categories. Please select the one category below that best describes your field of research or creative work. You may add one or two additional categories on your submission form that will also be associated with your work as secondary subjects.

Arts, Business, Education, Humanities, and Social Sciences